White, Jordan (2025) *Improving efficiency and performance of rotary regenerative heaters: computational fluid dynamics-based optimisation of heat transfer plates.* PhD thesis.

https://theses.gla.ac.uk/85263/

Improving Efficiency and Performance of Rotary Regenerative Heaters: Computational Fluid Dynamics-Based Optimisation of Heat Transfer Plates

Jordan White MEng
XXXXXXXX

A thesis submitted to the College of Science and Engineering, University of Glasgow, to fulfil the requirements of the degree of Doctor of Philosophy in Aeronautical Engineering

Abstract

This study presents a comprehensive investigation into the enhancement of thermal and aerodynamic performance of heat storage plates within rotary regenerative heaters through computational fluid dynamics (CFD) simulations and optimisation techniques.

Rotary regenerative heaters are critical in industrial applications, especially in the power generation and process industries, where they recover waste heat from exhaust gases to enhance overall system efficiency. This process ensures that the industrial applications are as efficient as possible. There is a continual demand to improve thermal performance and efficiency to meet ever-tightening stringent energy efficiency and emission reduction goals.

This PhD project focuses on optimising the aerodynamic and thermodynamic performance of the heat storage plates, or elements, within a rotary regenerative heater using advanced CFD modelling techniques, geometric optimisation, sensitivity analysis and novel innovation of integrating delta winglet vortex generators.

The initial phase involved the development of a CFD model, which was validated against experimental data from a physical test rig. This model successfully predicted the heat transfer and pressure drop performance of 3 different element profile designs, ensuring that the model was robust and accurate, and could therefore be utilised as a “virtual test rig” for continued experimentation.

Subsequently, using the validated CFD model, a geometrical optimisation was performed on the flat notched crossed style element profile. Key geometric parameters – pitch between notches and radius of notches – were altered and tested following a Latin Hypercube design of experiments methodology, and the heat transfer and pressure drop performance was measured at each configuration. A Kriging surrogate model was generated from the input variables and results, and a multi-objective pattern search function found a predicted increase in heat transfer of 7.3% and a reduction in pressure drop of 2.3%. The predicted optimal configuration was tested using the CFD model and it was confirmed that the prediction was accurate to within 1%.

A sensitivity analysis was conducted to ensure the optimised element geometry was suitable for manufacture and to assess the effect of the manufacturing tolerances on the performance of the element. The analysis was conducted using a Box-Behnken design of experiments and kriging surrogate model. The results confirmed that the optimal design maintained an improvement over the baseline design, with the worst-case scenario showing higher performance over the original element geometry, affirming its suitability for manufacture and integration into real-world applications.

To further augment the element performance, vortex generators were studied. Delta winglet type vortex generators were added to the optimised element design. These aerodynamic devices improve performance by generating longitudinal vortex structures that disrupt thermal boundary layers and promote turbulent mixing, leading to enhanced convective heat transfer. The chosen delta winglet configuration involved winglets angled opposed to the notches, with the intention of directing flow towards this area to enhance the existing flow effects generated by the notches. An optimisation scheme was carried out on the winglets, focusing on the length, angle of attack and distance from front of plate variables. A further 1% improvement in both heat transfer and friction factor was established.

The findings highlight the efficacy of combining CFD simulations with optimisation techniques to optimise heat transfer plates, ultimately leading to reasonable enhancements in the efficiency and effectiveness of rotary regenerative heaters.

Contents

List of tables

Table of figures

List of symbols

Terms

$A_{Orifice}$ - Cross-sectional flow area of the orifice

A_{flow} - Flow area through the element test pack

A/B (can be changed) amplitude of upstream and downstream temperatures

C_d – Orifice discharge coefficient

c_s - Specific heat capacity of the solid material

D_h - Hydraulic diameter

H - Height

h - Heat transfer coefficient

J – Colburn factor

k - Thermal conductivity

L – Length

$\dot{m}$ – Mass flow rate

m_f – Hydraulic radius

m_s - Surface area to volume ratio of the solid geometry

Nu - Nusselt number

P - Pressure

Pr – Prandtl number

$\dot{q}$ – Heat flux

R – Universal gas constant

Re – Reynolds number

St - Stanton number

T - Temperature

u – Velocity

W - Width

Greek Symbols

β - Ratio of the orifice diameter to the duct diameter

ϵ – Expansibility factor

κ - Isentropic exponent

μ – Dynamic viscosity

ρ – Density

ϕ - Porosity

ω_o - Frequency of the temperature oscillation

Definitions & Abbreviations

ACHE: Air-cooled heat exchanger

CAD: Computer-aided design

CF: Colburn factor

CFD: Computational fluid dynamics

DACE: Design and analysis of computer experiments

DES: Detached Eddy Simulation

DNS: Direct numerical simulation

DU: Double Undulated

FF: Friction factor

FNoC: Flat notched crossed

GCI: Grid Convergence Index

HC: Herringbone Corrugated

LRAPH: Latent rotary air preheater

LES: Large eddy simulation

LMTD: Log mean temperature difference

PCM: Phase change material

PHE : Plate heat exchanger

RANS: Reynolds averaged Navier-Stokes

RAPH – Rotary air preheater

RRHE – Rotary regenerative heat exchanger

RSM: Response surface method

STHE: Shell and tube heat exchange

List of accompanying material

Previous work is constituted by a conference paper detailing the optimisation of the FNoC style plate. The work in that paper was undertaken as part of this project and thus there is some shared material, specifically referring to chapter 5 of this paper.

Multi-objective optimisation of heat transfer elements within a rotary regenerative heater.

Available at:

https://avestia.com/MHMT2023_Proceedings/files/paper/ENFHT/ENFHT_173.pdf

Preface

Some of the technical content of this PhD research project is protected under NDA. Howden Group have supplied technical data, drawings, designs and experimental results for use in this project. This data is confidential and will not be shared. To comply with this, the performance data, technical data, designs and dimensions will have normalised numerical values. No physical dimensions, measurements or records can be shown.

Additionally, colour scales for visualisations are normalised and constant, e.g. all heat transfer rate colour scales cover an identical range of values of heat transfer rate.

Thank you for your understanding.

Acknowledgement

Firstly, thank you to Howden for sponsoring this PhD project. Thank you to Dougal, Joanne, Adam, Laura and Kevan for your support and knowledge.

Thank you to both Craig and Marco for your insight, guidance and company over the years.

Results were obtained using the ARCHIE-WeSt High Performance Computer (www.archie-west.ac.uk) based at the University of Strathclyde.

Thank you to my family, Mum, Dad and Edith, for always being there for me, and helping me strive to be better. Your belief in me is the reason I am where I am now.

Thank you to my wonderful wife Saphira for giving me the strength and confidence to complete this project. I would not have been able to get here without your support throughout the years. Thank you for being by my side through it all and never wavering in your confidence in me.

Authors declaration

I, Jordan White, hereby declare that the work presented in this dissertation is my original work and has been carried out under the supervision of Marco Vezza & Craig White.

I confirm that this dissertation is the result of my own independent work and research, except where explicitly stated otherwise; all sources and references have been properly acknowledged and cited where appropriate; I have not previously submitted this work, or any part of it, for the award of any degree or qualification at any other university or institution; and this dissertation complies with the ethical standards of research as outlined by the University of Glasgow

Signed:
Print name: Jordan S. White
Date: 09/05/2025

1. Introduction

1.1 Background

In the current climate, it is becoming increasingly important to “go green”, especially within high emission industries, such as power generation and manufacturing. With rising social, economic and environmental pressure, increasing efficiency and reducing harmful emissions is imperative. Global commitments to reducing carbon footprints, driven by international agreements such as the Paris Accord, as well as stringent governmental regulations, have put immense pressure on industries to innovate and adopt more sustainable practices.

One key area where significant improvements can be made is in energy recovery and heat exchange processes. In power plants, manufacturing facilities, and other energy-intensive sectors, a large amount of energy is often wasted in the form of heat loss. Optimising heat recovery systems not only conserves energy but also reduces the reliance on fossil fuels, leading to lower emissions of greenhouse gases and other pollutants. As industries face these mounting challenges, technologies such as rotary regenerative heat exchangers offer promising solutions.

Rotary regenerative heat exchangers, specifically designed to recover waste heat and improve overall thermal efficiency, have long been used in large-scale industrial applications. Their ability to transfer heat between gas streams, minimising energy loss while maximising heat recovery, makes them critical components in reducing fuel consumption and emissions. However, as the demand for higher efficiency continues to grow, there is a need for further innovation in the design and optimisation of these heat exchangers to meet stricter environmental standards. By enhancing the heat transfer efficiency and addressing key issues such as leakage and pressure drop, rotary regenerative heat exchangers can contribute significantly to long term sustainable energy usage.

1. Introduction

The rotary regenerative heat exchanger (RRHE), also known as Ljungstrom heater, rotary regenerative heater, or, in certain circumstances, rotary air preheater (RAPH), consists of a large rotating wheel, or rotor, shown in Figure 1, filled with complex-profiled metal plates known as "elements". The RRHE is a type of regenerative heat exchanger, a heat exchanger that transfers heat indirectly using a heat storage medium. This medium is alternately exposed to hot and cold fluid streams, transferring heat via convection. The periodic fluid stream switching is achieved either by valves, where one fluid stream is closed off and the other is opened, or rotation, where both fluid streams are constantly open and either the fluid ducting or the heat storage medium are rotated to achieve periodicity (1).

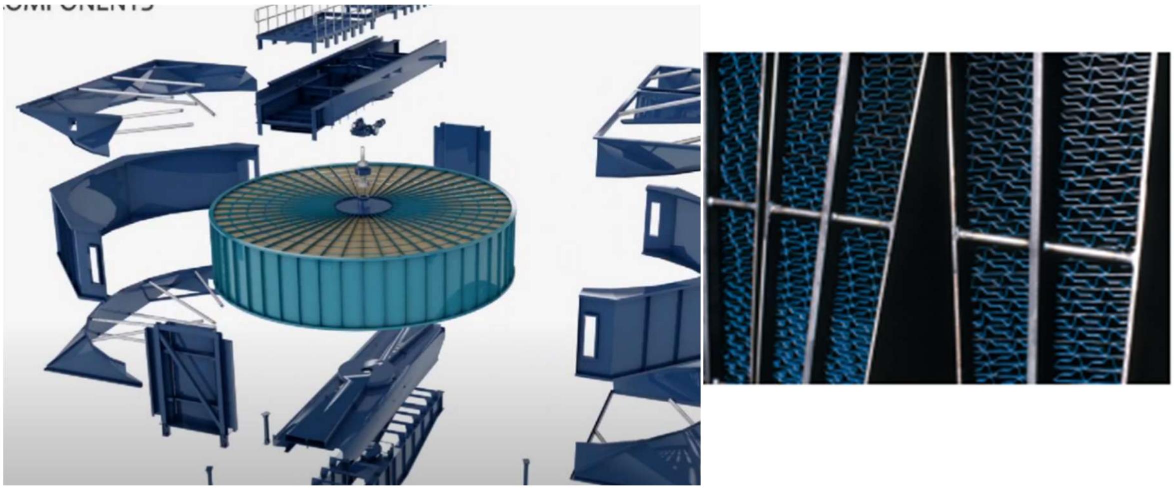

Figure 1. Exploded view of Howden rotary air preheater (left). Elements stacked within baskets (right)(3).

Throughout its history, the RRHE has been utilised in a wide variety of applications, including steam trains, steamboats, mill drying, brick manufacture, chocolate factories and more. (2)

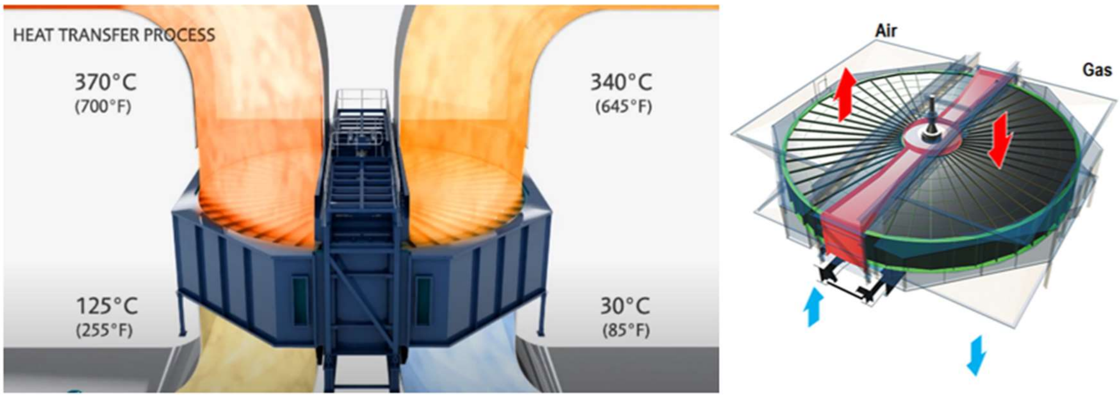

Figure 2. Air and gas flows through the Howden rotary air preheater (3)

The most common application of the RRHE is in the power generation industry, where it is used to preheat air. This form of the machine is known as a rotary air preheater, or RAPH. The RAPH effectively transfers hot exhaust gas from a power generation process, such as a coal boiler, to the cool inlet air, as shown in Figure 2. This reduces the energy requirement to heat the inlet air to the appropriate reaction temperature within the boiler, resulting in a significant improvement in efficiency. In coal boilers, this is quantified as a 20% reduction in coal usage (3).

Fortunately, the rotary heater is a versatile product and is commonly used in a variety of industrial processes, and sometimes is used multiple times within a single process for different applications. Once again using the coal boiler example, it is typical to feature an RRHE in conjunction with other emissions control devices in the treatment of flue gasses, as shown in Figure 3.

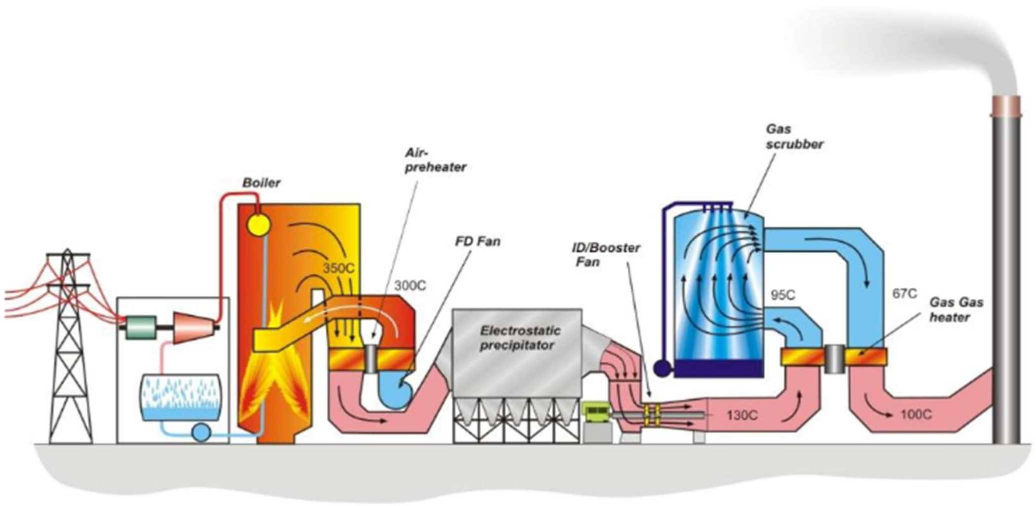

Figure 3. Diagram of power plant with RAPH for boiler and gas-gas rotary heater for removal of harmful gasses (3)

One example is with selective catalytic reduction machines (SCRs), also known as gas scrubbers, used for reducing nitrogen oxide emissions. These devices require inlet gas temperatures under 100°C for the emission capture reaction, but temperature of cooling tower must be higher to ensure that the gas will rise properly. To remedy this issue, an RRHE is required to extract heat from the inlet flow, cooling it from 130°C to 95°C, transferring it to the exhaust flow, which is heated from 67°C to 100°C. This process allows the gas scrubber to work efficiently, without wasting the heat required to raise the temperature of the exhaust flue gas to evaporate properly and rise through the cooling tower (3) (4).

Another study has shown that there is further use for a rotary heater in the removal of harmful sulphur oxides from the exhaust flow. The study found that using a gas-gas rotary heater, high humidity exhaust gas could be cooled, allowing the water within the gas mixture to condense on the heater elements. This dehydrates the gas, allowing the flue gas desulphurisation process to work more efficiently, reducing the harmful impact on the environment. Additionally, the removal of water impeded the dispersion and visibility of the exhaust gas, some of the main contributors to smog, as flue gas humidity plays a large factor in the smog process (5).

Rotary regenerative heaters play a crucial role in enhancing efficiency and conserving energy in industrial processes, contributing significantly to environmental sustainability, regulatory compliance, and cost savings. Given the importance of these factors, continued advancements in their performance are highly desirable. One key area for potential improvement lies in the optimisation of the heat storage matrix, where further innovations could deliver even greater efficiency gains.

The overall efficiency of a heat exchanger depends on two key factors: heat transfer and pressure loss. These factors categorise the heat exchanger's ability to transfer heat between mediums, and the associated operational costs required to do so. These factors both depend heavily on the geometry of the element plates within the heat storage matrix.

1.2 Thesis background

Howden currently manufacture market-leading rotary air preheaters, and are actively researching ways to improve their products, both for cost efficiency and environmental protection. One of the ways this research is conducted is through the "Element Development" program. This program involves designing and evaluating the corrugated plate heating elements within the rotary air preheater. The geometry of these plates greatly influences the heat transfer performance of the preheater; therefore, it is of high interest to study various geometries in detail to fully understand the mechanisms which affect performance.

The experimental testing is undertaken on a wind tunnel style test rig which measures the heat transfer and pressure drop characteristics of each element design. Manufacturing and testing each element design can be an expensive and time-consuming process: new rollers must be fabricated, then the elements are produced from mild steel sheets by the rollers before being shipped to the test rig location to be tested. This process can take up to 6 months, and if the factory is occupied with other projects, the research and development production loses priority.

In addition, the current research philosophy is very much a trial-and-error basis, with no method to analyse flow patterns. In this regard, the element chamber within the test-rig is a "black box". These factors combine to create an expensive, lengthy and inefficient research and testing process.

The current study is part of the Element Development program to integrate computational fluid dynamics into the design process. This aims to alleviate design costs and gain a deeper understanding of the flow through element packs to aid future design processes.

1.3 Background physics

The general theoretical background in heat exchanger design will be discussed in this section, defining the concepts and mechanisms heat transfer and pressure drop depend on. A deeper dive into the theory is presented in chapters 2 and 3 of this paper.

1.3.1 Performance factors

The performance of a heat exchanger is often measured through heat transfer and pressure drop.

Heat transfer is a measure of the amount of energy transferred from one medium to another within a heat exchanger. This energy exchange can be through radiation, conduction or most typically, convection. A high heat transfer rate ensures that a heat exchanger can bring the working medium to the required temperature effectively and efficiently, i.e. within a desired length of time or distance. The heat transfer rate often drives the size of a heat exchanger specified for a specific industrial heat transfer process: a higher heat transfer rate would require a smaller overall heater to achieve the same output. A smaller heater is desirable for cost savings, space savings and simplification of handling, transporting and installing.

Pressure drop refers to the reduction in pressure of a working fluid from the inlet to the outlet of a heat exchanger. Pressure can be lost through resistance experienced by the fluid through interaction with channels, tubes, or surfaces within the heat exchanger. This resistance leads to a loss in pressure, which is categorised as the pressure drop. To efficiently move fluid through a heat exchanger, a fan or pump is usually required. Higher levels of pressure drop result in an increased power requirement to maintain the desired flow rate, resulting in increased operational costs, or unsatisfactory flow rates, leading to a reduction in heat transfer.

It is therefore imperative in heat exchanger design to maximise heat transfer whilst minimising pressure drop.

1.3.2 Heat Transfer Enhancement

Heat transfer enhancement is the process of designing heat exchangers with the purpose of increasing the overall heat transfer rate, thus improving the efficiency and performance. The main area of focus is convective heat transfer, as the majority of heat exchangers involve a mix of solid-fluid energy exchange processes (6).

Many studies have been undertaken to understand the nature of heat transfer and turbulent flow in an attempt to use this understanding to develop improved heat exchanger designs.

The heat transfer in a system is defined by Newton's Law of Cooling, (Equation 1.1).

$$Q = h \cdot A_{surface} \cdot \Delta T \tag{1.1}$$

Where: Q is the overall heat transfer rate (W), h is the heat transfer coefficient (W/m^2K), $A_{surface}$ is the contact area between the two mediums (m^2) and ΔT is the difference in temperature between the two mediums (K) (7).

Enhancing the heat transfer rate, Q, requires an increase in h, A or ΔT. This section will discuss the general methodology in enhancing heat transfer.

1.3.2.1 Surface Area

Surface area plays a significant role in heat transfer. From Newton's Law of Cooling, (Equation 1.1), the heat transfer, Q, is proportional to the contact area A.

A larger effective surface area provides a larger contact region between the solid and fluid, resulting in an increased interaction, and therefore a larger energy transfer. The effect is a larger overall temperature change with the same heat transfer rate (7).

Another way to define this technique is through the effective heat transfer surface to overall volume ratio, also known as the specific heating surface area. An increased specific heating surface generally correlates to an increase in overall heat transfer rate.

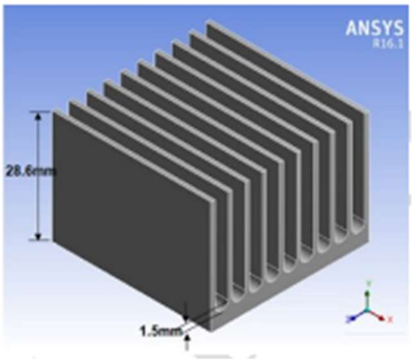

Figure 4. A general heat sink design. (8)

A common application of this technique can be seen in heat sinks used in computers and electronics. The basic heat sink has multiple tall straight fins protruding from the base, resulting in a significantly increased effective surface area compared to the base, as shown in Figure 4. (8)

Another application of this technique is present in plate fin heat exchangers. These heat exchangers use sheet metal profiled into tight corrugations between two flat plates forming narrow passages.

The drawback of this technique is the rise in pressure drop. By increasing the specific heating surface area, the available flow area is reduced, resulting in an increase in fluid resistance. (9)

1.3.3 Flow control

Using devices or geometry to direct and control the flow through the heat exchanger is a common method of enhancing the overall heat transfer and maximising efficiency. This can be achieved by directing flow to under-performing areas, or areas with a concentrated area of heat transfer surface, that may transfer heat more effectively – such as a corrugation, fin or other feature, in turn raising the overall heat transfer coefficient of the plate. Additionally, flow control techniques are used for promoting turbulent flows and vortex structures, further enhancing the surface heat transfer coefficient (6).

1.3.3.1 Turbulent mixing

Turbulence occurs when fluid flow becomes chaotic and irregular. These turbulent movements facilitate thorough mixing of the fluid, promoting uniform distribution of temperature and other properties. This is known as turbulent mixing and is a desirable flow characteristic in heat exchangers.

Turbulent flows disrupt the thermal boundary layers where rapid temperature changes occur near the surface. This turbulence enhances the mixing of the fluid, thereby reducing the thickness of these boundary layers and facilitating more efficient heat transfer from the surface to the bulk fluid. Ultimately, this process leads to a more uniform distribution of temperature within the fluid, minimising localised hot and cold spots and enhancing the overall heat management capabilities (10).

As such, it is often preferable to have a turbulent boundary layer over heat transfer surfaces within a heat exchanger. Turbulent mixing is often augmented through geometry design or by adding vortex generating devices.

1.3.3.2 Vortex generation

Vortex generation is a technique used to generate vortex structures or promote an earlier transition to turbulence. Early transitions to turbulence are desirable, as a larger portion of the boundary layer on the heat transfer surface is turbulent, and turbulent mixing is active at an earlier location, driving an increase in heat transfer (10).

Vortex structures can also be useful to direct flow, for example, in fin and tube heat exchangers, winglet vortex generators can be added to create vortex structures which direct flow toward the tube, enhancing the heat transfer in this key area. (11)

1.4 Project objectives

The primary objective of this project is to enhance the performance of RRHEs by improving the heat transfer characteristics of the heat storage plates. This has been achieved through several stages. Firstly, the aerodynamic and thermal behaviour of the profiled element plates within RRHEs were studied in order to gain an understanding of the complex flow structures and how they affect the heat transfer and pressure drop performance criteria.

This outcome was achieved through simulating the flow over element profiles in CFD and using modern flow analysis techniques to gain insight into the behaviour. Further understanding was found via an optimisation scheme. The Flat Notched Crossed (FNoC) element profile was chosen for experimentation due to its long-standing use in the industry, its well-established performance characteristics, and its status as a non-proprietary design.. Using popular design of experiments and optimisation methods, an optimal version of the element profile was found, maximising heat transfer and minimising pressure drop.

Heat transfer enhancement methods were investigated to determine the suitability of the application to element profile design in the RRHE industry. Delta winglet style vortex generators were added to the optimised FNoC element design, increasing the performance again.

The secondary objective is to investigate the factors that influence the performance of these heat transfer plates. This was accomplished by analysing the flow behaviour at each stage throughout the process to deepen the understanding of the mechanisms that drive the heat transfer and pressure drop qualities. By comparing the optimal FNoC to the original, it was possible to identify the positive and negative effects of observed flow behaviours. Additional insight was found by observing the difference in flow patterns after adding delta winglets, resulting in a new found understanding of the flow regime within these complex geometry channels.

1.5 Thesis Outline

Chapter 2 presents a review of the literature surrounding rotary heat exchangers, to provide some understanding of the background of the project and to highlight the requirement for the work undertaken throughout this project.

Chapter 3 encompasses a methodology of the setup of the “virtual test rig” CFD simulation, including discussion of the experimental test rig and simulation theory.

Chapter 4 validates the CFD simulation with experimental data using friction factor and Colburn factor correlations for the pressure drop and heat transfer respectively. Flow behaviour is then analysed through the element plates using modern visualisation techniques to study the flow patterns and vortex structures.

Chapter 5 presents an optimisation study undertaken on the FNoC profile. This study used a Latin Hypercube Design of Experiments and Kriging surrogate model methodology to optimise the geometry of the FNoC design. The optimised design excelled in both friction factor and Colburn factor. The predicted optimal design was tested with the CFD simulation to ensure accuracy, and the flow was analysed to identify the key differences driving the performance improvement.

Chapter 6 presents a heat transfer enhancement investigation, in which delta winglet vortex generators were added to the optimised FNoC element profile. The delta winglets were optimised with the length, angle of attack and distance from front of plate dimensions set as variables. A further increase in heat transfer was found, and the flow was visualised to analyse this performance improvement.

Chapter 7 presents an overview of the significant outcomes from the project and recommends future work to further develop this area of research.

2. Literature Review

This section focuses on examining the state of the art for industrial scale heat exchangers. Beginning with a comparison of the types of heat exchangers available, followed by an in-depth look into rotary heat exchangers, progressing on to heat transfer enhancement techniques and finally discussing optimisation methods. This will attempt to explain the place for rotary heat exchangers within industry, emphasise the necessity of improving performance and highlight the gap in the literature relating to the heat transfer enhancement of element plates within rotary regenerative heaters.

2.1 Heat Transfer and Heat exchangers

Generally, in a heat exchanger, the hot fluid flows through one set of passages, while the cold fluid flows through another. The thermal energy from the hot fluid is transferred through the wall of the heat exchanger to the cold fluid. This process is driven by the temperature difference between the fluids, in line with the second law of thermodynamic (1).

Heat exchangers come in a variety of designs and styles, with a multitude of use cases, benefits and drawbacks. These devices are used for heating and cooling in a vast range of industries, scenarios, and configurations, including power generation, product manufacture, food processing and storage, climate control, electronics temperature control and many more (12).

Whilst heat exchangers are used in many different fields, this thesis will primarily focus on large heat exchangers used in industrial applications.

Heat exchanger performance is measured through two main characteristics: heat transfer rate and pressure drop, although there can be other performance indicators depending on the scenario. The heat transfer rate is a measure of the heat exchanger's ability to transfer energy, and the pressure drop is a measure of the flow resistance, or the fan or pumping power required to reach the optimum flow rate. Enhancing either of these characteristics offers significant benefits. For instance, improving heat transfer performance can allow for a more compact design, as the exchanger can achieve the required outlet temperature with less surface area. This saves costs on materials, transport and installation, as well as reducing on-site footprint, which can be as crucial as cost saving in some cases, as sites can be very limited in space. Reducing the pressure drop results in a lower fan or pump power requirement, reducing initial costs and overhead costs. The overall combination of these factors is often referred to as the heat transfer efficiency or heat exchanger efficiency. An improvement in heat transfer efficiency is loosely defined by an increase in heat transfer rate per unit pressure drop, and can be achieved through increasing heat transfer, reducing pressure drop or through some combination of the two (13).

2.1.1 Shell and tube heat exchangers

The shell and tube heat exchanger (STHE) design consists of a large outer vessel known as the shell, which contains a bundle of tubes. One fluid travels through the tubes, while another fluid circulates around them within the shell. This setup enables the exchange of heat between the two fluids without mixing the streams. This heat exchanger design is popular due to its easily customisable design.

The arrangement of the tubes within the shell varies greatly for different applications and requirements. Any basic configuration can be modified by altering the number of tubes, length of tubes, tube path etc. Some examples of this are: additional tubes, which increases the surface area, and thus the heat transfer rate, but also reduces the flow area of the shell, increasing pressure drop; longer tubes increase the heat transfer with additional surface area, but results in a larger footprint on site.

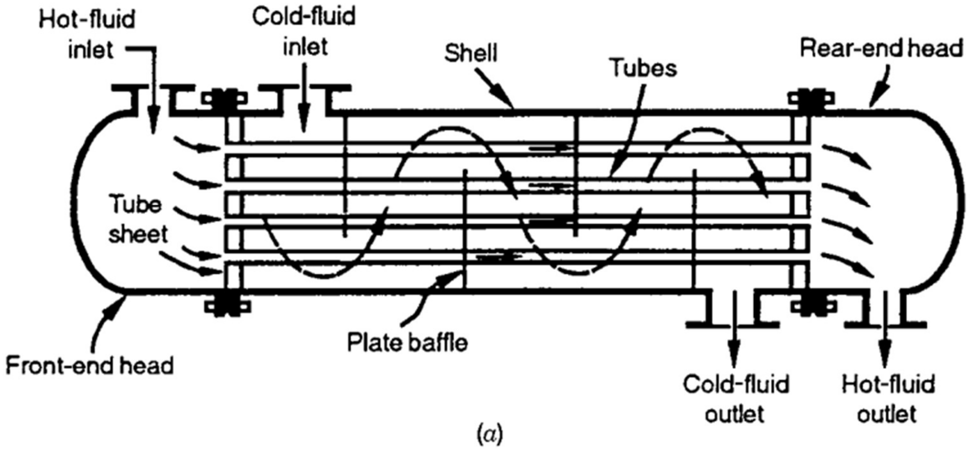

Figure 5. Shell & Tube heat exchanger layout diagram (15)

The path that the tubes take is also a key factor. The simplest tube path is a single-pass, where the tube fluid enters on one side of the heat exchanger and exists on the other. A double-pass tube path features a U-bend, where the tube fluid enters on one side, flows through to the other side, reverses direction through the U-bend and returns to the side it entered in, as shown in Figure 6. This extends the fluid residence time and increases the tube surface area, allowing an increase in heat transfer (14). This often results in a reduction in footprint compared to a standard STHE with the same heat transfer performance. There are drawbacks in the form of additional pressure drop incurred from the restricted flow area, and the U-bend restricts cleaning. This design is ideal for low space applications, or low fouling applications (15).

Additional fluid passes can be added to further increase the heat transferred, but there is limited performance improvement with each additional pass. Additional passes are often added to reach a desired tube fluid outlet temperature.

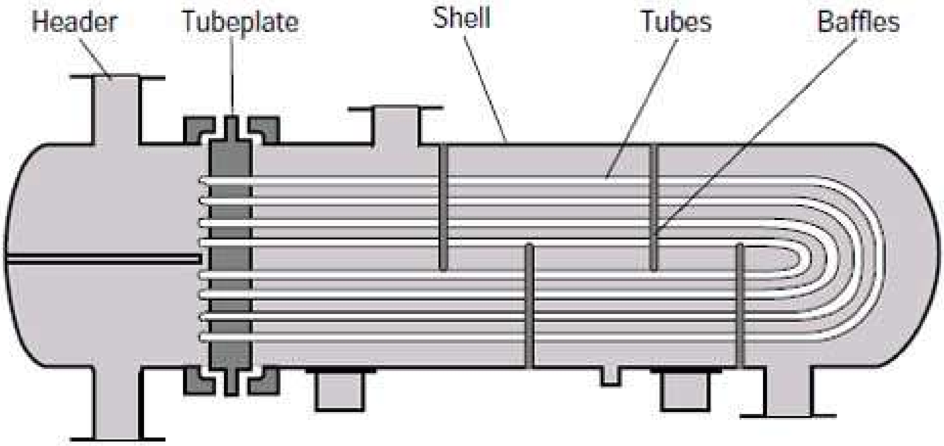

Figure 6. Double pass STHE with a U-bend feature (14)

The STHE is particularly effective for high pressure fluids due to the robust design and lack of leakage weak points, e.g. the gaskets on a plate heat exchanger. The design also favours large temperature differentials: the tubes and shell can be made from a plethora of materials to suit the required material restrictions, thermal stress levels and performance targets; and the tubes can be “floating” – not fixed at one end, to allow expansion and contraction with temperature changes. These factors make the STHE a top choice for chemical processing, petrochemical refining and power generation industries.

The drawbacks of the STHE include: larger footprints than other heat exchanger types, ground space is at a premium in most sites; high initial costs due to the complex design and materials required, especially for scenarios with high pressures or thermal stresses; and lower heat transfer efficiency for some applications, due to the relatively simple design and the difficulty in adding heat transfer enhancing devices, the performance can be limited and render the STHE unsuitable for high heat transfer requirements (15).

Some critical enhancements have been observed throughout the history of the STHE. Baffles were added to the shell to direct fluid flow to ensure consistent heat transfer across the surface of the tubes, eliminating dead zones. The baffles can also be set up to increase turbulent mixing and enhance the heat transfer further. This is demonstrated in Figure 5. Baffles increase the overall heat transfer rate, but also increase the pressure drop (15).

A study into baffle configurations found that “helical” baffles, baffles arranged in a spiral shape, resulted in increased uniformity of the velocity distribution, reducing dead zones, when compared to other common baffle types. However, a “flower” shaped baffle, circular baffles with alternating sections removed, resulted in the best overall heat transfer to pressure drop ratio (16). The results in this CFD study benefited from clear presentation of key performance metrics and well-defined flow visualisation techniques, allowing simple comparisons to be drawn from the data.

Studies have shown that altering the geometry of the tube walls can improve the performance. One study found that by implementing a corrugated tube wall, an increase in heat transfer could be gained with minimal effect to the pressure drop characteristic (17). Another study experimented with corrugated tube and shell walls, and found a maximum heat transfer efficiency increase of 24%, with convex corrugated tube walls and concave corrugated shell walls. This configuration was observed to minimise pressure losses from inefficient turbulent disruption whilst promoting heat transfer through effective turbulent mixing (18). Whilst the results were impressive, little analysis was presented to investigate the flow effects that drove the results.

Further enhancements were found via the implementation of twisted oval shaped tubes and found a significant decrease in pressure drop when compared to round tubes. The heat transfer rate also dropped, however the impact on heat transfer rate was far less than that on the pressure loss – resulting in an overall rise in efficiency (19).

Many studies have investigated twisted tape – a thin strip of material moulded into a helix shape. Inserting this device within a tube facilitates a reasonable increase in heat transfer, driven by a promotion of flow mixing, ensuring a more uniform temperature distribution across the tube.

One study tested plain, perforated and dimpled twisted tape inserts and found that the dimpled models generated the highest transfer, obtaining an overall performance improvement of up to 50% (20). A further study innovated by adding twisted tapes on the outside of the tube bundle. The tapes were inserted near the tube wall, and successfully induced flow mixing effects in this region. This manifested as a 20% increase in heat transfer rate across the heat exchanger (21).

2.1.2 Plate heat exchangers

Plate heat exchangers (PHEs) are devices comprised of stacks of thin plates arranged to form fluid channels between the plates. The fluid channels are set up such that heat to be transferred from the hot fluid to the plate wall, followed by the plate wall transferring heat to the cooler fluid. This set up is displayed in Figure 7. This facilitates effective heat transfer from one fluid to another without mixing the flows. The fluid streams are often arranged alternatively, such that a hot fluid channel is between two cool fluid channels, and vice versa (22).

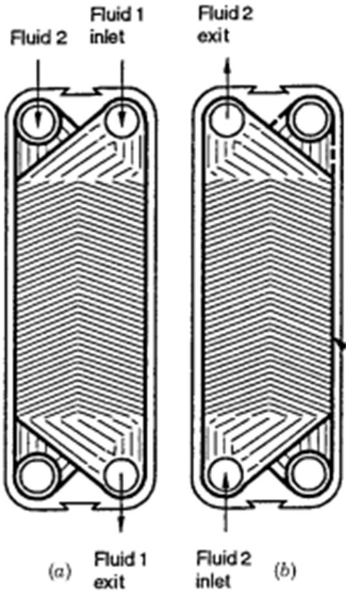

Figure 7. Typical PHE layout, split into two layers, a and b (6)

The plates within these heat exchangers are often formed with complex grooves and features (Figure 8) to enhance the heat transfer performance, and the study of this area has provided key insights into flow behaviour and heat transfer enhancement within heat exchangers as a whole.

PHEs are desirable for multiple reasons. Firstly, they are highly modular – the plates can be taken apart, swapped around for different scenarios, or the number of plates can be changed for different overall heat transfer requirements. This disassembly simplicity facilitates cleaning and maintenance as well. Secondly, high heat transfer performance is achieved through the complex geometry and multi-layered arrangement. The complex geometry also promotes turbulent flows and vortex structures, which results in reducing fouling and blockages. Furthermore, the alternating fluid layout allows very low temperature differentials across the two fluids, around 1°, compared to around 5° for other heat exchanger types. Finally, flow leakage is essentially non-existent due to the method of which the PHE is assembled (15).

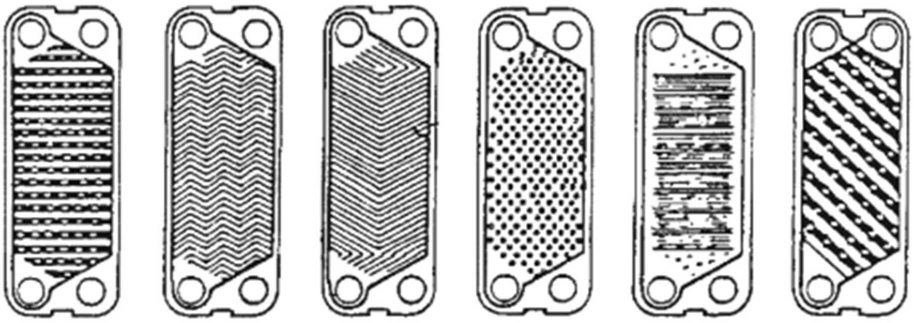

Figure 8. Various PHE layouts (22)

However, there are some drawbacks. Firstly, the PHE is not space efficient – the unit size can be much larger than other types of heat exchangers for the same amount of heat transfer. This is especially relevant in large plants or production facilities where floor space is at a premium, and thus minimising unit size is crucial. Furthermore, the standard PHE design has lower maximum pressure and temperature than other heat exchanger types. This is due to the modular design of the heat exchanger. Gaskets are required to ensure that each fluid stays in its intended channel, as mixing of the fluids not only reduces the effectiveness of the heat exchanger, but also compromises the composition of the process fluid, which can be dangerous for food industry applications. This can be solved with other types of sealing systems such as welding and brazing, however this adds to the cost of the heat exchanger. Additionally, the pressure drop through the PHE is much higher than other heat exchanger types (22) (6).

PHEs were first introduced in the dairy industry as part of the milk pasteurisation process (heating milk up to a defined temperature and holding it at the temperature for a set period of time to kill bacteria). Major applications include dairy, food & beverage industries, as the PHE facilitates a high level of hygiene, due to the ability to easily clean the machine; petrochemical and power plants, as water from a nearby source can be used to quickly cool down process fluids (22).

Some critical advancements in the field include the introduction of different sealing systems, such as brazing and welding plates. These methods bond the plates together along the sealing surfaces, eliminating the need for gaskets, thus increasing the maximum pressure and temperature limits up to 1MPa and 400°C. Additionally, welded PHEs offer a stronger bond than brazed PHEs, making them suitable for extreme environments and corrosive fluids, such as the power generation industry. The drawback of these design changes is that the heat exchanger can no longer be easily taken apart for cleaning and modification (23).

To combat this, the semi-welded PHE was introduced to create a best of both worlds. This design involves the plates being welded at one fluid side, and gasketed at the other. This allows one fluid to be high pressure, corrosive or otherwise unsuitable for use with gaskets, with the other fluid being suitable for gasket use. The use of gaskets again allows the PHE to be taken apart for cleaning, maintenance and alterations (22).

A critical example of heat transfer enhancement in this field is the development of optimal groove pattern configurations. One of the most common types is chevron style corrugations. These channels enhance the heat transfer by promoting turbulent flows, disrupting the boundary layer and increasing the effective surface area. At the same time, the corrugation pattern helps manage the pressure drop by providing clear channels for the flow, reducing resistance (22).

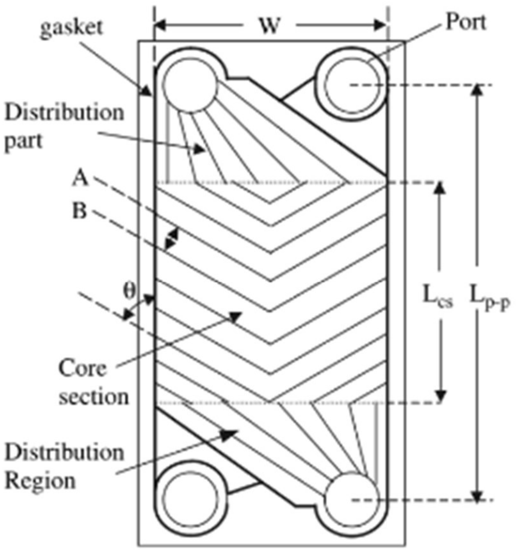

Figure 9. Chevron style PHE design (22)

While this style of corrugations is prevalent among plate heat exchangers, various studies have been undertaken to improve the design to optimise the heat transfer and flow characteristics. Lee et al. found that setting the angle of the chevrons to the flow direction as 66°, and the corrugation pitch to height ratio to 2.71, a 44% increase in heat transfer could be achieved, compared to the reference example with angle of 45° and pitch/height of 2.8 (24). This is a well-executed optimisation scheme, effectively covering the full range of geometry variables.

Another study investigated the pitch to height ratio, and found that as the corrugations increase in height, recirculation areas appear in the peaks and troughs, causing a reduction in efficiency, as shown in Figure 10 (25). This study visualised the flow data clearly and presents clear analysis exemplifying a full understanding of the flow behaviour.

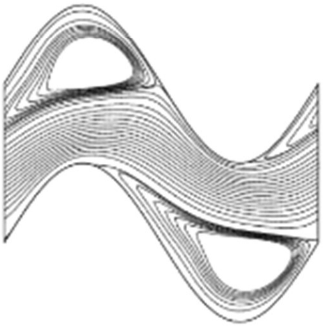

Pitch to height ratio = 0.75

Figure 10. Recirculation areas within larger pitch to height ratio corrugations (25)

2.1.3 Air cooled heat exchangers

Air-cooled heat exchangers (ACHE) are devices designed to dissipate heat from a medium using air. They typically consist of a fan blowing air over a heat sink, a structure that absorbs heat from the hot medium and transfers it to the air. To enhance heat transfer, the heat sink often includes fins that increase the surface area.

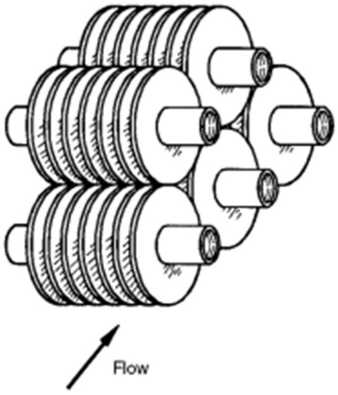

Figure 11. Finned tube heat exchanger diagram (12)

Finned tube heat exchangers are the most common large-scale ACHEs, and involve a tube carrying hot fluid, with fins attached to the outside of the tube to increase the effective heating surface area. Air is blown over the finned tubes by fans, removing heat from the process fluid. Multiple rows of tubes are often required to cool the process fluid to the desired temperature, which helps reduce the overall size of the heat exchanger. By using several rows, the front area of the unit is smaller, allowing for more efficient fan configurations. Due to the reliance on only ambient air for cooling, ACHEs are desirable for applications in locations with limited water supplies, such as dry, desert or inland areas. They are also widely used in power plants, chemical processing facilities, refineries and air-conditioning systems (12).

Finned tube heat exchangers generally experience higher pressure drops due to the resistance created by the tubes and the complex fin geometries. In contrast, PHEs and STHEs tend to have lower pressure drops and are often selected when water or another coolant fluid is available. Because finned tube heat exchangers rely on ambient air being blown over the tubes, they are prone to fouling from dust, debris, sand, or other particulates. Regular cleaning and maintenance are crucial to ensure their reliable operation. Additionally, air-cooled heat exchangers are often larger in size compared to other types because the heat transfer coefficient of air is lower than that of water or specialised coolant fluids, making air a less efficient medium for heat exchange (15).

Early studies in the area focused on tube arrangements, fin dimensions and tube materials to improve heat transfer and minimise fan power consumption. It was found that a staggered tube configuration provided superior heat transfer performance with an acceptable increase in pressure drop, as air streams are better mixed between tubes and there is increased contact between the air and the tubes compared to inline configurations (12).

Further enhancements in the area have been found through optimising the fin design. Kays & London designed louvered fins in the 1950s. This design involves cutting rectangular sections out of the fin and bending them upwards to break up the thermal boundary layer, promoting turbulence and enhancing heat transfer. (12) Further optimisation work was conducted using computational methods, finding that a louvre angle to the flow of around 36° and pitch between louvers of 1.8 mm resulted in a performance improvement of around 8% (26).

Microfinned tubes were introduced by Fujie et al in 1977. These are tubes with small fins or grooved patterns added to the inside, to increase heat transfer from the process fluid to the tube. The grooves are helical in nature, and facilitate an improved heat transfer rate through the increase of effective surface area, and through mixing of the flow. It was found that there is a significant temperature difference from the edge to the centre of the tube in plain tubes, which is reduced through the mixing effect of the helical microfins. (13) Further investigation was undertaken and found that heat transfer was enhanced by 80- 180%, with only a 20-80% increase in pressure drop, dependant on tube size, fin size and fluid properties (27). The experiments were conducted well, but the data is presented in a way that is difficult to understand. Better presentation could ease understanding of the effect of each of the variables on the heat transfer rate.

Another study investigated the effect of fin spiral angle, this, finding that increasing the angle from 10° to 37° increased the heat transfer coefficient significantly (28).

A further microfin design style is the herringbone tube, categorised by its V-shaped grooves. This geometry has the interesting effect of pushing fluid away at some sections and bringing it together at others. This results in a low pressure drop and low heat transfer at the diverging area and a high pressure drop and heat transfer at the converging area. One study tested various configurations of helical and herringbone microfins, and found that the herringbone designs had higher overall heat transfer coefficients, with similar pressure drop performance compared to the helical fin style (29). The investigation went on to investigate helix angle, confirming that an increase in helix angle results in increased heat transfer performance, at the cost of pressure losses.

2.1.4 Heat Exchangers Summary

The range of large-scale heat exchangers for industrial applications has been discussed. The STHE is suitable for high pressure and temperature fluids, due to its robust design with minimal leakage. It is often chosen for its high degree of flexibility, with a plethora of modifications available to tailor it to specific applications. The PHE is suitable for lower pressure fluids, features essentially zero leakage and the modular design ensures it can be taken apart easily for modification and cleaning, making it the clear choice for food processing and other hygienic applications. ACHEs are appropriate for cooling process fluids when another cooling fluid such as water isn’t available, and are simpler than other types due to the lack of a secondary fluid line, resulting in a lower cost solution.

2.2 The Rotary Regenerative Heat Exchanger

RRHEs are the most compact large-scale heat exchanger and are widely used for industrial gas-gas heat transfer processes. The compactness is due to the ability to use double sided heating surfaces, like plates within the heat storage matrix, as the matrix is fully immersed in a single fluid stream, unlike PHEs and STHEs which require a hot side and cold side of each heat transfer surface. This results in a much larger effective heat transfer surface per cubic volume, driving a higher high heat transfer rate, when compared to other large heat exchanger types (2). This feature also results in lower weight and overall volume for the same heat transfer rate compared to other types of heater, resulting in a lower cost and easier installation (30).

The biggest drawback of RRHEs is leakage. As the fluid streams are not fixed to specific channels, there are boundaries at which fluid can leak from one stream to the other. While the leakage can be reduced through various methods, it is extremely challenging to eliminate it. Leakage is undesirable as it can allow a fluid stream to become contaminated, which reduces efficiency and could be dangerous.

Most leakage occurs at the rotor's end faces, near the inlet and outlet. The leakage area is fixed in height and spans the width of the rotor. Since the rotor is circular, the flow rate increases with the square of the radius. As a result, leakage rate, measured as a percentage of flow rate, decreases as the rotor size increases. This means that there is a minimum size in which the RRHE becomes uneconomical, which changes depending on the application, but is commonly around 3 metres in diameter (1).

2.2.1 RRHE Design and Specification

The specification of a rotary regenerative heat exchanger (RRHE) for a given application is governed by multiple interrelated factors, including required heat transfer performance, acceptable pressure drop, spatial limitations, and operating conditions. The key design parameters—rotor diameter, matrix depth, heat transfer element type, and rotational speed—are interdependent, and therefore the specification process involves a careful trade-off analysis to achieve an optimal configuration.

The process begins with determining the thermal duty, defined as the amount of heat to be transferred between the hot and cold gas streams. This value is derived from the target outlet temperatures, the inlet temperature differential, the mass flow rates, and the specific heat capacities of the respective gas streams (6).

Following this, attention shifts to balancing rotor dimensions and selecting the appropriate element type. Element selection is primarily based on heat transfer effectiveness and pressure drop characteristics, but secondary considerations such as fouling potential, cleanability, and suitability for protective coatings are also crucial. In applications where the gas flow contains particulates such as ash or dust, complex channel geometries within the element matrix may promote deposition and blockages. In such cases, simpler geometries, such as the double undulated type, are preferred, as they offer improved cleanability and reduced fouling. Cleanability refers to the ability of the matrix to be cleared of deposits using jet cleaning systems or soot blowers. Straight channel designs are more amenable to such cleaning methods than more complex geometries like the flat-notched crossed type (31).

Coating adherence ability is another important factor, especially in corrosive environments where ceramic or metallic coatings are applied to protect the matrix. Element types with sharp geometries are typically unsuitable for coatings, as stress concentrations around edges can cause cracking or peeling. Therefore, the selected element must balance performance and longevity: a high-performing element with poor fouling resistance may be rejected in favour of a moderately performing one with superior durability.

Once the thermal and material considerations are addressed, the physical sizing of the RRHE is specified. Rotor diameter is often determined based on spatial constraints and gas velocity requirements. For a given mass flow rate, the diameter is selected to maintain the gas velocity within the optimal operational range of the chosen element type. The element's performance, particularly its heat transfer and pressure drop characteristics, is sensitive to velocity, and maintaining this within design limits ensures efficiency and longevity.

However, increasing the diameter can lead to higher internal leakage, particularly across the gas sector divider. This leakage arises due to the necessary clearance between the rotating matrix and the static divider plate, allowing cross-contamination between the gas streams and thereby reducing thermal effectiveness. This leakage becomes more pronounced as the diameter increases, since the gap area scales with the rotor (32). A larger diameter also increases capital and operational costs. Larger rotors experience greater structural deformation, necessitating additional reinforcement, typically thicker plates, leading to increased material usage and weight. This, in turn, requires more powerful drive motors, more robust bearing systems, and introduces challenges related to transportation and installation of the RRHE.

After establishing the diameter, the matrix depth is selected to meet the required total heat transfer surface area. Greater depth increases both the pressure drop and the available surface area. In some scenarios, increasing depth while reducing diameter can help reduce overall costs, as long as the gas velocity remains within the acceptable range for the selected element type (33).

The rotational speed of the heater is also considered, as it affects the heat transfer effectiveness and potential leakage between compartments. The ideal rotation speed is dependent on the gas flow rates, inlet temperatures, desired outlet temperatures,

Typically, a lower rotational speed extends the residence time of the matrix within each gas stream, allowing more heat to be absorbed or released by the heat transfer elements during each cycle. This increased contact time can enhance the heat transfer rate between the fluid and the solid matrix. Conversely, a higher rotational speed results in more frequent exposure of the matrix to the hot and cold streams, effectively increasing the number of heat exchange cycles in a given timeframe, which can also raise the overall heat transfer rate. An optimal balance must therefore be found: rotation must be slow enough to allow sufficient thermal exchange during each pass, yet fast enough to maximise the cumulative rate of heat transfer (6).

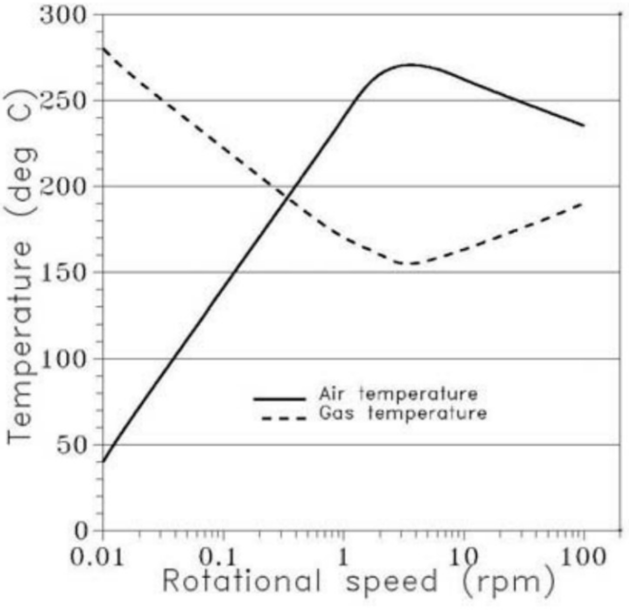

Figure 12. Outlet temperatures for varying rotational speed in a validated RRHE model (34)

One study investigating a computational model of a validated RRHE system operating within a coal-fired boiler process identified an optimal rotational speed of approximately 1.76 revolutions per minute (rpm) (34). The simulation results, corroborated by plant data, revealed a trend where heat transfer rate increases with rotational speed up to a range of roughly 1 to 3 rpm, as shown in Figure 12. Beyond this point, the reduced contact time within each fluid stream begins to limit the amount of heat transferred per cycle, resulting in a decline in overall effectiveness.

In summary, the RRHE specification process involves iterative optimisation of the element type, diameter, depth, and rotational speed, all guided by thermal requirements, mechanical constraints, gas properties, and cost considerations. Modern design methodologies often rely on computational modelling and selection software to manage these trade-offs and converge on an optimal configuration (35).

The performance of the heat transfer element type plays a central role in this balance. Elements with higher thermal efficiency reduce the required surface area, enabling more compact and cost-effective designs. Conversely, elements with lower pressure drop characteristics permit increased matrix depth without incurring excessive fan power penalties, improving operational efficiency. As such, the development and optimisation of novel heat transfer elements is a critical area of research, with significant potential to enhance overall heat exchanger effectiveness while simultaneously reducing system costs, an area explored in detail within this thesis.

2.2.2 RRHE leakage

One of the main ways to increase RRHE efficiency is through the reduction of leakage. Research shows that leakage has a significant effect on the performance of rotary heat exchangers. In Rotary Air Preheaters (RAPHs), leakage originates from a pressure differential between the hot gas and the cool air flows, typically from the airside to the gas side. The bulk of the leakage flows happen across the face of the rotor, where it is difficult to seal a rotating body against a stationary one. This leakage results in the energy expended by the fans to move the leakage air being wasted, resulting in an increase in operational costs and reduction in efficiency (36).

Several studies have been conducted to investigate the leakage in RRHEs. One study undertook physical and CFD experiments of an RRHE to analyse leakage, confirming that the pressure difference across the air and gas flows is the main driver of leakage flows. Additionally, it was found that reducing leakage results in an increase in boiler efficiency (37).

Various methods of reducing leakage have been utilised. The most prominent and simplistic method is the use of sealing fins attached to the radial seal. These fins prevent fluid from travelling between the hot and cold side. The sealing fins can be divided into two sub-categories: adjustable-rigid and flexible.

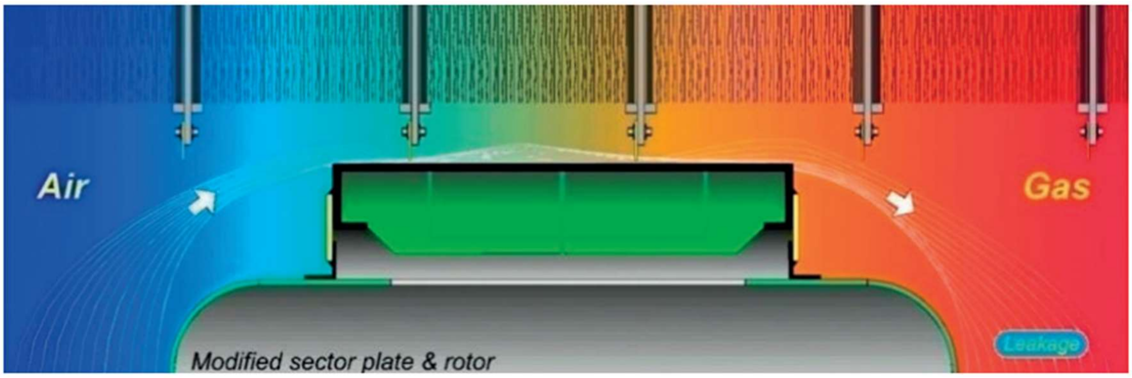

Figure 13. Leakage across face of rotor with rigid seals(3)

Rigid seals are strips of rigid material, such as steel, attached to the radial seal plate (Figure 13). These seals are usually adjustable to minimise leakage without impacting the rotor. However, as they are rigid, a small clearance gap must be implemented so contact between the fins and the elements is not made. Contact would result in friction losses: increased power would be required to rotate the RRHE at the same rate, and the seals would wear down over time. One study investigated the use of a series of rigid seals to reduce the leakage, finding that double seals reduce the leakage flow rate by 30% and triple seals by 43% compared to a single seal (38). This study presented experimental and CFD data and tested a wide range of scenarios to ensure complete analysis of the leakage flow. Another study found by reducing the clearance of the seals can improve the heat transfer rate by 4%, but didn't have the facilities to measure the actual leakage rate. (32)

In contrast to rigid seals, flexible seals are made of a non-rigid material and can be in contact with the element material. This contact allows for a better seal and overall reduced leakage. However, this comes with the drawback that these flexible seals are less durable due to issues such as friction and dust accumulation, and must be replaced often. To combat this issue, a "herringbone" flexible seal has been proposed (39). This consists of a combination of rigid sealing plates and a spring-like elastic herringbone flexible structure. This solves some of the problems that plague the other flexible seals, such as dust accumulation, however friction remains an issue. This sealing technology results in a leakage ratio of less than 6%. Whilst this is impressive, friction may cause the seal to wear down over time. Additionally, rigid knife-edge seals have been shown to maintain a 6% leakage ratio with slight adjustments over periods of several years, whilst being a far simpler method, with less maintenance and reliability issues (36).

2.2.2 Rotary Heater Element Material

Traditionally, elements were made from rolled mild steel. This material was chosen for its durability and heat transfer properties, as well as its relatively low cost (4).

The industry standard element configuration for a rotary air preheater in a boiler process usually involves mild steel elements at the hot end, with enamel coated mild steel elements at the cold end. Acid condenses on the surface of the elements at a certain temperature, named the “acid-dew point”. This can corrode the elements to the point of failure. The elements in the cold end are coated with an enamel coating to protect against this corrosion (36). This set up can vary depending on the application, with different applications resulting in various amounts of corrosive fluids and fouling.

Care must be taken in the production of enamel coated mild steel elements, as imperfections in the coating such as cracks and bubbles have been found to cause the coating to fail. Corrosive elements penetrated through the imperfections, gaining access beneath the coating, causing it to detach from the element plate (40).

A study into the application of a rotary preheater for the use of treating high humidity flue gas in a coal-fired power plant found that silicon carbide ceramic elements achieved a better condensation efficiency than steel, fluorine plastic and borosilicate glass. It was also found that the effect of the height and rotation speed of the preheater had no effect on the condensation efficiency after a certain height (5). The condensation efficiency is a measure of the percentage of sulphur oxides removed from the gas flow by cooling it to its “dew point”, the temperature at which the gas condensates on the heat transfer surfaces. While this paper presents a comprehensive analysis of case studies showing the improvements silicon carbide brings over the standard steel element plates, there is no mention of the initial cost of the element material or manufacture in comparison to steel.

Novel element materials have been studied, including “phase change materials” or PCMs, which derive from thermal storage materials used in solar panels (41). These applications generally involve capsules of the PCM which absorb and release thermal energy through melting and solidification. PCMs allow a smaller temperature difference in the element packs and larger energy storage density, allowing more energy to be transferred. The smaller temperature difference leads to less deformation and leakage (42).

2.3 Rotary Heater Element Geometry

There are several types of element profiles and configurations suited to a broad range of scenarios. Some element configurations excel in heat transfer and pressure drop characteristics, but are prone to blockage from fouling, and others excel in cleanability and are more averse to blockage, with the drawback of reduced heat transfer performance (43).

The heat transfer elements are integral to the overall performance of the RRHE. A higher heat transfer rate results in a higher temperature change across the gas flows. As the desired outlet temperatures of gas streams are usually a set value, this generally means that less heat transfer surface area is required, and by extension a smaller element matrix. This results in a cost saving, and reduction in heater size. A lower pressure drop is also beneficial: lower fluid resistance requires less fan power to achieve the desired mass flow rate. (12)

Unfortunately, due to the industrial applications and competition within the industry, most modern developments in element geometry are shrouded in secrecy. However, some research has been published about element geometry.

2.3.1 Flat Notched Crossed

The flat notched crossed profile, or FNoC, shown in Figure 14 consists of a series of notches at an angle to the flow direction, usually around 20-30° with flat areas in between. The pair of plates are identical, with the bottom plate flipped so the angle of the notches is opposing to the top plate. This creates a crossflow, with flow along the bottom plate directed one way, and flow along the top directed another, creating vortex structures. The cross flow, and vortex structures, result in well increased turbulent mixing, and drives exceptional heat transfer performance. Additionally, the large flat areas allow relatively free flow, resulting in a low pressure drop. The geometry is not easy to clean with a soot blower or high pressure water/steam, due to the crossflow, and it is therefore most useful in low fouling applications (44).

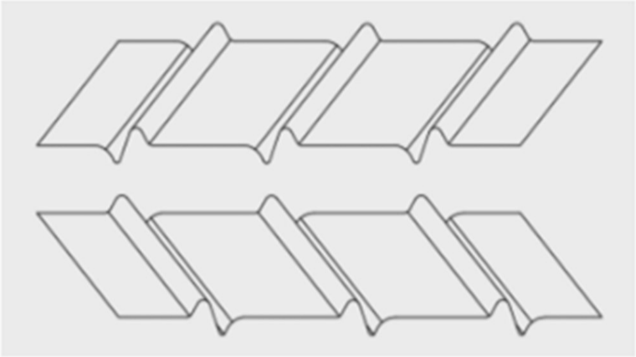

Figure 14. Flat notched crossed profile (43)

2.3.2 Double Undulated

The double undulated profile (DU), shown in Figure 15, consists of an undulated top plate, with sinusoidal type undulations, and corrugated style smaller undulations in between the larger ones, hence the name double undulated. The bottom plate is a simple corrugated plate. The undulations and corrugations are at an angle of around 30°, with the bottom plate angled in the opposite direction to the top plate.

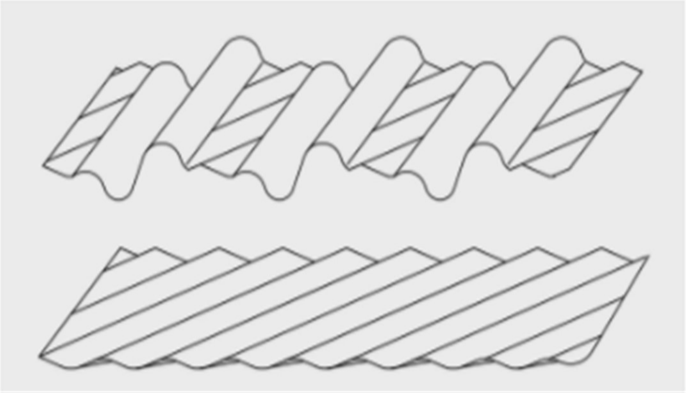

Figure 15. Double undulated profile (43)

This geometry has an interesting flow regime, where one section has the crossflow elements of the FNoC, and another section is a simple straight passage, allowing free flow.

The DU profile is essentially an "all-rounder", with good heat transfer and pressure drop characteristics, as well as good cleanability. It is used in a broad range of applications due to its versatile characteristics (44).

2.3.3 Herringbone corrugated

The herringbone corrugated (HC) design is a geometry profile developed by Howden, consisting of a herringbone style plate paired with a straight corrugated plate, shown in Figure 16. This profile maintains good thermal performance with minimal pressure drop, whilst adding other practical features. The Herringbone plate meets with the corrugated plate to create "closed" channels, where there is little crossflow. This allows the profile to be cleaned easily, and diminishes debris build up. There is also improvements in the structural characteristics, with the plates being much stiffer, resulting in less degradation from the pressure and vibrations in a RAPH (36).

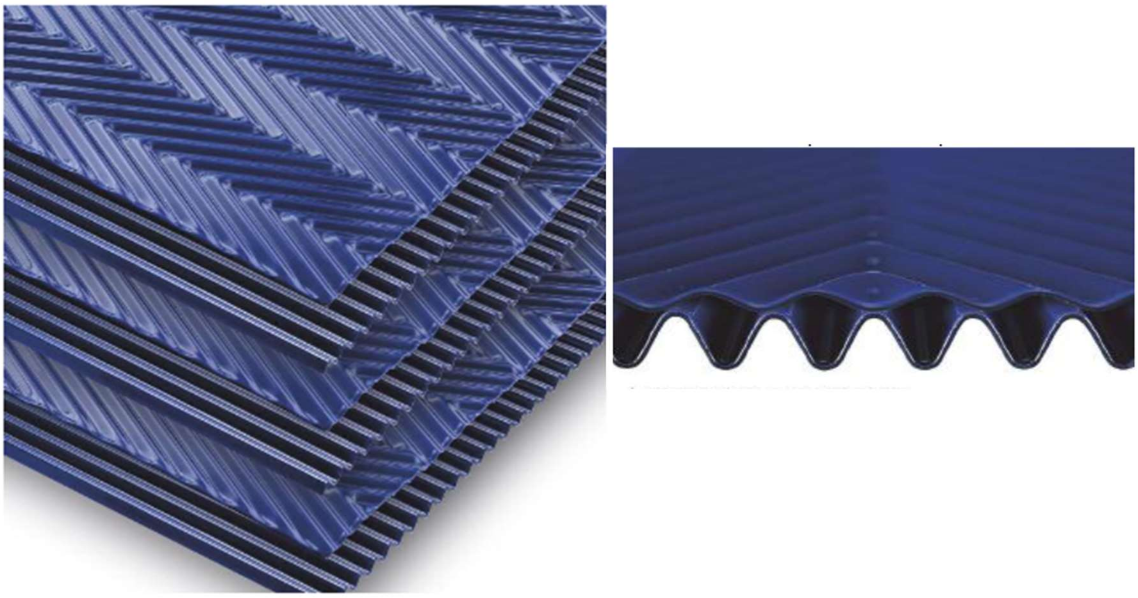

Figure 16. HC element plates (3)

2.3.4 Geometry factors affecting performance

There is very little published research on how specific geometry features affect performance, however one study about the effect of height and angle of undulations was published. In one study, variety of combinations of undulation height and angles were investigated. It was found that increasing the height of the undulations resulted in a reasonable increase in heat transfer, but a much larger increase in pressure drop. A very similar observation was made for the undulation angle. It is concluded that small increases in height and angle could give good heat transfer performance while retaining acceptable pressure drop characteristics (45). This gives the idea that a balance can be found between heat transfer and pressure drop performance, but further analysis is required to optimise these characteristics.

Another study optimised the heat transfer elements in a gas-gas rotary heater (46). The element pair consisted of a flat plate with a notch parallel to the flow and a corrugated plate with the corrugations at an angle to the flow. This angle, along with the peak-to-peak distance and depth of the corrugations were the variables optimised. A pressure drop improvement of 10% was found but came with the caveat of a 3% decrease in heat transfer coefficient. This study prioritised an improvement on pressure drop, which is a priority for gas-gas heaters, however in air preheaters heat transfer generally takes higher priority.

Other studies were performed with corrugated or shaped channels. “Sharp” corrugated channels, featuring pointed corrugation geometries, were found to be suitable for low Reynolds number applications. At higher Reynolds numbers, around 700 and above, recirculation zones develop within the trough areas, as flow separates as it travels over the sharp peaks. (47) The angle of corrugation was tested across at values of 20°, 40° and 60°, finding that Nusselt number rises significantly with angle, as do pressure losses. However, there appears to be a massive increase in both heat transfer and pressure drop between the 20° and 40° test points, indicating a vast change in flow behaviour between these configurations. It would be prudent to investigate intermediate corrugation angle to provide key insight into flow behaviour (48).

Sinusoidal crossed corrugated channels within a PHE were investigated. Research shows that flow separation occurs at higher Reynolds numbers within high amplitude corrugations with sharp corrugations, creating recirculation zones and reducing performance (49). This study provided valuable insight into the recirculating flow zones that exist within deep valleys. The numerical work was of high quality, but wasn’t validated against an experimental study, so it is unclear if the results are accurate and applicable to the real world. Additionally, further insight could be gained by varying the angle of attack the corrugations to observe how it alters the development of recirculation zones.

A study investigated the relationship between corrugation amplitude and wavelength in relation to the heat exchanger performance, finding that larger amplitude to wavelength ratio provides effective heat transfer, and confirming that recirculation zones form within the troughs of the corrugations at high Reynolds number flows (50). This study provided better insight into the detailed heat transfer over the surface of corrugated channels, finding that the heat transfer coefficient is maximised at the peak of the front face of the corrugation.

A divergent sinusoidal channel, as in a channel which expands from inlet to outlet , is shown to generate more chaotic mixing, driving an improvement in heat transfer when compared to a parallel sinusoidal channel (51).

Further research in shaped geometries can be found in the field of plate heat exchangers. Chevron, or herringbone, patterned plates are common in these heat exchangers. Studies show that chevrons tyle plates generate increased performance through the increase of effective surface area, boundary layer disruption and promotion of swirl flows (22). Another study found that angle of corrugations between 30 and 60° provide the optimum overall performance (52).

2.3.6 Rotary heaters summary

There has been a reasonable amount of research into rotary air preheaters as a whole, however the amount of available research into the element geometry is sparse, given that these elements are essential to the performance of the heat exchanger. It would be beneficial to further study factors such as plate thickness, types of notches and profiles, and radius, density, angle and height of corrugations and undulations to understand how the performance is affected. Further, there seems to be a general lack of research pursuing the understanding of the complex flow patterns present in these heater types.

2.4 Heat Transfer Augmentation Methods

As well as modifying the overall geometry, research has shown there are additional methods to further increase the heat transfer.

2.4.1 Surface Roughness

Artificially increasing the surface roughness of a heat transfer part is a common way to enhance the heat transfer rate. Cernecky et al. created a wavy style surface to induce roughness into a flat plate. It was found that the rough area disrupted the boundary layer growth and lead to enhanced heat transfer. (53) Forooghi et al. studied a number of roughness geometries, including pitting/dimpling, domes, and ribs to investigate the effects of roughness height, density and slope in a heat exchanger. It was found that steeper slopes tend to increase the pressure drop more than the heat transfer rate, lowering the effectiveness of the heat exchanger. Increasing the density and height was found to enhance the overall performance, although further increases in these factors created a “sheltering” phenomenon, where the trough/valley areas would trap pockets of flow, generating friction and reducing overall heat transfer (54).

Multiple studies have added round ribs of various designs to flat plates to augment heat transfer performance. According to the research conducted by Prasad et al., the presence of ribs in the laminar sublayer of the boundary layer has a minimal impact on the heat transfer and pressure drop characteristics of the flow. Moreover, the study suggests that the most effective rib size is approximately equal to the height of the boundary layer (55).

Taslim et al. studied ribs in a V-formation, and found that ribs at a 45° angle, pointing downstream achieved the best heat transfer to pressure drop ratio (56). Aharwal et al. studied the effect of a straight channel breaking up a continuous angled rib, allowing secondary flows to propagate through the area. A small increase in heat transfer was found, with significant improvements in pressure drop performance (57). Tanda studied a variety of triangular cross-section ribs and found a reasonable increase in performance. The performance was further enhanced with multiple ribs at an optimal spacing of 13 times the rib height (58).

2.4.2 Vortex Generating Devices

The use of vortex generating devices has become a common method to promote heat transfer through the creation of turbulent flow. These devices include various configurations, such as dimples, protrusions of different geometries, cut-outs, and other designs, with the intention of producing longitudinal vortex structures. These vortices improve heat transfer performance by enhancing turbulent mixing, inducing secondary flows, and disrupting the growth of boundary layers (59).

2.4.3 Winglets

Winglets are a form of vortex generator described as shaped and angled fins protruding from the surface of the heat exchanger plate. There is a great deal of research concerning the effects of shapes, size, angle and configurations of winglets on heat transfer and pressure drop. Winglets are differentiated from wings via the method of attachment to the plate.

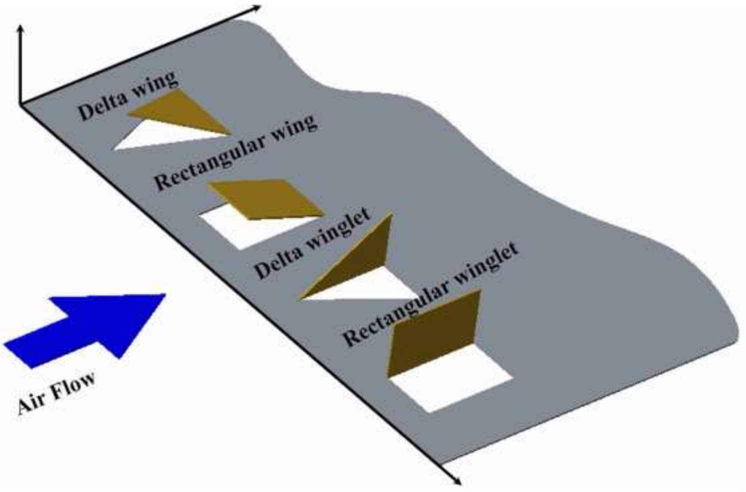

Figure 17. Rectangular and delta type vortex generators (69)

One of the simplest winglet types is the rectangular winglet. Rectangular winglets increase the heat transfer effectively through the generation of longitudinal vortices, which inspire turbulent mixing and boundary layer disruption throughout the region. One study found that angling the winglet to the flow increased the heat transfer performance, up to an angle of 35°, however the optimal configuration in regard to heat transfer and pressure drop was at an angle of 30° (60). Another study attached rectangular winglets to the inside of a tube and found a 27% heat transfer efficiency increase with 8 winglets. It was noted that the strength and number of longitudinal vortices was proportional to the number of winglets (61).

One of the most common forms of winglets are delta winglets. These usually comprise a right-angled triangle with the point and hypotenuse aligned with the inlet flow, although many studies have found success with directing the winglet at an angle of around 20-45° to the flow, keeping the face normal to the plate. The popularity of delta winglets can be attributed to the increased effectiveness when compared to the more basic rectangular winglet. Experimental studies from Fiebig et al. and Tiggelbeck et al. in the 1990s found that the delta winglets offered superior performance to the rectangular winglet, and the performance could be enhanced by angling the winglet to the flow (62) (63).

Lei et al. used a CFD model to test delta winglets with angles of attack from 10-50°, and aspect ratios of 1,2,3 and 4 in a plate and tube heat exchanger. The CFD model was validated against experimental data from an identical plate and tube heat exchanger without winglets. It was found that the 20° angle of attack and aspect ratio of 2 configuration yielded the highest heat transfer to pressure drop ratio, with a heat transfer increase of 35-45% and friction factor increase of 19-34% across the Reynolds number range (64). From observation of the data, it appeared that an optimal point could exist between aspect ratio of 1 and 2, as the difference in heat transfer enhancement is much smaller than the difference in pressure rise between the two configurations. Further experimentation could be done to improve heat transfer efficiency.

Li et al. tested height, spacing and angle of attack of delta winglet pairs upstream of a plate fin heat exchanger using experimental methods (65). It was found that 30° angle of attack performed best, but the tested values were 30°- 60°, showing that lower angles could perform better, such as the 20° case discussed previously. It was also shown that the heat transfer significantly reduces when the trailing edges of the delta winglet pair are too close together, with the 17.5 mm distance configuration producing lower heat transfer than the winglet-less configuration. This shows that the longitudinal vortices were counteracting each other, resulting in inefficient turbulence structures. This study generated a sound optimisation strategy and presented the data well, with the only further work requirement being an increase in the range of angles of attack tested.

He et al. experimented with configurations of multiple delta winglet pairs arranged in a V-shape, taking inspiration from the movements of groups of birds and fish. Over a range of Reynolds numbers, heat transfer performance was improved by around 32%, however pressure losses were increased by 20-40% across the Reynold number range (66). This was a unique experiment discussing constructive interference in terms of longitudinal vortex structures. Comparisons with regular delta winglet pairs showed that the V-shaped array resulted in a significantly lower pressure drop than a regular pair. Only two angles of attack and two levels of size were tested, with a large spread in results, showing that an optimal solution can be found with more testing.

Zhou et al. created curved trapezoidal shaped winglets and made comparisons with other winglet styles when added to a flat plate using experimental methods. The design intention of the curved style is to expand on the existing effect of winglet vortex generators, with the addition of a swirling effect . This configuration benefited from low pressure drop due to the curved, streamlined design, while enhancing heat transfer through the vortex structures developed by the trapezoidal form. It was found that for laminar and transitional flows, a pair of delta winglets provide optimal performance, whilst for turbulent flows, a curved trapezoidal winglet pair excelled with a high heat transfer rate and low pressure drop penalty

(67). This study presented a well-executed optimisation scheme and comparison between different winglet styles. While delta winglets have been well documented, the novel curved trapezoidal winglet has not, so it would have been beneficial to vary different variables such as curvature, length and height, and compare performance across different configurations.

Sarangi et al. designed “wavy” winglets, consisting of a rectangular cross-section winglet following a serpentine path along the plate. Using a CFD methodology, the wavy winglet was found to increase thermal mixing when compared to a regular rectangular winglet, resulting in a 20% improvement in heat transfer. A further improvement of 13% was found through increasing the angle of attack to 10° (68). This winglet style, when added to a fin-tube heat exchanger significantly reduced the wake area downstream of the tube. This paper benefitted from a comprehensive optimisation scheme, where all aspects of the winglet were varied, including length, angle of attack and period of waves on winglet, ensuring that the maximum performance was found. Further research on the “wavy” winglets found that whilst reasonable heat transfer enhancements were found, the pressure drop penalty was far greater, making the improvements less significant for realistic use cases. This CFD-based study focused on two configurations with fixed winglet dimensions; the results could be improved by varying the dimensions to find optimal proportions. (69)

Recent research has focused on modifying winglet-style vortex generators to enhance their performance. One modification involves punching a hole in the winglet. Gupta et al. investigated various configurations of rectangular winglets with punched holes using numerical methods, finding that the holes reduced fluid resistance, thereby improving friction factor performance. It was also observed that placing vortex generators further upstream increased heat transfer efficiency (70).

In another study, punching a hole in a rectangular winglet was found to aid in preventing fouling. Numerical and experimental methods were used to test the punched whole winglet, find that the hole generated a vortex structure that developed along the length of the plate, creating a sweeping effect over the surface. This sweeping action minimised stagnation zones where fouling typically occurs. Enlarging the hole size reduced pressure drop but impeded the formation of the vortex structure (71).

Ashish et al. examined rectangular winglets with varying numbers of holes using a CFD modelled validated with previous experimental work, and discovered that additional holes decreased flow resistance but also reduced heat transfer performance. Nevertheless, the impact on heat transfer was smaller than the reduction in pressure drop, leading to an overall improvement in heat transfer efficiency with 6 holes (72). While good results were found, the heat transfer increased with the number of holes, up to 6, the highest number of holes tested. A further increase in heat transfer with more holes may be available but was not found or tested within this study. It is also unclear whether heat transfer increases with number of holes only, or if it is a combination of other factors such as hole size, location or shape.

2.4.4 Dimples

Dimples are commonly used to disrupt the boundary layer for aerodynamic efficiency, but they are also used to enhance heat transfer through the same method.

An investigation involving plate heat exchangers demonstrated that adding dimples to a heat transfer channel increased the Nusselt number by 10%, indicating enhanced heat transfer performance. (73) In another study, the effect of dimple depth was evaluated. The findings showed that deeper dimples result in higher levels of heat transfer but also lead to increased flow resistance, due to the presence of recirculation zones within the dimple which appear at higher dimple depth values. The optimal heat transfer efficiency was achieved at a dimple depth of 0.2 times the diameter (74). In a further study, dimples were tested in a plate fin heat sink. It was found that the most sensitive factors affecting performance were the dimple depth and the pitch between dimples. The optimal configuration was determined to be a dimple depth of 0.5 times the diameter and a pitch of 2.5 times the diameter (75).

A comparison between convex and concave dimples claimed that convex dimples offer lower flow resistance while maintaining similar heat transfer performance. This is because concave dimples tend to entrap flow in recirculation zones within the dimple, whereas convex dimples cause flow separation in their wake. A pair of counter-rotating vortices from the sides of the dimple cause the flow to quickly re-attach, reducing the fluid resistance (76). This investigation presented thorough analysis on the differences between convex and concave dimples, finding that concave dimples contained recirculation zones within the dimple, whereas studies discussed previously found that these recirculation zones only appear at higher relative dimple depths. This study didn’t vary the depth, so the performance range wasn’t fully explored, and thus it cannot be fully concluded that convex dimples are superior to concave for heat transfer performance.

From the research, it appears that in general, dimples create a lower heat transfer performance than winglet type vortex generators, but also inhibit lower pressure losses. It is therefore recommended that dimples be used in situations where minimising pressure drop takes precedence over maximising heat transfer. Some studies have combined dimples with delta winglets to further increase performance. One study added a delta winglet pair upstream of a single large dimple, finding significant improvements of 42% to the heat transfer coefficient and very little increase in the friction factor, around 5% (77). This study used both experimental and numerical methods to validate the results and visualise the flow. It was found through visualisation that the longitudinal vortex induced by the delta winglet reduced the recirculation zone within the dimple, increasing efficiency. Four angles of attack of delta winglet were tested from 15-60°, with the optimum configuration lying between the 30° and 45°. However, research discussed previously showed delta winglet angles of attack of around 20° were optimum for heat transfer, showing that the higher angle of attack is necessary to reduce the recirculation zone within the dimple. Further work could be done in testing the relative size of the delta winglets and dimple and adjusting the placement of the delta winglets in regards to the dimple.

Another CFD-based study added a delta winglet pair upstream of multiple rows of smaller dimples and confirmed that the longitudinal vortices induced by delta winglets reduced the recirculation effect within the dimples, making them more effective. This study found a heat transfer enhancement of 36%, with a pressure loss increase of 36% (78). When compared to the other study, the heat transfer rise is of similar magnitude, but the pressure drop increase is much larger. This may be due to the smaller dimple size, or the winglet angle of attack of 18°, but it is unclear as the paper did not explore any additional configurations related to dimple size, winglet size, or winglet angle.

2.4.5 Heat transfer enhancement summary

In the pursuit of enhancing heat transfer efficiency in thermal systems, numerous passive techniques have been explored and implemented. Modifying surface roughness has been a fundamental approach, where roughened surfaces disrupt the laminar sublayer and promote turbulence, thereby increasing convective heat transfer rates. The addition of ribs to heat exchange surfaces introduces artificial roughness and secondary flow patterns, enhancing mixing and thermal performance. Winglet-type vortex generators have gained significant attention, with studies on rectangular winglets demonstrating their ability to produce strong longitudinal vortices that disrupt boundary layers. Delta winglets, characterised by their triangular shape, offer a balance between enhanced heat transfer and acceptable pressure drop penalties by generating stable vortical structures. Curved winglets further optimise this effect by inducing swirling flows that intensify heat transfer while minimising flow resistance. Adding perforations to winglets can reduce pressure drop and introduce new vortex structures. Dimples, as another surface modification technique, create localised zones of recirculation and flow reattachment, leading to improved thermal performance without substantial increases in pressure drop. Collectively, these methods—surface roughness alterations, ribs, various winglets, and dimples—provide effective strategies for passive heat transfer enhancement, contributing to more efficient and compact thermal system designs.

Overall, research shows that delta winglets are a promising area of research currently, with good performance in a wide variety of applications. The addition of delta winglets to heat transfer elements with an RRHE has not been explored but appears to be a plausible method to improve heat transfer performance. No further research is available on the application of heat transfer enhancement techniques of any kind to heat transfer plates with RRHEs. Thus, a gap in the literature is established.

Additionally, several studies have demonstrated the use of CFD to analyse delta winglets, helping to confirm that the method is reliable and appropriate for this type of application.

2.5 Optimisation

Optimisation can be defined as the process of finding the best solution to a problem. Optimisation of a product or process will usually involve finding the values of certain input variables that result in the maximum or minimum of a desired output value. In engineering scenarios, the input variables may be geometric dimensions (radius of curvature, length, twist angle etc) or flow properties (e.g. Reynolds number, pressure, velocity etc.) and the output may be some measure of performance (e.g. drag coefficient, friction factor, heat transfer coefficient).

2.5.1 Surrogate Modelling

Surrogate modelling is a technique used in complex optimisation problems. It involves creating a function to approximate the relationship between the inputs (variables) to the outputs (results). These functions are typically built from the ground up, using experimental data with different input variables (79).

Response surface methodology is a type of surrogate modelling introduced by Box & Wilson in 1951, (80). This method uses a second-degree polynomial function to model the real-world correlation. The results are typically represented on a 3D plot, with the variables on the X and Y axes, and the results on the Z axis, showing a surface which covers the range of the variables, as shown in Figure 18. The topology of this surface represents the effectiveness of the solution across the full scope of the experimental range, facilitating a quick, straightforward analysis of the problem (81).

This is a powerful method that has found widespread use through the scientific community. Zhong et al. (82) defined methods to use RSM for shell & tube heat exchangers with a novel approach to calculating heat transfer and pressure drop. Kim & Lee (83) used the response surface method to optimise a V-shaped rib in an internal cooling passage. Mohapatra, Sahoo and Padhi (84) optimised the heat transfer in a three fluid heat exchanger using RSM. Kola et al. (85) found the optimal solution to a twisted tape insert used to promote turbulent mixing within a double pipe heat exchanger using RSM.

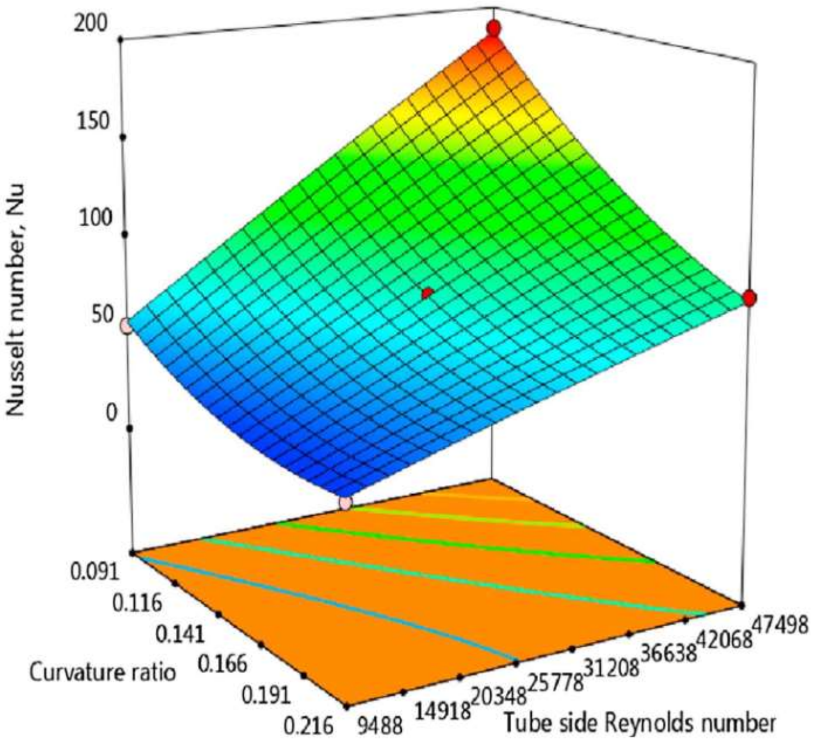

Figure 18. Response surface of Nusselt Number against spiral tube curvature ratio and tube side Reynolds number (84)

Kriging, also known as Design and Analysis of Computer Experiments (DACE), is a statistical method for predicting the behaviour of a function with unknown inputs, introduced by Santner, Williams and Notz in 1989, (86). It entails solving an optimisation problem to fit the model's parameters to each sample distribution. It is another form of surrogate modelling but differs from RSM as it does not rely solely on a polynomial model. For some complex problems, this model can not fully approximate the relationship between variables and results. Kriging uses a global polynomial model, with a covariance matrix handling local deviations. This allows for more complex response surface plots with the ability to show smaller peaks and valleys that RSM may not capture as shown in Figure 19. This increased accuracy and detail in local areas gives Kriging functions more versatility, allowing them to conform to more complex models, (87). Kriging has not seen the widespread use in engineering applications that RSM has due to its complex nature and inherent difficulty to use (88). Fortunately, there are now tools to assist with analysis, such as the DACE toolbox for MATLAB. Even so, it must be said that the polynomial nature of RSM is more straightforward and practical to use, making it the obvious choice if appropriate for the optimisation problem.

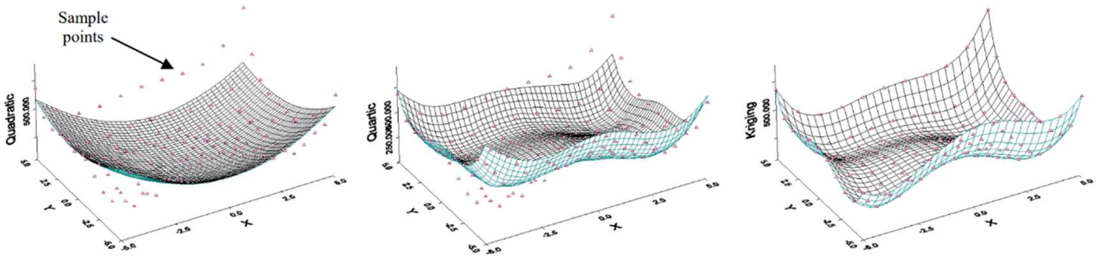

(a) 2nd Order RS Model (b) 4th Order RS Model (c) Kriging Model

Figure 19. Comparison of RSM and Kriging response surface plots for a complex example problem(88)

Mohammadi-Ahmar et al. (89) investigated the effectiveness of turbine blade film cooling with Kriging based methods. Kim and Shin (90) optimised a dimpled channel to increase heat transfer using Kriging and Latin Hypercube sampling. Augspurger et al. (91) used Kriging to optimise the fin design of a PCM heatsink.

2.5.2 Artificial Neural Networks (ANNs)

A study proposed the use of artificial neural networks (ANNs) to solve optimisation problems. ANNs are a type of machine learning algorithm, designed to mimic the structure of the human brain. The investigation sought to use an ANN for awkward problems where traditional optimisation techniques would struggle. The ANN achieved high accuracy when approximating objective functions, with the disadvantages of the necessity to “train” the ANN and some scenarios where the ANN has difficulty approximating more complex problems (92).

Several studies have used ANNs for optimisation problems relating to aerodynamics and heat transfer. One study optimised corrugated tubes using an ANN optimisation methodology. It was found that the predicted results deviated from the actual results by a maximum 0.63% (93). Another study used ANNs to optimise the geometry of a heat exchanger and found an increase in Nusselt number of 32%. However, there was an overall error of 2.6% comparing ANN predictions to experimental results (94). Investigations into baffles within microchannel heat exchangers used ANN optimisation techniques, finding a 46% increase in overall performance, with ANN prediction error under 1% (95).

One study developed a hybrid ANN approach, integrating traditional optimisation algorithms with ANNs, resulting in higher accuracy and lower likelihood of falling into local optimum (96).

2.5.3 Design of experiments (DoE)

Careful consideration must be taken when planning the experimentation process in an optimisation problem. It is important to design the experiments so that the full range of each variable is explored, and good analysis can be undertaken. This will allow solid, accurate conclusions to be drawn from the process.

The first step in designing the experiments is choosing the variables. Variables can be quantitative or qualitative. Quantitative variables are those which can be measured with a number, such as length, velocity or number of corrugations. Qualitative variables are more general, usually describing a type or feature of something, such as colour, material, or type of paint used (97). In some fields, variables are referred to as factors, qualitative variables are referred to as “categorical” and quantitative variables are referred to as “continuous”.

There are statistical methods to assist with the processing of planning the testing, known as Design of Experiments (DoE). These tend to help reduce the total number of experiments, while ensuring the full range of each variable is explored.

Box-Behnken design is a widely used DoE method which uses 3 values, or “levels”, for each variable, coded as -1, 0 and 1, or low, medium and high. The process can be designed such that 15 experiments will provide enough data to build the response surface for a problem with 3 variables. This is quite efficient, considering the maximum number of experiments would be 27 for this scenario. The drawback of Box-Behnken design is its restriction of 3 levels per variable. This constraint makes the technique more useful for qualitative factors, or quantitative factors with few possible values.

Another popular DOE method is Latin Hypercube sampling, first proposed by Mckay and Beckman in 1979, (98), and later refined by Iman in 1980 (99). This method is useful for quantitative variables. It is a semi-random technique which aims for a good distribution of values across the range of each of the factors. This ensures each variable is properly explored and defined, leading to a better understanding of the optimisation problem. This technique is particularly useful for variables with a wider range, such as the current study, where the distance between notches could be varied from 20 mm to 40 mm, for example (100).

The Box Behnken technique could only sample the notch distance as 20mm, 30mm and 40 mm, whereas Latin Hypercube could test a wide range of values between 20 and 40 mm. This would be beneficial if, hypothetically, the optimal distance was 33 mm. Box Behnken design would identify that the optimal solution lay somewhere between 30 mm and 40 mm, however unless the solution was linear and the value could be interpolated, the optimal value may never be accurately identified. On the other hand, Latin Hypercube may test several points around the optimal value and allow the optimisation algorithm to accurately approximate the model (101,102). In summary, Latin Hypercube is the ideal choice of DoE for problems with a wide range of possible solutions, whereas Box Behnken is more suited to problems with a finite set of solution points, i.e. low, medium and high, or yes-or-no type variables.

2.5.4 Tolerances & Sensitivity

In any manufacturing process, there must be some variation in dimensions or physical properties in products. These variations can be due to a number of reasons, such as movement in the machinery, atmospheric conditions, or variation in material qualities. These variations can be detrimental to the quality of a product in a variety of ways: two parts may not fit together as designed; a rotating part may have an irregular shape, disrupting the balance and inducing rotational vibrations; a load-bearing part may not be large enough to distribute the load effectively, resulting in a failure; or a complex aerodynamic device may not control the flow as intended. (103)

Whilst these variations may never be fully avoidable, it is possible to manage them. Managing variations requires tolerances, well-defined allowances for small variations in product dimensions and qualities within which the performance and standards of the product is acceptable. Defining the tolerances of a product is a process of defining the limits beyond which the product is no longer suitable for the intended purpose.

There is a cost associated with defining tolerances. Generally speaking, defining overly tight tolerances increases the manufacturing cost, as a higher percentage of products manufactured fall outside of the tolerances, and are therefore wasted. This results in a delicate balance between higher performance from tight tolerances, and lower cost from loose tolerances.

To find the optimum tolerance band, a sensitivity analysis is undertaken. This involves analysing the performance of the product over the tolerance range to identify the point at which the best compromise between cost and performance is achieved.

The methods of analysing the performance across the tolerance range are varied and have been improved and refined through recent history. These methods typically fall into four categories: worst-case, statistical, reliability-based and sampled.

Worst-case tolerance analysis compounds the maximum performance reduction at each tolerance bound, to provide an absolute worst-case scenario. While this is relatively simple to compute, it can result in a flawed view of the performance over the tolerance range, and result in a sub-optimal compromise between tolerances and cost. (103)

Statistical tolerance methods assume that manufacturing variations follow a statistical distribution and accept a certain level of non-conformance. This provides a more realistic representation of the cost-tolerance compromise; however, it is not tailored to each application, and thus there may be special circumstances which require specific tolerances that are overlooked (104).

Reliability based tolerance analysis measures the effect that variations in dimensions have on the overall system performance. A tolerance limit is then set at the minimum tolerance values that ensure the system’s robustness. This effectively calculates the maximum variation in each dimension that can be tolerated before the system loses reliability. This method can result in robust tolerance specification but is heavily reliant on the Hasofer-Lind Reliability Index, which can be computationally inefficient to run, and struggles with non-linear problems (105).

Sampled tolerance analysis uses test data at sampled data points to estimate the effect of variations through the tolerance range of each dimension. This can be thought of treating the problem as an optimisation problem, maximising performance and minimising cost.

Michael & Sidall first established the use of an optimisation scheme to maximise performance and minimise the manufacturing cost associated with tolerances and quality control in 1982 (106). The study took inspiration from statistical optimisation methods, creating an optimisation algorithm which accounts for the cost of waste, effectively creating the framework of the modern tolerance sensitivity analysis using optimisation methods.

Design of Experiments methods were incorporated into the sensitivity analysis process to reduce the time and cost expended during the process. Initially, the Monte Carlo system resulted in success, but a large sample size requirement made it cumbersome and inefficient to use (107). Other studies replaced the Monte Carlo system with more efficient DoE techniques, such as the orthogonal array, finding similar levels in accuracy with reduced computational power requirements (108). Shoukr et al. further increased the efficiency of the process by assigning weight factors to each dimension within the design of experiments algorithm, allowing specification of the significance or importance of each dimension (109). This enables more computational power to be allocated to the most influential variables, ensuring accuracy and efficiency.

A study involving a shell and tube heat exchanger used optimisation methods for a sensitivity analysis, finding that heat exchanger effectiveness has higher sensitivity at larger hot/cold fluid temperature differentials, showing that tolerances may change over the range of operating conditions (110). This study used the Response Surface methodology and Box-Behnken DoE optimisation methods effectively to accurately define tolerance limits.

Another study involving the optimisation of delta winglets in a solar air heater performed a sensitivity analysis using surrogate modelling optimisation techniques (111). This investigation used the Latin Hypercube DoE and kriging response surface method to analyse the heat transfer and pressure drop performance of optimised delta winglet vortex generators over the tolerance range. It was found that the height of the winglets was the least influential on performance, finding that winglet length and angle were far more significant in the performance.

These studies demonstrate that optimisation approaches, such as surrogate modelling, are effective tools for measuring the sensitivity to manufacturing tolerances. The use of these methods allows for a comprehensive evaluation of the design space and operating conditions, providing valuable insights into the behaviour of key variables and ensuring robust performance across varying conditions. Given the success of these techniques in previous research, their application in the current study is well-supported and appropriate for optimising heat transfer elements and evaluating the impact of the pre-established design tolerances.

2.6 Literature Review Summary

This literature review provides a comprehensive exploration of heat transfer enhancement techniques in heat exchangers, with a specific focus on rotary regenerative heat exchangers It begins by discussing general heat transfer principles and various heat exchanger types, including shell and tube, plate, and air-cooled heat exchangers, summarising their performance and design considerations.

The review then delves into rotary regenerative heat exchangers, outlining their importance in industry and comparing with other large scale heat exchanger types, common applications, and key areas of research such as leakage and the materials used for their heat transfer elements. A detailed examination of different rotary heater element geometries is presented, including flat notched crossed, double undulated, and herringbone corrugated configurations, highlighting the factors that influence their thermal performance.

Further studies involving heat transfer elements is discussed, outlining the lack of public research in this area. Whilst RRHEs are a somewhat niche topic due to their specific applications, there is a reasonable amount of published work in the area, focusing on leakage, corrosion, simulating the performance of the heater, and discovery of new applications for the technology, there is a fundamental gap in the literature surrounding the heat transfer elements. This is mostly due to the competitive market for RRHEs: enhanced element geometries can provide vast improvements in performance, and the sponsored research is usually kept secret to gain an advantage in the market. Therefore, there is very little available literature on the subject of heat transfer mechanisms within RRHE heat transfer elements.

The review then discusses heat transfer enhancement methods. Fortunately, there is a wide array of research available on this subject, including extended surfaces, surface roughness, ribs, dimples, and vortex generators such as winglets. While these studies focus on other heat exchanger types, such as PHEs and ACHEs, the techniques are analysed and compared to determine the suitability of applying to RRHE heat transfer elements, with a particular focus on the impact these modifications have on the flow behaviour and resulting heat transfer performance. Again, there is a gap in the literature involving applying heat transfer enhancement methods to RRHE heat transfer elements. This section concludes that delta winglet style vortex generators are useful for creating vortex structures that increase turbulent mixing, control flow and disrupt the boundary layer, resulting in a significant performance improvement.

Finally, optimisation techniques are reviewed and compared to establish the most suitable method for optimising heat transfer element plates. This section covers surrogate modelling techniques such as response surface modelling and Kriging, artificial neural networks, and Design of Experiments methods, including Latin Hypercube and Box Behnken. It was established that a Latin Hypercube Design of Experiments and Kriging surrogate model methodology would result in an accurate, efficient and effective optimisation regime. The discussion then moved to tolerances and sensitivity analysis, highlighting the necessity of tolerances and ensuring the reliability of performance across manufacturing tolerance ranges. Research show that optimisation schemes are a common method of testing the sensitivity range. Surrogate model techniques combined with Design of Experiments methods have been used to map the performance across the tolerance range, facilitating simple analysis of the robustness of the design when subject to manufacturing tolerances.

3. Methodology

This thesis will use the STAR-CCM+ Computational Fluid Dynamics (CFD) software to simulate the rotary regenerative heat exchanger element test rig at Howden, creating a "virtual test rig". The priorities of this investigation involve the creation of the virtual test rig, in which the characteristics of element profiles can be predicted, including heat transfer coefficient, pressure drop, friction factor and Colburn number. This aims to help reduce the cost and time of physically manufacturing elements and testing them. A second priority is to visualise the flow to understand how the different geometries affect the properties of the airflow, such as inducing turbulence or increasing effective heating area. This data will then be used to design new element profiles which are optimised for certain scenarios.

3.1 Experimental set up

The element test rig at Howden is shown in Figure 20. It comprises an air blower system that delivers heated air through an "element pack" at a specified velocity. The element pack contains around 12 profiled heater element plates. Heat transfer elements are evaluated for their pressure drop and heat transfer performance across a range of velocity conditions. In the experimental data, these characteristics are measured and compared through friction factor for pressure drop, and heat transfer coefficient and Colburn number for heat transfer, across a range of Reynolds number values covering around 1000 to 3000.

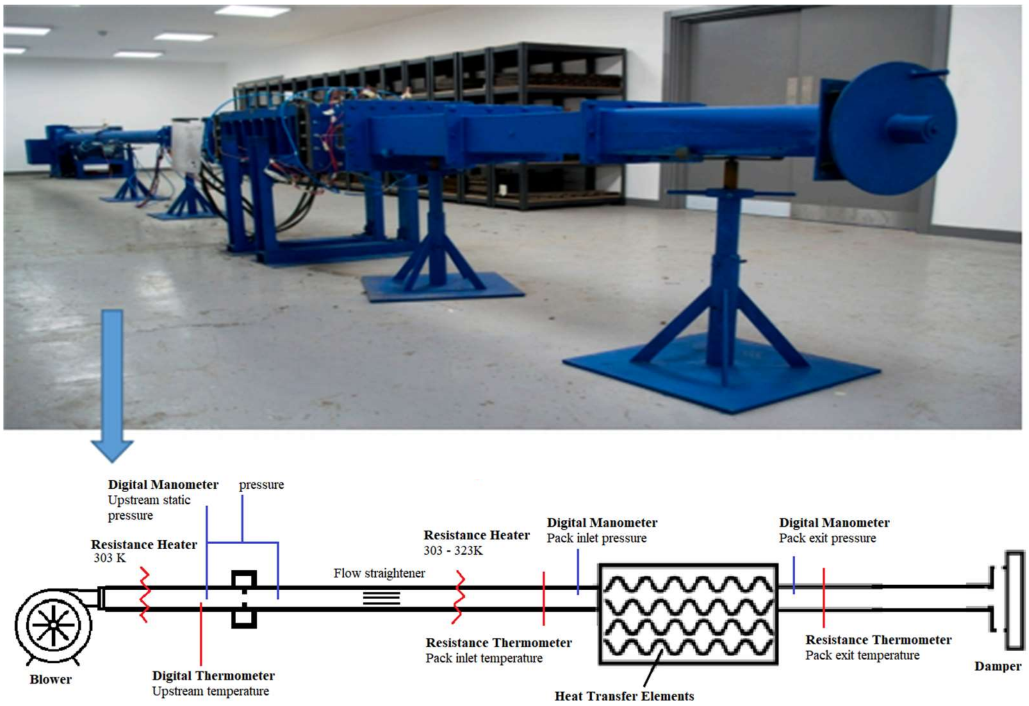

Figure 20. Picture and Diagram of Howden element test rig

Air is pushed through the system by a blower. It is heated to 303K by a copper wire resistance heater, before passing through an orifice plate flowmeter. The temperature is recorded upstream of the orifice plate with a digital thermometer, and the upstream pressure and orifice differential pressure are recorded with digital manometers. The flow then passes through a flow straightener, before reaching the second resistance heater. This copper wire heater raises the flow temperature according to a sinusoidal temperature variation, varying from 303 to 323 K over a time period of 25.71 seconds.

The temperature upstream of the element pack is recorded with a copper wire resistance thermometer. A resistance thermometer is chosen for its superior accuracy and stability compared to thermocouples and other temperature measuring devices (112). The pressure upstream of the element pack is measured with a digital thermometer across multiple tapping points; 3 on each side of the square duct for a total of 12.

The flow then travels through the element pack, where heat is transferred between the flow and heat transfer elements. The pack exit pressure is then measured with a digital manometer across multiple tapping points in the same configuration as the upstream location. A copper wire resistance thermometer measures the pack exit temperature. Finally, a damper is attached to the end of the duct. Closing this damper reduces the flow rate through the system, allowing for performance to be recorded across a range of velocity values.

The ambient pressure is measured through a barometer and the ambient temperature is measured with a digital thermometer.

3.1.1. Element pack measurements

The length and width of the element pack are measured using a tape measure. The thickness of the element plate is measured using a set of precision callipers.

The perimeter of the flow area between the plates is found by using tape. Tape is smoothly attached to the surface of the plate at the leading edge, ensuring that the tape is flush with the surface at every point. The edges of the plate are marked on the tape, and the tape is removed. The tape is placed on a flat surface and measured with a measuring tape. This is repeated for the opposite surface of the plate, and the other plate in the pair. The perimeter is calculated by adding the lengths of tape and the height of the wall at the side of the channel.

It is important to note that due to the configuration of the plate pairs, there may be two unique perimeter values.

The stack of elements is weighed on calibrated scales. The flow area is found via the pack porosity. The porosity is the ratio of open, or flow, volume to the total volume. Additionally, the ratio of the volume of the solid to the total volume is equivalent to one minus the porosity. The porosity is calculated using Equation 3.1.1 (113).

$$\phi = 1 - \frac{M_{pack}}{\rho_s \cdot L \cdot W \cdot H} \tag{3.1.1}$$

Where ϕ is the porosity, M_{pack} is the mass of the pack, ρ_s is the density of the solid material, L is the length of the pack, W is the width of the pack and H is the height of the pack.

Since the length of the pack and the plate thickness are constant, the porosity is also equal to the ratio of average flow area to the average total area of the pack at any cross-sectional plane normal to the flow direction. Therefore, the flow area can be calculated using Equation 3.1.2 (113).

$$A_{flow} = (1 - \phi) \cdot B \cdot H \tag{3.1.2}$$

Where A_{flow} is the flow area, B is the width of the pack and H is the height of the pack.

The standard form of hydraulic diameter for non-circular channels is calculated using Equation 3.1.3 (114).

$$D_h = \frac{4A_{flow}}{P_{Chann}} \tag{3.1.3}$$

Where D_h is the hydraulic diameter, A is the flow area, and $P_{channel}$ is the wetted perimeter.

This is adapted for the multiple channel scenario in Equation 3.1.4. Since only the total flow area is known, it is necessary to take the sum of the perimeters of the channels.

$$D_h = \frac{4A_{flow}}{\sum P_{chann}} \tag{3.1.4}$$

The plates are placed into the element chamber via the top opening. The top lid is placed over the elements, and compressed down until the height of the chamber matches the design value for the stack. This compression is achieved with a series of threaded rods inserted through a support structure into the top lid. Nuts are fastened to the rods above the support structure. As the nuts are tightened, the threaded rods push the top lid downwards. Precision callipers are used to measure the distance between the bottom and top inside walls to find the overall height.

3.1.2 Flow Measurements

The flowrate is measured using an orifice plate. An orifice plate is a plate with an opening in the middle that is smaller in size than the pipe or duct. This causes a decrease in pressure, which is directly related to the flow rate. By measuring the pressure drop across the orifice, the flow rate can be calculated using the orifice flow equation, which is adapted from Bernoulli's principle (115).

The pressure differential across the orifice is measured with upstream and downstream static pressure tubes connected to a digital manometer. The flowrate is calculated using equation 3.1.5.

$$\dot{m} = \frac{C_d}{\sqrt{1-\beta^4}} \cdot \epsilon \cdot A_{Orifice} \cdot \sqrt{2\rho_f \cdot \Delta P} \tag{3.1.5}$$

Where C_d is the orifice discharge coefficient, which is set depending on the geometry of the orifice. For straight edge, thin plates with no rounding around the orifice, this set as 0.61 (115).

β is the ratio of the orifice diameter to the duct diameter. The orifice is 101.63 mm or approximately 4 inches in diameter. The duct has a diameter of 153.19 mm or approximately 6 inches. Therefore β is 0.66342.

ϵ is the expansibility factor, which accounts for the density changes in compressible fluids passing through an orifice plate. It is calculated with equation 3.1.6 (116).

$$\epsilon = 1 - (0.41 + 0.35\beta^4)\left[\frac{\Delta P}{\kappa \cdot P_1}\right] \tag{3.1.6}$$

Where ΔP is the pressure differential across the orifice, κ is the isentropic exponent, approximately 1.4 for air, and P_1 is the upstream static pressure.

$A_{Orifice}$. is the cross-sectional flow area of the orifice.

ρ_f is the density of the fluid, calculated using the ideal gas law (Equation 3.1.7), and is reliant on local pressure and temperature (114).

$$\rho_f = \frac{P_{static}}{R \cdot T} \tag{3.1.7}$$

The static pressure, P_{static}, is the absolute static pressure and is taken immediately upstream of the orifice plate. *R*, the universal gas constant, is set as 286.9 *J/kgK* for air.

The overall velocity, $\bar{u}$, through the element test pack can be calculated using the mass flow continuity equation shown in Equation 3.1.8 (114):

$$\bar{u} = \frac{\dot{m}}{\rho_f \ \cdot A_{flow}} \tag{3.1.8}$$

Where A_{flow} is the cross-sectional flow area of the element test pack.

Finally, the Reynolds number is calculated using the Equation 3.1.9 (114):

$$Re = \frac{\rho_f \cdot \bar{u} \cdot D_h}{\mu} \tag{3.1.9}$$

The standard Reynolds number equation is adapted to replace *L*, the characteristic length, with the hydraulic diameter, D_h, to suit the channel flow scenario. μ is the dynamic viscosity of the fluid, which is sensitive to temperature changes. As such, a reference temperature must be chosen to evaluate the Reynolds number at, as the dynamic viscosity of the fluid changes slightly over the course of the temperature variation cycle. The temperature is defined as the midline of the inlet sinusoidal temperature curve, 313 K, as this represents the average value of the inlet temperature across the cycle.

3.1.2 Pressure drop performance

The pressure drop characteristics are measured through “friction factor”. This is a dimensionless scalable factor, allowing for easy comparison between test results. The friction factor is defined by the Darcy-Weisbach Equation, Equation 3.1.10 (117).

$$f = \frac{2 \cdot \Delta P \cdot D_h}{L \cdot \rho_f \cdot \bar{u}^2} \tag{3.1.10}$$

Where f is the friction factor, ΔP is the pressure drop across the element test pack and L is the length of the pack.

3.1.3 Heat transfer performance

The heat transfer coefficient is measured using the Cyclic Method. The Cyclic Method, as defined by Meek, determines the heat transfer coefficient of a solid geometry by directing a gas flow over it while periodically varying the gas inlet temperature in a sinusoidal pattern. This variation ensures that heat is transferred from the gas to the solid at higher temperatures and from the solid to the gas at lower temperatures. This approach prevents "heat soak," a condition in which the temperature of the solid acclimates to a constant gas inlet temperature over time. By analysing the amplitude of the inlet and outlet temperature fluctuations, the heat transfer coefficient can be calculated (118).

To quantify the heat transfer performance, the system's thermal response is interpreted using a dimensionless analytical model.

This model relates the logarithmic decay of the temperature amplitude to two key parameters: γ, the thermal response parameter, and St, the Stanton number, a dimensionless measure of the ratio of heat transferred into the fluid to the thermal capacity of the fluid. By incorporating both transient conduction in the solid and convective transport in the fluid, the model enables a more accurate estimation of the Stanton number, and by extension, the heat transfer coefficient. The balance between γ^2 and St^2 in the denominator reflects how the thermal behaviour is affected by convection (higher St) or conduction (higher γ).

It is important to note that this analytical model assumes an “infinite” thermal conductivity through the solid. This assumption is valid when the thermal conductivity of the solid is sufficiently high such that internal conduction does not significantly limit the overall heat transfer process.

The analytical model is presented in Equation 3.1.11.

$$\frac{m_f}{L} \cdot \log_e(\frac{\Delta T_I}{\Delta T_O}) = \frac{\gamma^2 \cdot St}{\gamma^2 + St^2} \tag{3.1.11}$$

Where:

$$\gamma = \frac{m_s \cdot \rho_s \cdot c_s \cdot \omega_o}{\rho_f c_f \bar{u}} \tag{3.1.12}$$

And:

$$St = \frac{h}{\rho_f \cdot c_f \cdot \bar{u}} \tag{3.1.13}$$

To solve for h, the heat transfer coefficient, this can be rewritten as:

$$h^2 + K_1 \cdot h + K_2 = 0 \tag{3.1.14}$$

Where:

$$K_2 = (m_s \cdot \rho_s \cdot c_s \cdot \omega_o)^2 \tag{3.1.15}$$

And:

$$K_1 = -\frac{K_2}{\rho_f \cdot c_f \cdot \bar{u} \cdot \frac{m_f}{L} \cdot \log_e\left(\frac{\Delta T_I}{\Delta T_O}\right)} \tag{3.1.16}$$

Where m_f is the hydraulic radius, L is the length of the solid geometry, ΔT_I is the amplitude of the upstream temperature variation, ΔT_O is the amplitude of the downstream temperature variation, St is the Stanton number, m_s is the surface area to volume ratio of the solid geometry, m_f is the hydraulic radius of the fluid, equal to $\frac{1}{4}D_h$, ρ_s is the density of the solid material, c_s is the specific heat capacity of the solid material, ρ_f is the density of the fluid, , c_f is the specific heat capacity of the fluid, ω_o is the angular frequency of the temperature oscillation, $\bar{u}$ is the average longitudinal velocity and h is the heat transfer coefficient.

For comparison purposes, the heat transfer coefficient is converted to a Colburn factor. To calculate the Colburn factor, the Prandtl number and Stanton number must be known.

The Prandtl number is the ratio of momentum diffusivity to thermal diffusivity in the fluid. It is defined in Equation 3.1.17 (114).

$$Pr = \frac{\mu \cdot c_f}{k} \tag{3.1.17}$$

Where:

Pr is Prandtl number, μ is dynamic viscosity, c_f is specific heat capacity of the fluid, and k is thermal conductivity. Each of these factors change with temperature, so, similarly to the dynamic viscosity, a reference temperature of 313 K is set for the value.

The Stanton Number is the ratio of heat transferred into a fluid to the thermal capacity of the fluid, determined by Equation 3.1.3 (114).

$$St = \frac{h}{\rho_f \cdot c_f \cdot \bar{u}} \tag{3.1.13}$$

Where the reference temperature for c_f is set as 313 K, matching the previous equations.

Finally, the Colburn factor, *J*, relates the heat transfer and mass transfer. It is defined by Equation 3.1.18 (114).

$$J = St \cdot Pr^{\frac{2}{3}} \tag{3.1.18}$$

3.2 Experimental Uncertainty

In any experimental measurement, some degree of uncertainty is inevitable due to limitations in equipment, environmental factors, and human influence. Understanding and quantifying these errors is crucial for assessing the accuracy and reliability of the results. This section discusses the potential sources of uncertainty in the experiment, their impact on the measurements, and methods to quantify the effect on the results.

In the context of computational modelling and experimental measurements, error refers to the difference between a measured or simulated value and the unknown true value. It is a single, realised deviation that cannot generally be known exactly because the true value is itself unknown.

Uncertainty, by contrast, quantifies the lack of confidence in a result. It represents an estimated range within which the true value is believed to lie, with a given level of confidence. Rather than attempting to pinpoint the exact error, uncertainty provides a statistical measure of the potential deviation based on known sources of variation such as discretisation, measurement noise, and modelling assumptions (119).

Each point of measurement has an associated uncertainty, and these stack up and combine to form a total error uncertainty associated with each result point. This section will discuss the methods of calculating uncertainties in experiments, following the techniques proposed by Coleman & Steele in Experimentation, Validation and Uncertainty Analysis for Engineers (119).

3.2.1 Methods of uncertainty propagation

There are two main calculation methods for the propagation of uncertainties; the Monte Carlo method and the Taylor series method.

The Monte Carlo method calculates the total uncertainty of a function by taking random values within the range of possible values of each component of the function and evaluating the function with those values. This process is repeated many times to give a range of values for the function. This range of values is formatted as a probability distribution of possible results, from which an overall uncertainty value can be derived.

The Taylor series method uses a first-order Taylor series expansion to approximate the function with a linear model. It can then evaluate the effect of the uncertainties of each of the input variables to the overall function uncertainty by considering the partial derivatives of the function with respect to each variable. This method is efficient and provides clear insights into the contribution of each input uncertainty. The first-order Taylor expansion provides a linear estimate of the uncertainty; using a higher order expansion can boost the accuracy of the approximation for non-linear functions but raises the complexity of the evaluation by a considerable amount.

These methods differ in their fundamental approaches: the Monte Carlo method is a probabilistic approach, and the Taylor series method is deterministic. The Taylor series method’s analytical technique is suited to systems with a low degree of non-linearity in their functions and small uncertainty values. It is efficient and straightforward to use but is limited in it’s versatility. The Monte Carlo method’s probabilistic distribution technique more accurately represents complex, non-linear system behaviour, with the caveat that requires significantly more computational resources and time to use (119).

This thesis will use the Taylor series method. There is an uncertainty value associated with each of the test points, resulting in a significant amount of calculation required. To use the Monte Carlo method for each of these points would be time consuming and inefficient. There is some degree of non-linearity in the system, however the reduction in accuracy is believed to be limited and acceptable for this scenario.

3.2.2 The Taylor Series Method

The Taylor series method is defined for the function of a number of variables:

$$r = r(X_1, X_2, \ldots, X_i) \tag{3.2.1}$$

Where *r* is the function, X_i are the unique variables.

The uncertainty in r, u_r, can be found using Equation 3.2.2.

$$u_r^2 = \left(\frac{\partial r}{\partial X_1}\right)^2 u_{X_1}^2 + \left(\frac{\partial r}{\partial X_2}\right)^2 u_{X_2}^2 + \cdots + \left(\frac{\partial r}{\partial X_i}\right)^2 u_{X_i}^2 \tag{3.2.2}$$

Which can be written in the compact form:

$$u_r^2 = \sum_{i=1}^{J} \left(\frac{\partial r}{\partial X_i}\right)^2 u_{X_i}^2 \tag{3.2.3}$$

The uncertainty magnification factor (UMF) measures the influence of the uncertainty of a particular variable on the overall uncertainty of the function.

$$UMF_i = \frac{X_i}{r}\frac{\partial r}{\partial x_i} \tag{3.2.3}$$

By dividing Equation 3.2.3 by r^2, and multiplying each term by $\left(\frac{X_i}{X_i}\right)^2$, which is equal to 1, it can be expressed in terms of the UMFs.

$$\left(\frac{u_r}{r}\right)^2 = \sum_{i=1}^{J}\left(\frac{X_i}{r}\cdot\frac{\partial r}{\partial X_i}\right)^2\left(\frac{u_{X_i}}{X_i}\right)^2 \tag{3.2.4}$$

This simplifies the evaluation process as $\frac{u_r}{r}$ and $\frac{u_{X_i}}{X_i}$ are fractional uncertainties.

For a function including components with exponents but not including any special terms such as logarithmic or trigonometric operators., Equation 3.2.4 can be reduced and simplified to Equation 3.2.5:

$$\left(\frac{u_r}{r}\right)^2 = \sum k_i^2\left(\frac{u_{X_i}}{X_i}\right)^2 \tag{3.2.5}$$

Where *k* represents the value of the exponent.

When a special term such as a logarithmic operation is present, it is necessary to use Equation 3.2.4.

3.2.3 Sources of Experimental Error

There are multiple possible sources of error throughout the process of testing the heat transfer element plates. Firstly, the dimensions of the element plates must be measured. For distance dimensions, two forms of measurements are used: a tape measure, and precision callipers. The tape measure is a standard metric tape measure with measurement divisions of one millimetre. Typically, the uncertainty of a measurement device is estimated as plus or minus half of the smallest division, thus the uncertainty of the tape measure is ±0.5 mm. For some measurements, such as the plate thickness and the pack height, small differences in the measured value make a large difference to the overall test results, thus a higher level of accuracy is required. For these measurements, precision callipers are employed. The precision callipers have a digital display that can measure with a resolution of 0.01mm, although the manufacturer's quoted accuracy is ±0.03 mm.

The pack is weighted on calibrated scales which have a resolution of 1 gram or 0.001 kg. The manufacturer has a quoted accuracy of 0.001kg.

The physical dimensions of the test rig are also measured. The overall test chamber width is measured with a measuring tape and the orifice diameter and duct diameter at the orifice are measured using precision callipers, to ensure reasonable accuracy in the mass flow calculation.

The pressure measurements are made with digital manometers, which have a resolution of 1 Pa, therefore the uncertainty is 0.5 Pa. The temperature is measured using a copper wire resistance thermometer, which has a quoted accuracy of 0.15 K from the manufacturer.

Table 1. Sources of uncertainty in experimental test rig

	Source of Uncertainty	Measurement method	Uncertainty	Unit
Element Physical Dimensions	Length of pack	Tape measure	0.5	mm
	Width of pack	Tape measure	0.5	mm
	Height of pack	Precision Callipers	0.03	mm
	Plate Thickness	Precision Callipers	0.03	mm
	Weight	Calibrated scales	0.001	kg
	Perimeter	Tape measure	0.5	mm
Test Rig Dimensions	Test chamber width	Tape measure	0.5	mm
	Duct diameter	Tape measure	0.5	mm
	Orifice Diameter	Precision Callipers	0.03	mm
Flow Measurements	Barometric pressure	barometer	100	Pa
	Orifice static pressure	digital manometer	0.5	Pa
	Orifice differential pressure	digital manometer	0.5	Pa
	Pack upstream pressure	digital manometer	0.5	Pa
	Pack downstream pressure	digital manometer	0.5	Pa
	Pack upstream temperature	Resistance thermometer	0.15	K
	Pack downstream temperature	Resistance thermometer	0.15	K

3.2.4 Experimental Uncertainty Analysis

Following the Taylor series method, the experimental uncertainties were evaluated to find the final uncertainty value associated with Reynolds number, friction factor and Colburn factor. The uncertainty value changes for each of the test points due to the mixture of absolute and fractional uncertainty values: for example, the ±0.5 Pa uncertainty of a digital manometer may be 1% of a 50 Pa measurement or 0.5% of a 100 Pa measurement.

The uncertainty of the Reynolds number, friction factor and Colburn factor across the range of test points is shown in Table 2. The uncertainty of the Reynolds Number is around 0.7%, the friction factor has an uncertainty of around 1.8%, and the Colburn factor uncertainty peaks around 3.7%.

The uncertainty of the friction factor decreases with increasing Reynolds number, due to the constant absolute uncertainty values of smaller measurements resulting in a larger percentage error.

For the similar reasons, the Colburn factor uncertainty increases with Reynolds number. The temperature measurement is the main driver of the uncertainty; although highly precise, the resistance thermometer's uncertainty is amplified by the small temperature amplitude at the pack outlet throughout the cycle. At higher Reynolds number, the pack outlet temperature amplitude is higher, resulting in a lower percentage uncertainty.

Table 2. Uncertainties of experimental test results

	Percentage Uncertainty		
Test Point	Reynolds Number	Friction Factor	Colburn Factor
3300	0.69%	1.63%	2.81%
3100	0.69%	1.63%	2.92%
2900	0.69%	1.64%	3.01%
2700	0.69%	1.65%	3.11%
2500	0.69%	1.65%	3.36%
2300	0.70%	1.66%	3.41%
2100	0.70%	1.68%	3.45%
1900	0.71%	1.73%	3.52%
1600	0.74%	1.83%	3.67%

3.3 CFD Set Up

Simulating the airflow through an air preheater can be extremely difficult due to the large and complex structure. The complexity requires a very fine mesh structure, requiring enormous amounts of computational power to fully model, making it unfeasible and inefficient for research purposes. It is therefore necessary to simplify the model where possible and prioritise the model to focus on a specific aspect of the RAPH. For example, in studies involving the leakage properties, the wheel of elements may be simplified to a solid disk with porous properties such that the air flow, pressure, velocity and heat transfer characteristics are replicated, without modelling the individual elements.

This difficulty is seen in experimental studies as well. To test an element profile, Howden use a single stack of elements to find pressure drop and heat transfer characteristics, due to size limitations.

For the purpose of this study, where the airflow within an element pack will be studied with great detail, it is inefficient to model a full pack of elements. Instead, it is more efficient to model a pair of element plates, with the use of periodic boundaries to replicate the rest of the flow through the element pack. As the whole pack is made up of identical element pairs, one pair of elements should provide enough information to correctly model the flow conditions and generate accurate results.

Additionally, to further conserve computational power, only a small section of the model is used. As the profile is a repeated pattern over the element plate, it can be useful to model a small part of the element plate and use periodic boundaries to replicate the rest of the plate. This allows a further reduction in cell count, allowing for faster and more efficient simulations to be run.

The STAR-CCM+ simulation is set up as a turbulent implicit unsteady flow regime, with the use of the segregated flow solver and the WALE Large Eddy Simulation (LES) solver. The temperature oscillation is implemented with Equation 3.3.1.

$$T_{inlet} = 313K + 10\sin(2\pi \cdot 0.03889 \cdot t) \tag{3.3.1}$$

Where: T is temperature (Kelvin) and t is time (seconds).

This equation ensures that the inlet flow temperature completes a full sinusoidal oscillation with 303K minimum and 323K maximum temperatures in 25.71 seconds, identical to the experimental set up.

3.3.1 CAD Model

The element plate models are created in Solidworks CAD software following manufacturing drawings supplied by Howden, shown in Figure 21, Figure 22 and Figure 23. These 3D models are imported into STAR-CCM+. A fluid region is generated as a box surrounding the plates, with the top and side edges of the box in contact with the plate. This creates distinct fluid channels, with periodic boundaries set up at the top and bottom, and left and right surfaces of the fluid region. Conjugate transfer interfaces are set up on all contact faces between the air and solid regions.

Figure 21. FNC element plates modelled in Solidworks.

Figure 22. "HS8" double undulated element plates modelled in Solidworks.

3.3.2 Selection of Physics Model

The appropriate selection of physics models is imperative to a successful simulation. While various physics models may result in similar numerical results, it is important to understand the strengths and weaknesses of each model in regard to the priorities of the investigation. There are 4 main turbulence models commonly used in CFD studies: Reynolds averaged

Figure 23. Herringbone style HC7a element pair modelled in Solidworks

Navier Stokes (RANS), large eddy simulation (LES), detached eddy simulation (DES) and direct numerical simulation (DNS). RANS is the only one of these which can be used in time-independent simulations.

RANS resolves the flow by solving the Navier Stokes equations, averaging the components over time. This results in a mean flow solution, facilitating a simpler approach to turbulence modelling. Turbulent fluctuations are accounted for using turbulence models, such as k-ε or k-ω. These turbulence models estimate the overall impact of turbulence on the flow using key properties such as turbulent kinetic energy (*k*), rate of dissipation (ε) or specific dissipation rate (ω). This allows the flow to be predicted with reasonable accuracy without the burden of calculating each turbulent fluctuation.

RANS tends to be more computationally efficient but can be lacking in visualising the detailed turbulent flows. Therefore, it is useful for providing insight into mean flow behaviour, and performance characteristics such as pressure drop and heat transfer but may be insufficient to analyse the finer details of the turbulent flow structures within a model. (120)

LES provides a higher fidelity approach by resolving the larger scale turbulent eddies in the flow and modelling smaller scales using sub-grid scale models. This method captures transient features and fluctuations in the turbulent flow structures, providing a more accurate representation of the finer detailed turbulent flows than RANS. This allows for in-depth analysis of turbulent flows, vortex structures, flow separation zones and wake regions.

LES provides good technical information about the turbulence within a flow, at the cost of an increased computational power requirement. Studies have shown that LES provides greater accuracy in both quantitative measurements and qualitative data when compared with RANS. Results more accurately follow experimental data, and the turbulence has a closer resemblance to experimental data when viewed, as shown in Figure 24 (121).

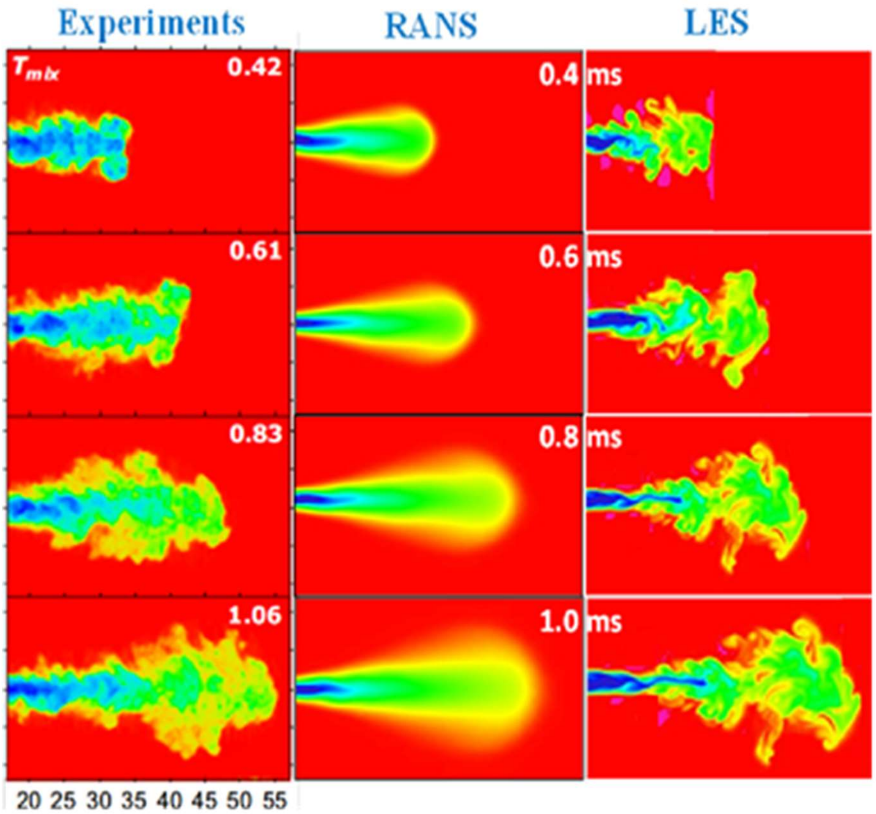

Figure 24. Comparison of turbulence in RANS and LES models to experimental data. (121)

DES is a hybrid technique that combines the strengths of RANS and LES. Near solid boundaries and within attached flow regions, the DES model utilises RANS modelling to maintain computational efficiency. In turbulent flow regions, LES modelling is employed to capture the flow phenomena accurately. This approach allows for better prediction of complex turbulent behaviours without the full computational cost of LES. It was originally developed to reduce the computational cost of using LES model to simulate flow over aeroplane wings and is mostly used in this area today (122).

There have been multiple studies comparing turbulence models in various scenarios. One study compared RANS, DES and LES with a physical experiment for the flow through an air-cooled radiator and found that LES accurately predicted both the numerical results and the visual flow structures accurately. The DES model's predictions were slightly less accurate, but within acceptable margins, and whilst the RANS model displayed visually similar, albeit time-averaged, flow structures, some of the quantitative measurements varied from the experimental value by up to 20%. The study also measured the time taken to run the models and found that RANS was 43% faster than DES and 65% faster than LES. (123) Another study compared LES and DES models for flow through a channel and found while

DES performed well, it failed to model near-wall turbulence effects, and LES closely matched the predicted result. (124) Furthermore, an investigation into the use of CFD to model heat transfer in confined channels found that LES provided the closest approximation of experimental results. (125)

DNS models resolve the flow in its entirety, including all scales of turbulence. This naturally results in a high level of accuracy but demands an enormous amount of computation power. The mesh must be fine enough to accurately resolve turbulent interactions at the smallest scales, and it is estimated that the number of operations grows at a proportional rate to the cube of the Reynolds number. Hence, for most studies it is unrealistic to attempt to use this model. DNS, however, has been useful for understanding turbulence, and has been instrumental in developing turbulent approximation models, such as LES and DES (126).

It is clear that LES offers the highest level of accuracy of the three physics models but requires the largest computational power. This is appropriate for studies requiring a deep analysis of the flow patterns and turbulence structures. DES is a good compromise, offering advanced turbulence modelling with slightly reduced accuracy in some cases, whilst using less computational power. This is ideal for detailed analysis, where time or computational power is somewhat limited. RANS offers a good approximation of the flow but fails to capture complex turbulent interactions. This allows some quantitative analysis whilst remaining extremely computationally efficient. This is appropriate for preliminary design assessments, or other scenarios where finer flow details are less critical.

The current study aims to create a model that accurately replicates the physical test rig, but also endeavours to analyse the detailed turbulent interactions and their effect on the performance of the model to advance future development. Therefore, LES is the appropriate choice of turbulence model.

LES is widely used in the study of heat transfer and vortex generators. Wang et al. used an LES model validated against previous experimental work to study cylindrical vortex generators (127). Jiansheng et al. validated an LES code of a plain rectangular channel with experimental results before adding cube shaped vortex generators (128).

Sohankar created a CFD model to compare the LES and DNS physics models for the case of angled rectangular winglets, finding that the LES model corresponded with the DNS results very well, whilst requiring significantly less computational power (129).

3.3.3 LES model

The LES physics model simulates flow by solving the filtered Navier Stokes equations, which are derived by applying a spatial filtering operation to the instantaneous Navier Stokes equation. The solution variables are decomposed into a filtered value and a "sub-grid" value, which correspond to large-scale resolved and smaller-scale unresolved values.

The instantaneous Navier-Stokes equations for incompressible flow are comprised of the continuity equation:

$$\sum \frac{\delta u_i}{\delta x_i} = 0 \tag{3.3.2}$$

And the momentum equation:

$$\frac{\delta u_i}{\delta t} + \frac{\delta u_i u_j}{\delta x_j} = -\frac{1}{\rho}\frac{\delta P}{\delta x_i} + v\frac{\delta^2 u_i}{\delta x_j x_j} \tag{3.3.3}$$

Where:

u is velocity components, *P* is pressure, ρ is fluid density, *v* is kinematic viscosity and *x* is the spatial co-ordinate. In vector notation, these equations can be written:

$$\nabla.(\boldsymbol{u}) = 0 \tag{3.3.2a}$$

$$\frac{\delta \boldsymbol{u}}{\delta t} + \nabla \cdot (\boldsymbol{u}\boldsymbol{u}) = \frac{-\nabla P}{\rho} + v\nabla^2 \boldsymbol{u} \tag{3.3.3a}$$

The LES filter is applied to the spatial field via the velocity component. The filtered velocity is calculated with Equation 3.3.4:

$$\overline{u_\imath}(\boldsymbol{x}, t) = \int_{-\infty}^{\infty}\int_{-\infty}^{\infty} G(\boldsymbol{x} - \boldsymbol{r}) u_i(\boldsymbol{r}, t) d\boldsymbol{r} \tag{3.3.4}$$

Where $\overline{u_i}$ is the filtered velocity, $\boldsymbol{x}$ is the spatial position vector, $\boldsymbol{r}$ is the integration variable over the spatial domain, and *G* is the filter function.

Applying the filter to the Navier Stokes equations:

$$\nabla.(\overline{\boldsymbol{u}}) = 0 \tag{3.3.5}$$

$$\frac{\delta\overline{\boldsymbol{u}}}{\delta t} + \nabla\cdot(\overline{\boldsymbol{u}\boldsymbol{u}}) = \frac{-\nabla\bar{P}}{\rho} + v\nabla^2\overline{\boldsymbol{u}} \tag{3.3.6}$$

Note that the overbar accent represents a filtered property.

Finally, the filtered Navier Stokes equations are derived (130).

$$\nabla.(\overline{\boldsymbol{u}}) = 0 \tag{3.3.7}$$

$$\frac{\delta\overline{\boldsymbol{u}}}{\delta t} + \nabla\cdot(\overline{\boldsymbol{u}}\,\overline{\boldsymbol{u}}) = \frac{-\nabla\bar{P}}{\rho} + v\nabla^2\tau^{SGS} \tag{3.3.8}$$

Equation 3.5 is unchanged, but Equation 3.3.9 now features the τ^{SGS} term, known as the sub-grid scale stress tensor, and is utilised to resolve the $\overline{\boldsymbol{u}\boldsymbol{u}}$ term, via Equation 3.8:

$$\tau^{SGS} = -(\overline{\boldsymbol{u}\boldsymbol{u}} - \overline{\boldsymbol{u}}\overline{\boldsymbol{u}}) \tag{3.3.9}$$

The sub-grid scale, or SGS, stress tensor can not be computed directly, and thus an SGS model is employed to approximate the stress tensor and resolve the equations. This is the computational representation of the physical eddy filtering; large turbulent structures are directly resolved, and smaller structures are approximated by an SGS model.

There are a variety of SGS models available with a range of strengths and weaknesses. There are 3 main models in wide use today: the Smagorinsky model, dynamic Smagorinksy model and WALE model.

The Smagorinsky model was one of the earliest SGS models and was used widely across the industry. The model is based on a concept of eddy-viscosity, where the effects of turbulence are estimated as turbulent viscosity. The viscosity is treated as proportional to the rate of deformation of the large-scale eddies. This results in a simple and computationally efficient approximation of the turbulence at sub-grid scales, however it lacks in accuracy near walls and requires fine tuning of a model coefficient, C_w, for different flow conditions (131).

The Dynamic Smagorinsky model was introduced by Gernamo et al. as an improved version of the Smagorinsky model to eliminate the requirement of fine tuning for each flow configuration. This was achieved via a “dynamic” approach, where C_w , which was previously user set, is now calculated throughout the simulation based on the flow’s current state. The calculated constant allows the model to “dynamically” adapt to different flow conditions. This facilitated an increase in accuracy over the previous model and made the model easier to use, however it also resulted in an increase in the computational power demand and was still inaccurate near the wall (132).

The wall-adapting local-eddy viscosity (WALE) SGS model is a modern approach designed specifically to improve accuracy in the near-wall region. This was achieved by adjusting the calculation of the eddy viscosity to decrease as the distance to the wall is reduced. This facilitates improved capture of flow behaviour close to surfaces. However, the WALE model does not feature the dynamic adapting ability of the Dynamic Smagorinsky model, so C_w is once again fixed. However, testing and validation has shown that the model coefficient is not as sensitive in the WALE model, and a single set value can predict flow behaviour accurately across a wide range of flow configurations (133). The resulting model provides sufficient accuracy to facilitate the analysis of complex turbulent features across a variety of scenarios, ensuring that the model is the most popular in modern day LES simulations (134).

3.3.4 Fluid energy and heat transfer model

In CFD, the fluid energy equation describes how thermal energy is transported and transformed within a fluid domain. This is essential for accurately modelling heat transfer processes, including convection, conduction, and radiation. The fluid energy equation is derived from the first law of thermodynamics, which details the conservation of energy.

The general form of the governing energy equation is shown in Equation 3.3.10 (135).

$$\frac{\partial(\rho_f E)}{\partial t} + \nabla \cdot \left(\rho_f \vec{u} E\right) = -\nabla \cdot (\vec{q}) + \Phi + S_E \tag{3.3.10}$$

Where ρ_f is the fluid density, E is the Total specific energy, $\vec{u}$ is the velocity vector, $\vec{q}$ is the heat flux vector, Φ is the viscous dissipation term and S_E is the energy source term.

This energy equation is solved alongside the Navier Stokes equations to predict the temperature and heat transfer behaviour throughout the fluid domain.

3.3.5 Solid physics model

In CFD simulations, the treatment of solid regions is an essential aspect of accurately modelling and simulating fluid-solid interactions. While the fluid regions are typically governed by the Navier Stokes equations, solid regions require different formulations to predict their behaviour.

In rigid solid bodies, where stress, strain and other mechanical effects are not considered, the governing equation is limited to the energy equation. This is a form of the general energy conservation equation applied to solid materials. It states that the rate of change of internal energy within the solid is equal to the net heat conduction plus any additional heat generation.

$$\rho_s c_v \frac{\partial T}{\partial t} = \nabla \cdot (\kappa_S \nabla T) + Q_s \qquad (3.3.11)$$

Where ρ_S is the solid material density, c_v is the solid material specific heat capacity, T is the temperature, k_s is the solid material's thermal conductivity, ∇T is the temperature gradient and Q_s is the user-specified internal heat source.

The heat conduction term is a form of Fourier's Law of Heat Conduction, shown in Equation 3.3.12.

$$\dot{q} = -k \cdot \nabla T \qquad (3.3.12)$$

Where $\dot{q}$ is the local heat flux vector.

The solid region is modelled as a rigid, stationary, constant density region. The material is set as mild steel, with the properties detailed in Table 3.

Table 3. material properties of mild steel

Material	Density (kg/m3)	Thermal Conductivity (W/mK)	Specific Heat Capacity (J/kgK)
Mild Steel	7850	63.9	486

3.3.6 Conjugate Heat Transfer

Conjugate heat transfer (CHT) refers to the analysis of heat transfer between a solid and fluid. It is a model which simultaneously evaluates convection in the fluid domain, conduction in the solid domain, and the heat flux at the boundary between the two to ascertain the overall heat transfer between the mediums. This is particularly useful in scenarios where thermal energy moves across solid-fluid interfaces, such as in heat exchangers, cooling of electronic components, and turbine blades (10).

In STAR-CCM+, CHT is solved by simultaneously computing the energy equations for both the fluid and solid domains, ensuring conservation of total heat flux at the interface. At a conjugate heat transfer contact interface, the solver iteratively balances the heat flux between the solid and fluid boundaries, while accounting for additional user-specified heat transfer if necessary, as shown in Equation 3.3.13 (135).

$$\dot{q}_f + \dot{q}_s = -S_u \tag{3.3.13}$$

Where $\dot{q}_f$ is the heat flux from the fluid boundary, $\dot{q}_s$ is the heat flux from the solid boundary and S_u is the user-specified heat flux across the interface.

The heat flux is calculated from the difference in temperature at the boundary using Fourier's Law of Conduction (10).

$$\dot{q}_{wall} = \frac{T_2 - T_1}{R} \tag{3.3.14}$$

Where R is the thermal resistance across the boundary.

The solver iteratively computes the temperature at each boundary using Equations 3.3.15 and 3.3.16, balancing the heat flux until a converged solution is reached.

$$\dot{q}_f = -\frac{S_u}{2} + \frac{T_{w_s} - T_{w_f}}{R} \tag{3.3.15}$$

$$\dot{q}_s = -\frac{S_u}{2} + \frac{T_{w_f} - T_{w_s}}{R} \tag{3.3.16}$$

3.3.7 Boundary Conditions

The boundary conditions for the fluid region are established to closely replicate the experimental setup.

A velocity inlet is defined with an inlet velocity corresponding to a range of pack Reynolds numbers between approximately 1000 and 3000. The velocity is uniform and normal to the inlet plane.

The turbulence at the inlet is characterized by turbulence intensity. Turbulence intensity is a measure of the strength of turbulence in a fluid flow, expressed as a percentage of the mean flow velocity. For internal, lower-speed flows, a turbulence intensity value of 1-5% is typical (136).

A turbulence intensity value of 1% is chosen based on the relatively low-speed flow and the presence of flow straighteners upstream of the test chamber in the experimental test rig. These factors suggest that the turbulence at the inlet to the test chamber is minimal.

The pressure outlet is set to atmospheric pressure, consistent with the test rig, where the flow exits to atmospheric pressure via a damper. The damper serves to regulate the flow provided by the inlet blower but does not need to be modelled in the CFD since the inlet velocity is already defined.

The CFD domain is shown in Figure 25. Periodic boundary conditions are applied to the left, right, top and bottom surfaces. The left-right periodic pair simulates the effect of a wider section of plate, while the top-bottom periodic pair mimics a larger stack of element plates while modelling only two. This approach reduces the overall domain size, thereby decreasing both computational power and time requirements.

For the solid region, boundary conditions are specified at the top, bottom, leading edge, and trailing edge surfaces of the heat transfer plates, where conjugate heat transfer interfaces are applied. The side edges of the solid region are set as periodic boundaries to ensure consistent heat transfer and temperature distribution across the fluid periodic boundaries.

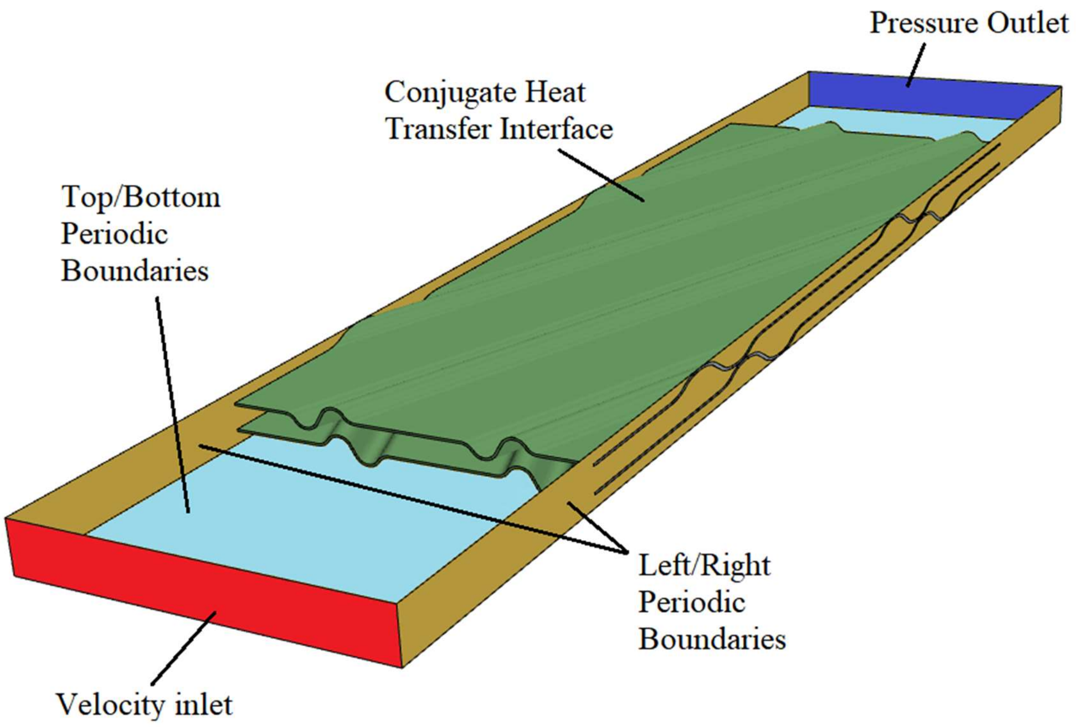

Figure 25. CFD domain and boundaries. Top boundary hidden to view interior of domain

3.3.8 Initial conditions

The simulation is set up with initial conditions matching the expected conditions of the test. This allows faster residual convergence, reducing the computation time and power requirements.

The initial flow velocity in the longitudinal direction is set to an estimated value of the average velocity through the pack.

The temperature of the solid region is set as a gradient in the longitudinal direction, with the inlet side being a higher temperature than the outlet. The values of the gradient are estimated from previous tests. There is typically a period of time, around 5-10 cycles, depending on the geometry, for the temperature gradient to stabilise. By establishing this gradient from the outset, the stabilisation time is significantly reduced, resulting in a more efficient simulation.

3.4 Measuring Data

The element profiles are analysed through the pressure drop and heat transfer performance. The CFD simulation is set up to replicate the experimental conditions as much as possible.

The flow area is measured in Solidworks with the measure tool. The mass flow rate is recorded across the inlet pressure plane, and Equation 3.1.4 is used to calculate the velocity through the pack.

Planes are set up to mimic the measurement points in the experimental set up, upstream and downstream of the element test pack. Area-averaged pressure and temperature readings are taken across these planes throughout the test cycle. The pressure drop is taken as the average difference between the inlet and outlet pressure readings across the cycle. The inlet and outlet temperatures are recorded throughout the cycle, and plotted to a graph.

3.4.1 Reynolds Number

The Reynolds number is derived from the inlet velocity. The inlet mass flow rate is measured from the inlet pressure measurement plane, and the pack velocity is calculated using the mass flow continuity equation, Equation 3.1.8. This method differs slightly from the experimental method as the velocity can be reliably measured in CFD with sufficient mesh quality, so an orifice plate or other flow measurement device is not required (137).

$$\bar{u} = \frac{\dot{m}}{\rho_f \cdot A_{flow}} \tag{3.1.8}$$

The Reynolds number is then calculated using Equation 3.1.9, as in the test rig. Calculation of the hydraulic diameter follows a similar method to the test rig, where the perimeter and flow area is measured in the CAD software.

$$Re = \frac{\rho_f \cdot \bar{u} \cdot D_h}{\mu} \tag{3.1.9}$$

3.4.2 Pressure Drop

The pressure drop is measured as the difference between the upstream and downstream pressure measurement planes, matching the upstream and downstream measurement points on the test rig. The measurement is implemented in Darcy's friction factor, Equation 3.1.10, following the experimental method.

$$f = \frac{2 \cdot \Delta P \cdot D_h}{L \cdot \rho_f \cdot \bar{u}^2} \tag{3.1.10}$$

Where ΔP is the pressure drop across the element pack, D_h is the hydraulic diameter of the element, L is the length of the element pack, ρ_f is the density of the fluid and $\bar{u}$ is the overall velocity through the pack.

3.4.3 Heat Transfer Coefficient

There are a few methods to calculate the heat transfer coefficient. The experimental test rig uses Meek's Cyclic Method, and this method can also be used in the same way for the CFD simulation, as it closely resembles the experimental method.

However, with CFD simulations, more analytical data is available. The heat flux at the boundary can be calculated, allowing the heat transfer coefficient across the fluid-solid interface to be measured, which is considerably simpler and more efficient to use. To compare with the cyclic method, this value must be time-averaged and area-averaged across all heat transfer surfaces.

The general form of the heat transfer coefficient derives from Newton's law of cooling, as shown in Equation 3.4.1.

$$h = \frac{\dot{q}}{T - T_{ref}} \tag{3.4.1}$$

Where:

h is heat transfer coefficient, q_{con} is the conduction heat flux at the boundary,
T is boundary temperature, T_{ref} is reference temperature.

For conjugate heat transfer problems, this is modified to find the heat transfer coefficient at the boundary, as shown in Equation 3.4.2.

$$h_{surface} = \frac{\dot{q}_{boundary}}{T_{boundary} - T_{ref}} \tag{3.4.2}$$

Where $\dot{q}_{boundary}$ is the heat flux at the boundary, $T_{boundary}$ is the temperature of the boundary. These assume that the simulation has converged fully, and therefore the heat flux and temperature of the solid and fluid sides of the boundary are equal.

The selection of an appropriate reference temperature is key to an accurate heat transfer coefficient result. In many simple heat transfer problems, this can simply be set as the ambient or atmospheric temperature. For heat exchangers, it is typically set as the bulk temperature of the fluid, but is defined as a characteristic temperature of the fluid (114).

To simplify the selection of the reference temperature, the specified Y+ heat transfer coefficient is utilised. This parameter defines the reference temperature as the temperature at a specified Y+ value, removing ambiguity around a reference temperature chosen by the user. The Y+ value is set at 100 in this case, as it is the recommended value in the STAR-CCM+ documentation, and has shown to correlate well to experimental data (138).

Using this method, the instantaneous local heat transfer at each cell on the boundary can be calculated, using the instantaneous local heat flux, local cell area, and local bulk fluid temperature, as shown in Equation 3.4.3.

$$h_{local} = \frac{\dot{Q}_{cell\ boundary}}{A \cdot (T_{cell\ boundary} - T_{Ref})} \qquad (3.4.3)$$

This is then spatially and temporally averaged for the full heat transfer surface and temperature variation cycle, as defined by Equation 3.4.4.

$$\bar{h} = \frac{1}{\tau A} \cdot \int_{\tau_0}^{\tau_1} \int_{A} h_{local}(x, y, z, t) \cdot dA \cdot dt \qquad (3.4.4)$$

Where $h_{local}(x, y, z, t)$ is the local heat transfer at a point with spatial co-ordinates (*x, y, z*) at a time, *t*, τ is the time period, τ_0 is the time at the start of the period, τ_1 is the time at the end of the period.

The cyclic method shall be employed to validate the simulation, and the boundary heat flux method will be recorded and compared with the validated cyclic method results. Providing they are equivalent within a reasonable degree of accuracy; the simpler heat transfer measurement method will be employed.

The heat transfer is converted to Colburn factor via the process detailed in Section 3.1.3.

3.5 CFD Model Validation and Verification Method

The CFD model employed in this study is validated and verified in accordance with the methodology defined in ASME V&V 20: Standard for Verification and Validation in Computational Fluid Dynamics and Heat Transfer (139).

Verification refers to the process of ensuring that the numerical algorithms implemented in the CFD solver correctly and consistently solve the governing equations. It addresses the question of whether the equations are solved accurately, but does not evaluate how well the equations represent physical reality.

Validation, on the other hand, is the process of assessing how accurately the CFD model replicates real-world behaviour. This is achieved by comparing simulation outputs against experimental data at defined validation points. The discrepancy between the simulated and measured values is used to quantify a modelling error, which contributes to the overall validation uncertainty of the predicted result.

3.5.1 Verification

For a commercial CFD software package such as STAR-CCM+, code verification is a critical part of the development and quality assurance process prior to public release.

STAR-CCM+ has undergone rigorous code verification procedures conducted by the developers, which typically involve solving a series of standard benchmark problems with known analytical, manufactured, or highly resolved numerical solutions. These exercises confirm that the implemented numerical schemes converge to the correct solutions as grid resolution is increased and that discretisation errors behave as theoretically expected.

Because STAR-CCM+ is a widely used, validated commercial product, its underlying code has already been verified for a broad range of fluid dynamics and heat transfer problems. As such, additional code verification by the user is not typically necessary. Case studies are available to independently verify the code (140–142).

3.5.2 Validation Method

The validation method follows that presented in ASME VV20. The method evaluates the total simulation uncertainty by considering the comparison error, uncertainty from the simulation software, inputs, and model, and the experimental uncertainty.

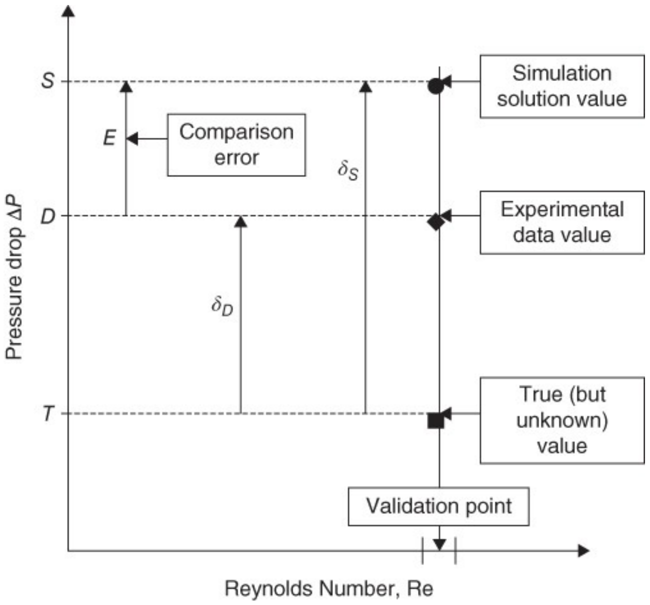

Figure 26. Diagram showing true, experimental and simulated data values and the associated errors arising from them (119)

Figure 26 demonstrates the errors found in simulation validation. *T* is the true value, *D* is the experimental data value, and *S* is the simulated value.

The difference between the experimental value and true value, is the experimental error:

$$\delta_D = D - T \tag{3.5.1}$$

The difference between the simulated value and true value is the simulation error.

$$\delta_S = S - T \tag{3.5.2}$$

E, the comparison error, is the difference between the simulated solution value and the experimental data value.

$$E = S - D = \delta_S - \delta_D \tag{3.5.3}$$

The purpose of simulation validation is to estimate the simulation error. The simulation error can be broken down into constituent parts.

$$\delta_S = \delta_{Model} + \delta_{input} + \delta_{num} \tag{3.5.4}$$

Where δ_S is the solution error, δ_{Model} is the error sourced from modelling assumptions and approximations, δ_{input} denotes the error due to input parameters, and δ_{num} is the error in the numerical solutions of the equations. In this scenario, δ_{Model} is unknown, further manipulation is required to estimate it.

Substituting in equation X,

$$E = \delta_{model} + \delta_{input} + \delta_{num} - \delta_D \tag{3.5.5}$$

Where δ_D is the experimental error value.

Rearranging,

$$\delta_{model} = E - \left(\delta_{input} + \delta_{num} - \delta_D\right) \tag{3.5.6}$$

As the true data value is unknown, the exact error for any of these parameters cannot be determined. Instead, corresponding uncertainty values are estimated as the standard deviation of the range within which each of the errors are expected to lie.

An overall validation uncertainty can be defined as the standard deviation of the combined effect of the error sources on the data value, provided that each of the uncertainty sources are independent.

$$u_{val} = \sqrt{u_{num}^2 + u_{input}^2 + u_D^2} \tag{3.5.7}$$

Therefore, the model error exists in the range of the comparison error ± the validation uncertainty, as shown in Equation 3.5.8.

$$\delta_{model} \in [E \pm u_{val}] \tag{3.5.8}$$

3.5.3 Numerical Uncertainty

The numerical uncertainty, u_{num}, arises from the discretisation of the governing equations and is assessed during simulation validation. To assess the numerical uncertainty, the

Richardson extrapolation and the Roache Grid Convergence Index (GCI) method are commonly used. Richardson extrapolation estimates the "true" solution value by analysing results obtained on successively refined grids, assuming that the discretisation error follows a predictable pattern related to grid spacing. The Roache GCI builds on this by providing a formal estimate of the numerical uncertainty based on the differences between these grid solutions. This approach accounts for the convergence behaviour of the solution and quantifies the uncertainty associated with the discretisation error (143).

The Richardson extrapolation is shown in Equation 3.5.9.

$$F = F_{exact} + g_1 H_{grid} + g_2 H_{grid}^2 + g_3 H_{grid}^3 + \cdots \tag{3.5.9}$$

Where *F* is the solution function value, the *exact* subscript indicates the true solution value, H_{grid} is the mesh grid spacing, and g_i are constants defined by the solution, independent of the mesh spacing.

The mesh grid spacing for three-dimensional simulations can be calculated using Equation 3.5.10 (144).

$$H_{grid} = \left[\frac{1}{N}\sum_{i=1}^{N} V_i\right]^{\frac{1}{3}} \tag{3.5.10}$$

Where *N* is the number of cells and V is the volume of a cell.

In the Roache estimate methodology, g_1 is set to zero, and the error is assumed to be closely related to the second order term. This is true for second order accurate numerical schemes, such as that of the LES physics model in STAR-CCM+.

The exact value of the solution function can then be defined using Equation 3.5.11.

$$F_{exact} = \frac{\left(H_{gri\ _2}^2 F_1 - H_{grid_1}^2 F_2\right)}{H_{gri\ _2}^2 - H_{grid_1}^2} \tag{3.5.11}$$

Where the subscripts 1 and 2 represent two mesh grids of fine and coarse resolutions respectively.

A grid refinement ratio, r_{grid}, is defined in Equation 3.5.12.

$$r_{grid} = \frac{H_{grid_1}}{H_{grid_2}} \tag{3.5.12}$$

Substituting Equation 3.5.11 into Equation 3.5.10, the formula can be simplified as in Equation 3.5.13.

$$F_{exact} = F_1 + \frac{(F_1 - F_2)}{\left(r_{grid}^p - 1\right)} \tag{3.5.13}$$

Where p is the order of the Richardson Extrapolation. For this case, it is set as 2.

A relative error factor *e* is defined in Equation 3.5.14.

$$e = \frac{F_2 - F_1}{F_1} \tag{3.5.14}$$

The estimated fractional error of the fine mesh grid solution, E_1 can then be calculated using Equation 3.5.15.

$$E_1 = \frac{e}{r_{grid}^p - 1} \tag{3.5.15}$$

This error value provides a reasonable estimate of the numerical error, but it does not guarantee that the true solution lies within the calculated deficit. Instead, it is more practical to define an uncertainty range that offers a higher level of confidence that the true solution value is contained within the specified bounds.

To determine the uncertainty range, a Grid Convergence Index (GCI) is proposed, shown in Equation 3.5.16. This introduces a safety factor, F_s, into the Equation 3.5.14 to account for the uncertainties in the estimation of the error. A safety factor of 3 is recommended when testing two mesh grids, and 1.25 when testing three or more (145).

$$GCI_{fine\ grid} = \frac{F_s|e|}{r_{grid}^p - 1} \tag{3.5.16}$$

This GCI is used directly to define the numerical uncertainty, as in Equation 3.5.17.

$$u_{num} = GCI_{fine\ grid} \tag{3.5.17}$$

3.5.4 Validation Uncertainty

For cases where the comparison value is found from a data reduction method, like the friction factor or Colburn factor as presented in this thesis, the uncertainty sources u_{input} and u_D are explicitly linked, as the simulation models the conditions of the experiment, and some of the inputs match that of the experimental data. The modified validation uncertainty equation is in Equation 3.5.18.

$$u_{val}^2 = u_{num}^2 + u_{input+D}^2 \tag{3.5.18}$$

Using the Taylor Series Method presented in Section 3.2.2, $u_{input+D}$ can be expressed in terms of the individual uncertainties of the variables, as in Equation 3.5.19.

$$u_{input+}^2 = \sum \left[\left(\frac{\partial S}{\partial x_i} \right) - \left(\frac{\partial D}{\partial x_i} \right) \right]^2 \cdot u_{x_i}^2 \tag{3.5.19}$$

Where *S* and *D* are functions of x_i variables.

For the case of the friction factor, calculated using Equation 3.1.10,

$$f = \frac{2 \cdot \Delta P \cdot D_h}{L \cdot \rho_f \cdot \bar{u}^2} \tag{3.1.10}$$

The data values are set as:

$$S_f = f_S$$

$$D_f = f_D$$

$$E_f = S_f - D_f = f_S - f_D$$

Where *f* denotes the friction factor.

Therefore, u_{inp} is expressed in Equation 3.5.20.

$$u_{input}^2 = \sum \left[\left(\frac{\partial f_S}{\partial x_i} \right) - \left(\frac{\partial f_D}{\partial x_i} \right) \right]^2 \cdot u_{xi}^2 \qquad (3.5.20)$$

Where x_i are the variables from Equation 3.1.10.

The uncertainty factors are then evaluated along with the comparison error to establish the model uncertainty. This validation method will be followed and presented in Section 4.

3.6 Meshing Technique

Mesh grid generation is a crucial step in the CFD simulation process. A mesh grid typically consists of a series of subdivisions of the simulation domain, facilitating the solving of the fluid dynamics equations. The equations are solved iteratively at each individual subdivision, or cell. These cells are often extremely small to conform to the shape of the geometry in the flow domain. This method is known as the Finite Volume technique. The quality and suitability of a mesh grid defines the level of accuracy in a simulation, (146).

The structure of mesh grids can be divided into 3 categories: structured, unstructured, and hybrid. A structured mesh contains cells composed in a regular, grid-like structure. The regularity of the cells simplifies the algorithm solving process, allowing for a computationally efficient simulation, reducing computational cost and time. The drawback is that complex geometries can not be well represented by this regular grid structure, and some accuracy is lost. Therefore, structured mesh grids are recommended for simple geometries, (135).

An unstructured mesh contains irregular shaped cells, such as tetrahedral (4 sided, e.g. pyramidal), hexahedral (6 sided, e.g. cuboidal) and polyhedral shapes (varied shapes and number of sides). The arrangement of these irregular shapes allows for increased flexibility in conforming to complex geometries. However, the irregularity complicates the algorithm solving process, resulting in an increased computational cost and time. Therefore, these grids are recommended for geometries that are too complex for structured grids.

A third option is the hybrid mesh, aiming to combine the advantages of both types. This is achieved by using structured grids in areas of simple geometry and transitioning to unstructured in more complex regions. This generally optimises computational efficiency accuracy in cases with a range of geometric complexities, (135).

Unstructured meshes tend to be the most common and versatile for modern CFD problems. There are various unstructured mesh types available, each suitable for different cases.

Tetrahedral Meshing is one of the fastest and most efficient meshing techniques, particularly when dealing with complex geometries. Tetrahedral cells are created using methods like the Delaunay triangulation, which is employed in STAR-CCM+. This method quickly generates a conforming mesh that efficiently handles intricate surfaces and irregular domains. However, despite its speed, tetrahedral meshes can require more cells to achieve the same level of accuracy as other types of meshes, especially when capturing fine details in the flow.

Polyhedral meshing was created to combine the benefits of tetrahedral and hexahedral meshing. Although sometimes considered less efficient in terms of generation time, polyhedral meshing offers a significant advantage in terms of mesh quality and solution accuracy. Polyhedral cells typically have around 14 faces and are generated through a dualisation scheme in STAR-CCM+. While this process is more computationally intensive during mesh generation, the resulting mesh can achieve similar or better accuracy than a tetrahedral mesh with 5 to 8 times fewer cells. This reduction in cell count leads to more efficient simulations overall, with fewer elements needed to resolve the same flow features, making it highly effective for optimising performance in complex flows, (147).

In conjunction with these main mesh generation techniques, other tools are available to further enhance the conformity and suitability of the mesh grid.

The prismatic layer is a layer of thin cells adjacent to a wall or boundary. The cells are typically hexagonal shaped, extruded normal to the boundary, and are stacked uniformly. This layer of cells aids in resolving the steep gradients of flow variables such as velocity and temperature that occur near walls, due to no-slip conditions or other boundary conditions. In general, the prism cell layers should fully encompass the fluid boundary layer.

Modern advancements in CFD mesh grids are wide and varied. Multiple studies have proposed “dynamic” mesh grids, where the mesh grid changes over the course of the simulation. This change can be to facilitate motion of a part, moving or deformation of boundaries, or adapting and refining the mesh in key areas. One study used a dynamic mesh to simulate the growth of fouling depositions within a heat exchanger, (148). Another study used a dynamic mesh to model the rotation of a rotor in a pump (149). Cant et al. developed a DNS CFD code with adaptive mesh refinement to effectively simulate a combustion problem. The adaptive mesh refinement significantly enhanced the efficiency of the simulation (150).

A particularly promising area of research involves the use of machine learning methods to generate unique unstructured meshes. One study created an artificial neural network trained to generate high quality mesh grids efficiently, finding that the generated mesh grids provide more accurate results than that of the current automated mesh generators available in commercial CFD software (151).

3.6.1 Mesh Sensitivity Analysis

A mesh sensitivity analysis was performed to find the appropriate mesh configuration to achieve a balance between accuracy and computational power requirements. This is done by generating a variety of mesh resolutions and configurations and testing them to compare to a known data value. In this case, the base size of the mesh cells, and the prism layers configuration were varied. The goal was to generate a mesh structure fine enough to capture the detail in the confined passages and ensure that the boundary layer was fully modelled within the prism layers, whilst keeping the number of cells to a minimum. This ensures that the results are accurate, and the simulation is efficient to run.

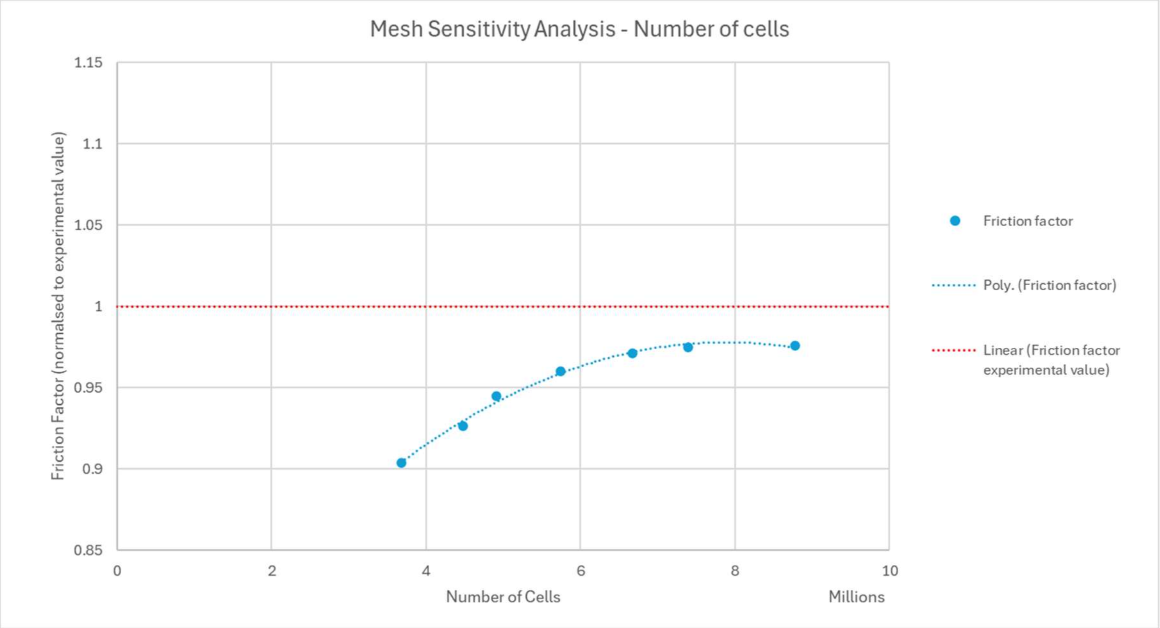

Figure 27. Mesh grid sensitivity analysis results – performance against number of cells compared with experimental data for friction factor

The FNoC part was modelled, with a pack Reynolds number of 2000. Mesh grids with cell base sizes of 10 mm to 2 mm were tested to compare the effect of the cell size and number of cells. The best configuration was then tested with number of prism layers varying from 3 to 10 to ensure the boundary layer effects were properly captured. The simulated values are compared against the experimental data for the same pack Reynolds number.

The results are shown in Figure 27. As expected, the simulated value approaches the experimental value as the number of cells increases. The accuracy limit was reached at around 6.5 million cells, and it is therefore inefficient to increase the number of cells past this point.

With the number of cells set at 6.5 million, the number of prism layers was varied to ensure the boundary layer was correctly represented. The results are shown in Figure 28. Increasing the number of prism cells brings the simulated value closer to the experimental result. An accuracy limit is reached at 8 prism layers, demonstrating that the boundary layer is modelled correctly. With 6.5 million cells and 8 prism layers, the simulated result is slightly higher than the experimental value, is within 1% of the value ,and is deemed sufficiently accurate for continued experimentation.

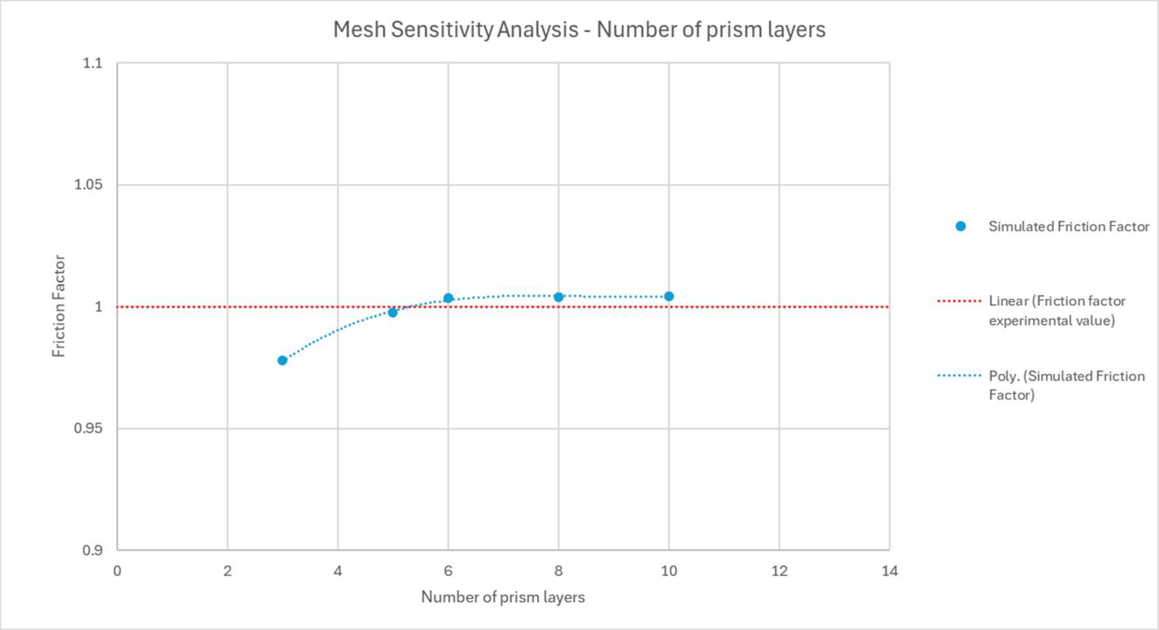

Figure 28. Mesh grid sensitivity analysis results – performance against number of prism layers compared with experimental data for friction factor

Another measure of mesh quality is through the wall Y+ values at the flow domain boundaries. Wall Y+ is a non-dimensional measure of distance from the wall, relating to the local velocity. It was defined by Prandtl, along with *u*+, the dimensionless velocity, in the

Law of the Wall to describe the behaviour of the flow within the boundary layer close to the wall, as shown in Figure 29. (152)

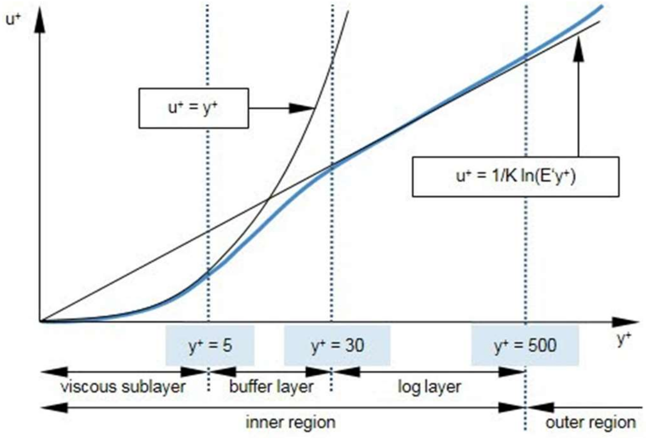

Figure 29. Relative velocity (u+) and distance (y+) near the wall

In CFD, the term can be used to describe how well the boundary layer is captured. In order to accurately model the boundary layer, the mesh resolution in this area must be sufficient to fully resolve the flow. One way to determine if this is the case is by checking the value of Y+ at the first layer of mesh cells. If the Y+ value is above 5, the viscous sublayer has not been solved. For most problems, a wall Y+ of around 1 ensures that the viscous sublayer is modelled correctly, and the boundary layer is fully captured. (146) This is particularly important for heat transfer problems, as the heat transfer at the surface is heavily reliant on the flow near the boundary.

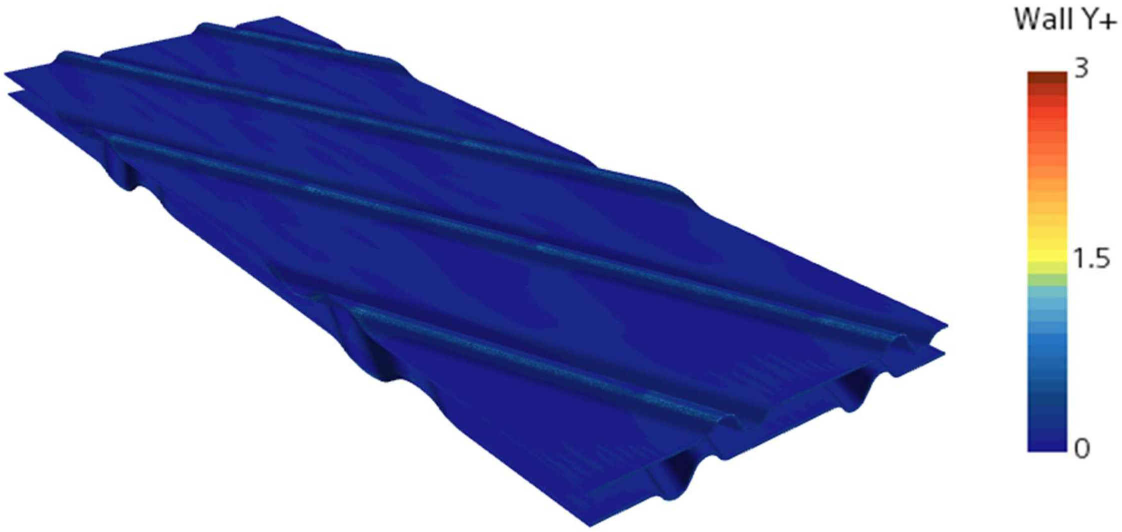

Figure 30. Y+ Values across surface of FNoC model

The Y+ over the heat transfer surfaces of the model is displayed in Figure 30. It is clear to see that the Y+ value is around 1 over the entire heat transfer boundary, ensuring that the boundary layer is fully captured, and the heat transfer can be simulated accurately.

3.6.2 Grid Convergence Index

Following from the findings of the mesh sensitivity analysis, a new fine and coarse grid were created with the optimal number of prism layers, in order to generate a reasonable comparison for the GCI.

The GCI was evaluated following the methodology presented in Section 3.5.3, and the results are presented in Table 4.

Table 4. Grid Convergence Index for FNoC mesh sensitivity analysis

	Friction factor	Colburn factor
GCI	0.021	0.027

4. Simulated Model Validation

This section discusses the validation of the CFD model and the quantification of the uncertainties and modelling error.

The heat transfer is calculated using the Cyclic method to replicate the experimental method. Additionally, the heat transfer rate is measured across the boundary. These values are compared to validate the software measurement of heat transfer coefficient as a reliable method.

Three element profiles are modelled and compared to experimental data to ensure accuracy and reliability of the CFD simulation across various geometries.

The element profile comparisons consist of the presentation of the experimental data, normalised to the fine mesh simulated value from the mesh sensitivity analysis. This normalisation protects Howden’s commercial interests, while allowing reasonable comparison between simulated and experimental data, and the different element types. A line of best fit is generated for the experimental results, and the simulated results are compared to it. Error bars are added to show the modelling error calculated in this section.

To provide insight into the performance of each element type, selected visualisations are presented in the form of surface heat transfer rate distributions and flow streamlines through the element channels. Although the simulation is time-dependent and governed by cyclic thermal conditions, a “snapshot” is shown to highlight key flow and thermal features. The time step chosen corresponds to the peak inlet temperature, where the temperature gradient between the inlet and outlet is greatest, and consequently, the surface heat flux is near its maximum. This enhances the visibility of local heat transfer behaviour across the element surfaces. While this does not represent the average condition over a full cycle, it serves as a useful reference point, particularly since the system exhibits periodic steady-state behaviour.

For the streamline visualisation, pressure drop was found to vary minimally over time, and velocity field monitoring indicates that the flow is fully developed and does not exhibit strong transient features during the cycle. Therefore, the streamline pattern at the selected time point is considered representative of the broader flow behaviour. Nonetheless, it is acknowledged that flow separation, recirculation, or secondary flows may vary subtly over the thermal cycle and are not captured in this single image. These visualisations are therefore used to qualitatively interpret trends in flow behaviour and heat transfer distribution, rather than to infer precise local behaviour at all time steps.

4.1 Simulation Modelling Error Analysis

The validation method from Section 3.5 was implemented to calculate the validation uncertainty and the overall model error for the fine mesh case used in the mesh sensitivity analysis.

The input uncertainty and experimental uncertainty is calculated using the simulated data, experimental data and experimental uncertainties. The experimental uncertainties at the lowest Reynolds number were used, as these are the highest uncertainties. This allows a single uncertainty value to be expressed across the Reynolds number range with confidence that the true value lies within the uncertainty range at each test point.

The validation uncertainties are displayed in Table 5. The uncertainties have been expressed as a fraction of the simulated value for the friction factor and Colburn factor to normalise for confidentiality reasons. The overall model error is therefore +3.3%, -2.5% friction factor, and +4.4%, -4.8% for Colburn factor, where the percentage is taken of the fine mesh simulated value at Reynolds number 2000.

Table 5. Simulation validation uncertainties

	Friction factor	Colburn factor
GCI	0.021	0.027
$\frac{u_{input+D}}{S}$	0.020	0.037
$\frac{u_{val}}{S}$	0.029	0.046
E/S	0.004	-0.002
$\frac{\delta_{model}}{S}$	0.4% ± 2.9%	-0.2% ± 4.6%

4.2 Heat transfer coefficient method validation

The heat transfer coefficient is recorded in the experimental test rig using the cyclic method. This method is complex and time-consuming, and it would be more efficient to utilise the heat flux method discussed in Section 3.4.3. To validate the heat flux method, both methods are tested and compared numerically for the FNoC model.

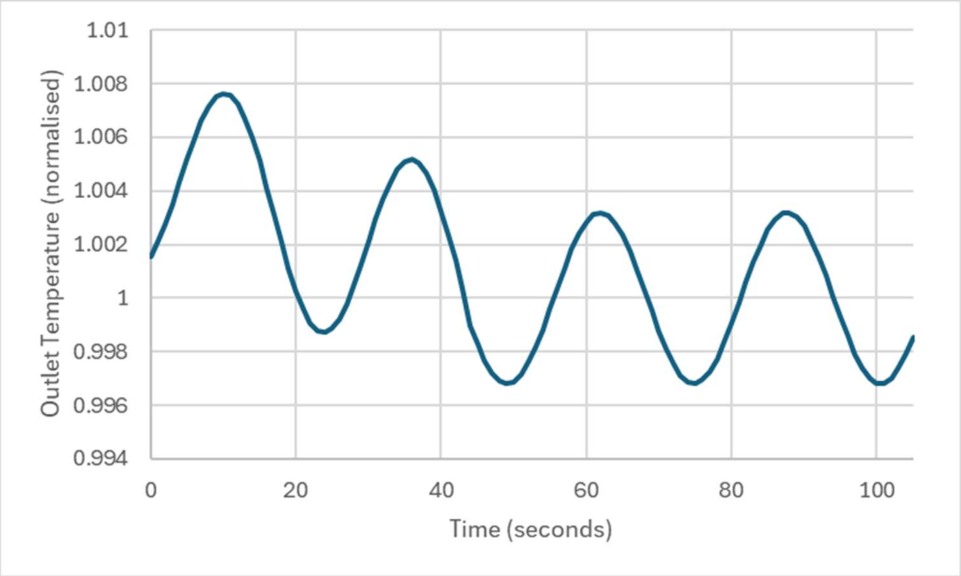

Figure 31. Validation: Outlet Temperature of FNoC with no initial temperature gradient, Reynolds number = 2000, numerical methodology used

Using the cyclic method, it takes multiple temperature cycles to properly establish the temperature gradient. This results in initially inconsistent output temperatures, until the temperature gradient is fully defined, at which point the outlet temperature becomes a steady sinusoidal curve, as shown in Figure 31.

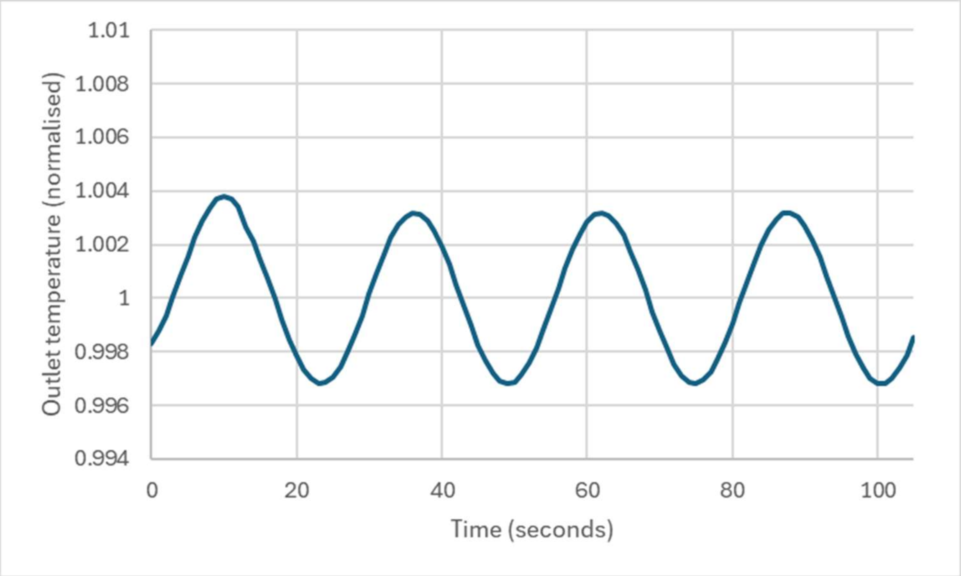

Figure 32.Validation: Outlet Temperature of FNoC with initial temperature gradient, Reynolds number = 2000, numerical methodology used

By setting the initial temperature of the heat transfer plates to the expected temperature gradient, the time taken to stabilise the outlet temperature is reduced. In Figure 32, the time is reduced to around 20 seconds.

Following this, the cyclic method was used to calculate the Colburn factor. The results were compared against the experimental data of the FNoC profile in Figure 33. Additionally, the heat flux method was used to calculate the Colburn factor, and was compared to the cyclic method and experimental results. Error bars are displayed with the modelling error calculated in the previous section, and are applied to the Cyclic Method data as the error has been calculated for that method.

The results show that the heat flux method follows the cyclic method data closely. The cyclic method value tends to be a little lower than the heat flux method value at each test point, but both methods represent the experimental data well, and the difference lies in the range of the modelling error.

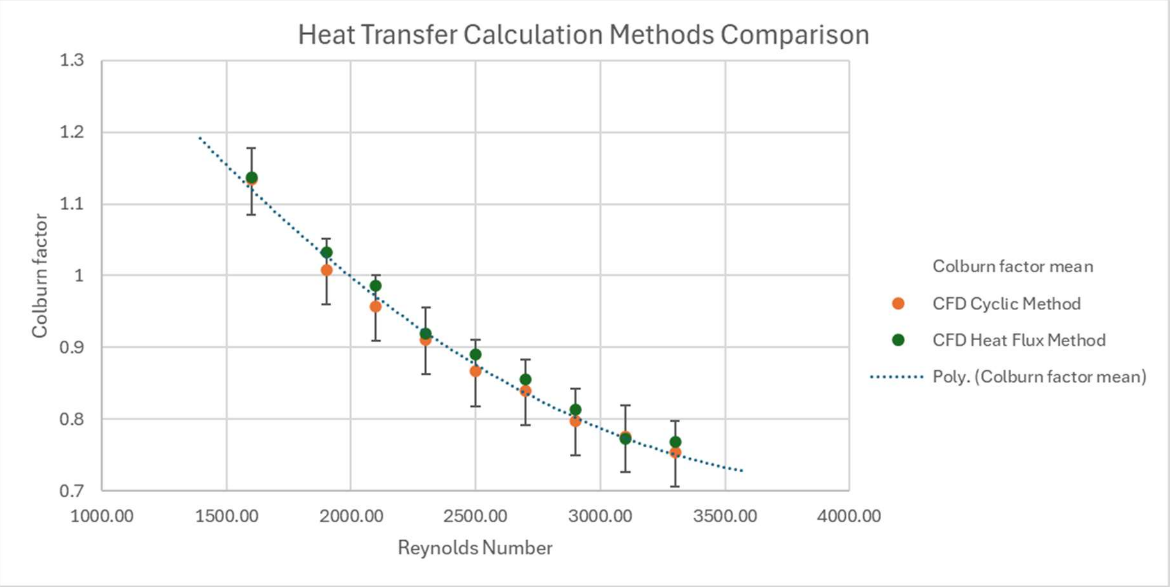

Figure 33. Comparison of simulated Colburn factor results for the cyclic method and heat flux method against experimental data for the FNoC profile

The difference in these values may be due to the difference in quantifying the energy transfer: the cyclic method assumes that the average inlet and outlet temperature readings are representative of the overall energy transfer, which may avoid capturing local variations in temperature. It may also smooth out short term fluctuations in heat flux, and diminish the effects of localised irregular heat transfer rates. In contrast, the heat flux method is sensitive to localised heat transfer, where lower quality mesh cells could incorrectly report heat flux. This could result in a slight over-estimation of the overall heat transfer rate. These differences are small but expected given that both methods measure the same energy transfer process while using slightly different approaches.

Therefore, it is determined that the heat flux method is a viable alternative to the cyclic method for the simulations undertaken in this thesis.

4.3 FNoC profile

The experimental results for the FNoC profile are presented in Figure 34 as a collection of test runs taken across a variety of dates. The test data is normalised for the fine mesh case simulated value. All tests were undertaken on the same batch of element plates to ensure consistency across results. There is a clear difference in the experiments from February and March of 2019, with the friction factor being consistently higher than other results. Results taken before and after this set of experiments are fairly consistent. This evidence points to a systematic error in experiments taken during this short time period.

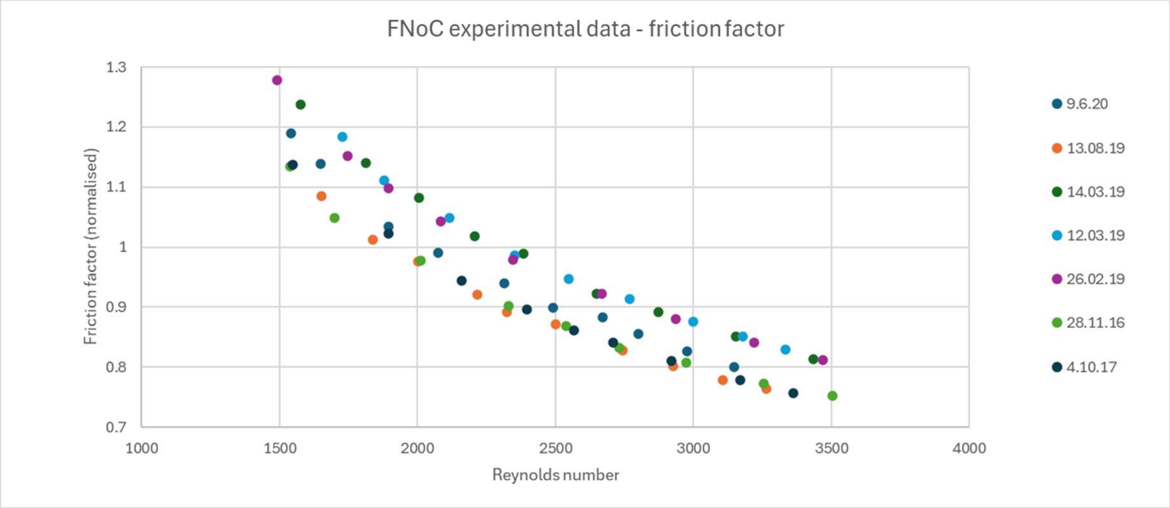

Figure 34. Experimental friction factor results data for FNoC for a variety of test runs

The systematic error may take the form of atmospheric conditions: whilst density and atmospheric pressure are measured, humidity is not. A change in humidity would alter the density of the air, resulting in a change in fluid resistance, and by extension friction factor. Another possible systematic error could be the deformation of the plates.

It is not likely that the plates deformed, as tests completed after the time period in question were in line with the previous lower friction factor results. However, it is possible that the compression of the plates in the test rig was incorrect. This would change the height of the notches and result in a change in the fluid channel area. In this case, it is believed that the element plates were over-compressed, reducing the height and the fluid channel area, resulting in higher fluid resistance and a higher pressure drop. The general volume of tests ran on the experimental test rig is low, so it is believed that the elements were left in the chamber across the 3-week period, explaining the consistency of the problematic results.

Whilst instruments falling out of calibration could be a factor, the data from the August 2019 experiment is in line with the previous data, and no calibrations were completed in the time between the February/March tests and the August test.

For the reason of the systematic error, the problematic results have been removed from comparisons.

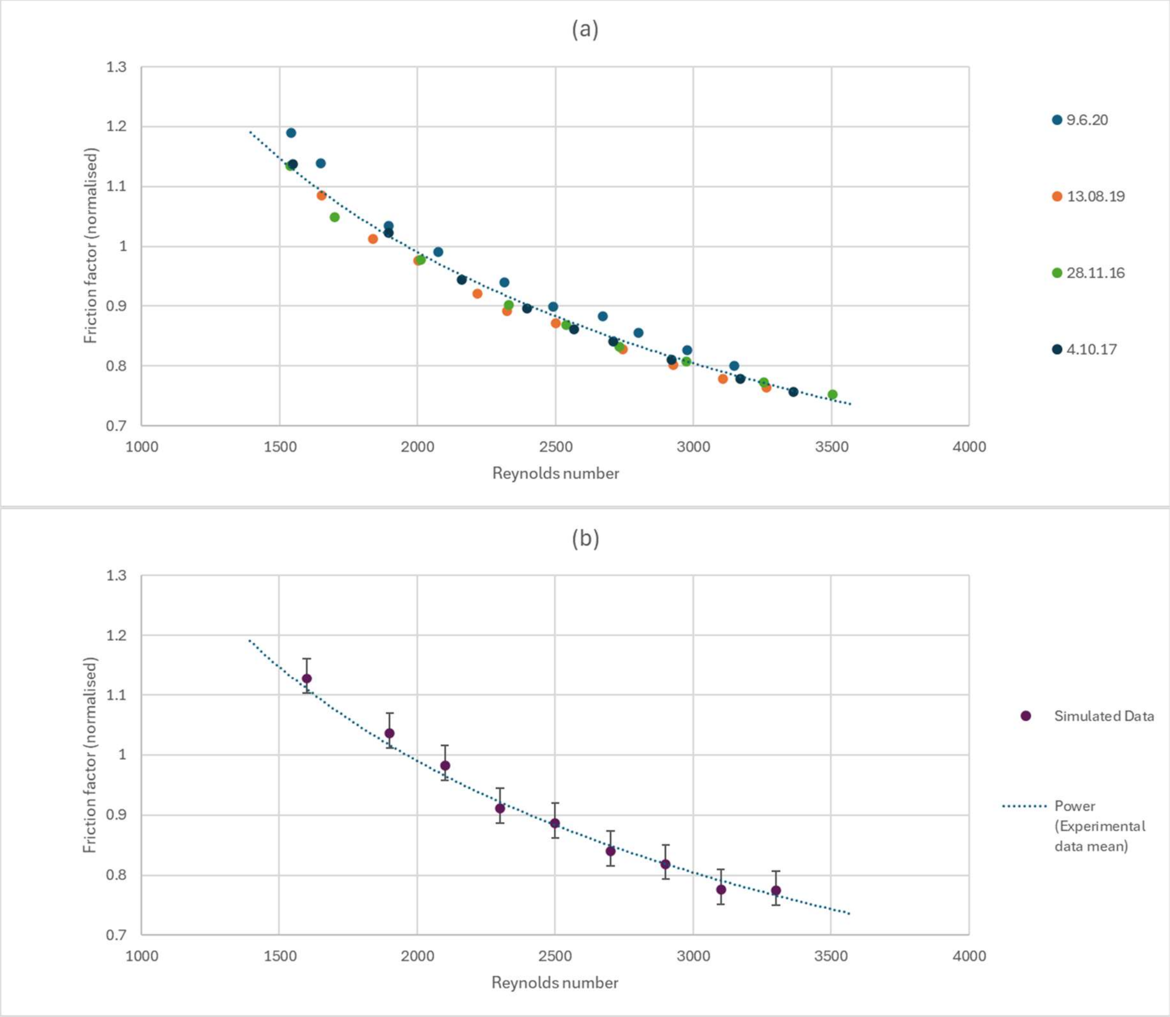

Figure 35. Experimental (a) and simulated (b) friction factor results for FNoC profile

The friction factor results are shown in Figure 35, (a) shows the experimental results and (b) shows the simulated results, with experimental data line of best fit and error lines showing the simulation modelling error. It can be seen that simulated the results correlate well to the experimental data, and the experimental data is within the modelling error range at each point.

The Colburn factor results are shown in Figure 36, (a) shows the experimental results and (b) shows the simulated results, with experimental line of best fit and modelling error bars. The experimental data had a particularly large scatter at the lower end of the Reynolds number range but had little variance at the higher Reynolds numbers. The simulated data fit reasonably well to the experimental average curve, although it does seem to slightly underestimate the Colburn factor. However, the experimental data falls within the modelling uncertainty range at each point.

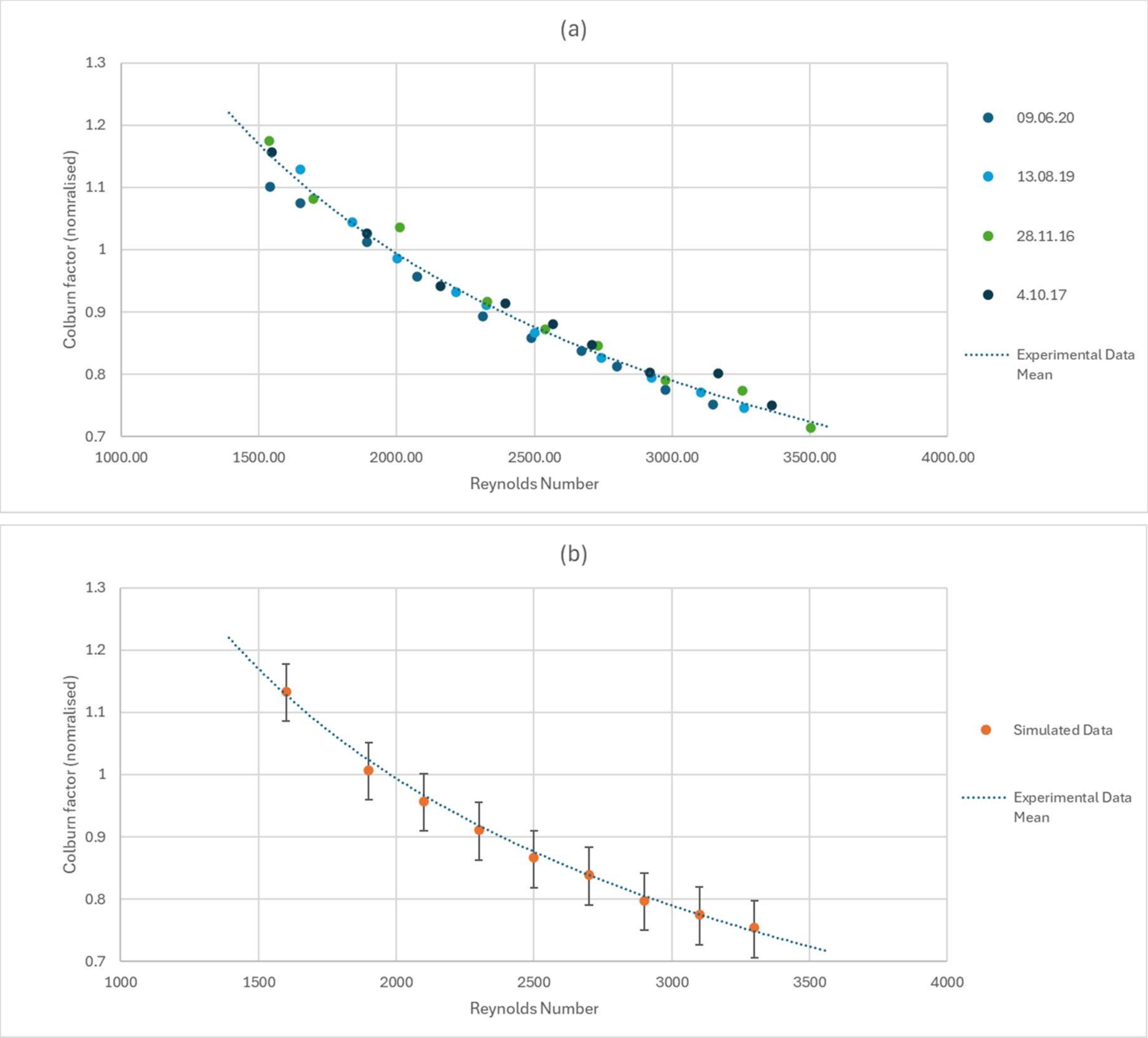

Figure 36. Experimental (a) and simulated (b) Colburn factor in FNC profile

It can be concluded that the simulation accurately resembles the experimental data for the FNC profile. This provides a solid foundation to continue testing work and begin to use the simulation as a “virtual test rig”.

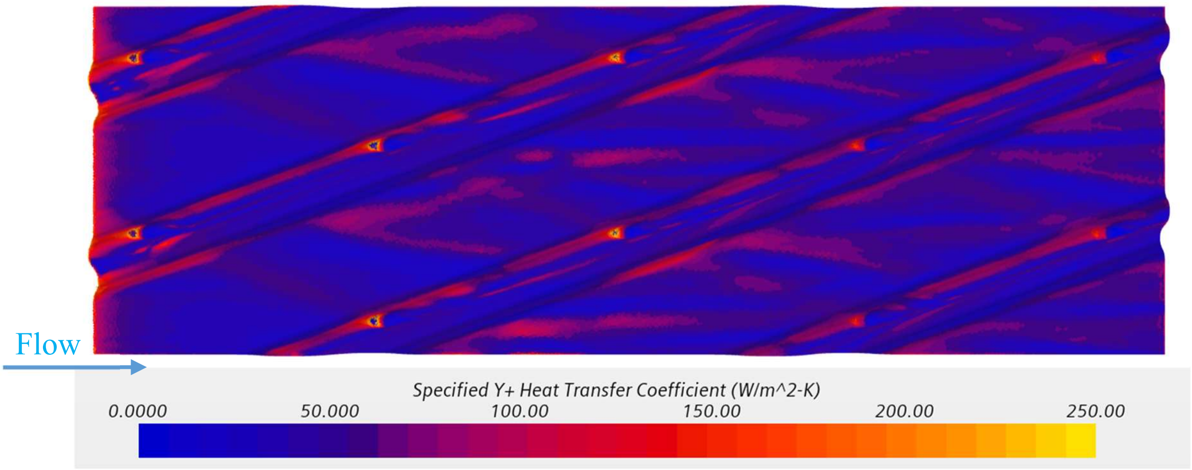

Figure 37. Heat Transfer Coefficient over FNC surface at 2000 Reynolds number

The heat transfer coefficient over the surface of the bottom element plate is shown in Figure 37. Areas of high heat transfer are observed along the front side of the peaks of the notches, with a maxima immediately upstream from the points at which the notches contact the opposing angled notches of the above plate. There are elongated finger-shaped areas of increased heat transfer running parallel to the flow. These areas expand and diverge over time and appear to originate at the trailing edge of the valley section of the notches. These are believed to be longitudinal vortex structures. The flow travelling over the peak impacts the trailing edge of the valley causing a disruption. This interaction can induce flow separation, leading to a formation of shear layers that roll up into vortices downstream. Additionally, the crossing notches from the top and bottom plates directing flow in opposing directions create a swirling or rotational motion within the flow. This can enhance the turbulence intensity and promotes the formation of vortex structures. The combination of this crossflow and the disruption from the trailing edge results in the generation of turbulent longitudinal vortex structures at these points. The longitudinal vortex structures promote turbulent mixing and facilitate an increased heat transfer at the plate surface.

In Figure 38, velocity streamlines are added, and the top plate is overlaid in a translucent fashion, to aid visualising the crossing notch features. The streamlines reveal a clear development from laminar to turbulent flow as the fluid travels through the channel. At the inlet, the flow is smooth and orderly, indicating laminar characteristics. However, as it progresses downstream, particularly around the mid-length of the plate, the streamlines begin to distort and exhibit unsteadiness, suggesting the onset of transition to turbulence. This transition appears to be triggered by the geometric disturbances introduced by the notches and undulations, which promote flow separation and instability.

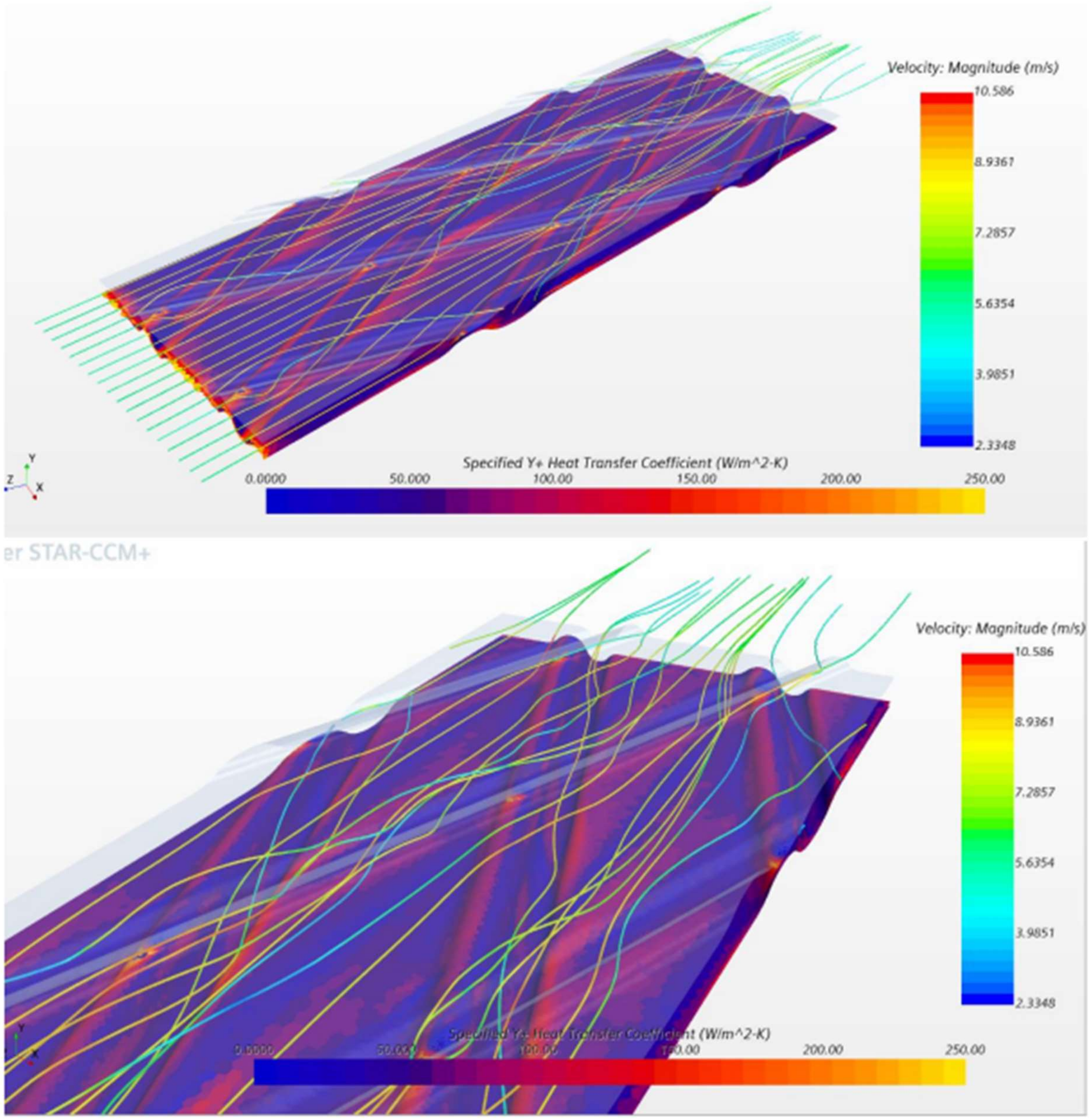

Figure 38. Heat transfer and velocity streamlines in the FNC model

Vortex structures become evident beyond this point, especially within the trough regions, where swirling motions are observed. These rotational flows likely stem from recirculation zones induced by abrupt changes in surface contour. As the swirling flow exits the troughs and interacts with the flatter surfaces, it rolls up into more coherent vortices, which further enhance mixing and contribute to the overall turbulence intensity in the domain.

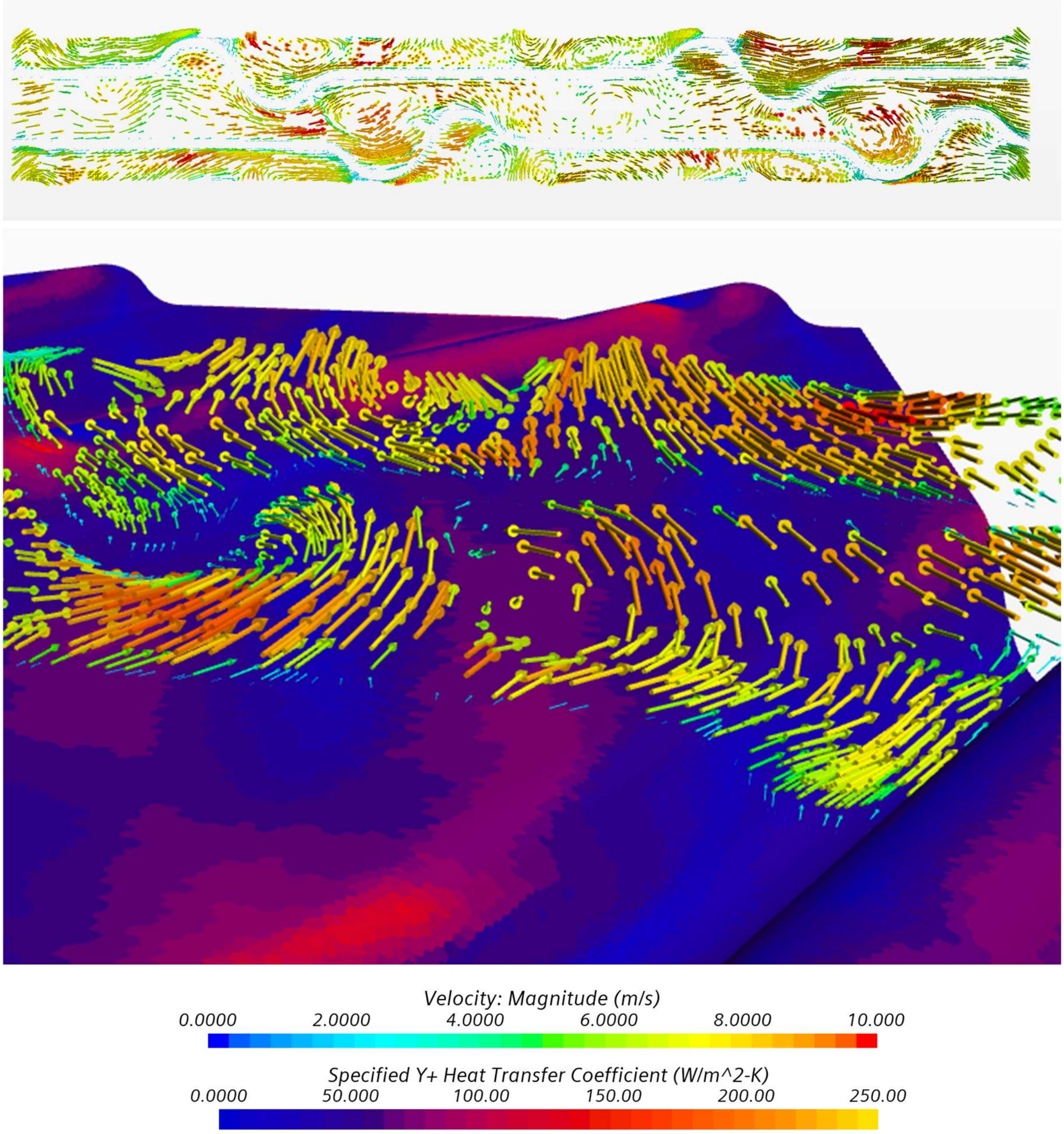

Figure 39. Velocity vector lines in the FNoC profile

The swirl flows within the trough areas is visible in the velocity vector lines visualisation in Figure 39. Additionally, the crossed notches create a crossflow effect, where the top plate directs the flow to the left and the bottom plate directs it to the right. This creates longitudinal vortex structures, which can be seen in the visualisation. These vortex structures enhance heat transfer by creating localised areas of increased heat exchange, which can be seen as irregular stripe patterns on the plate surface heat transfer visualisation (Figure 37). This increased heat transfer is due to vortex-induced turbulent flows disrupting the boundary layer, promoting greater convective heat transfer across the surface, and turbulent mixing bringing the hot flow in the middle of the passage towards the cool plate surface, reducing the temperature gradient and increasing the heat transfer efficiency.

4.4 Double Undulated profile

The HS8 double undulated (DU) model was simulated effectively. There was some variance in the results, but it is believed this is due to difficulties in creating the model: the transition from the straight notch to the angled corrugations is complex and proved to be problematic to model.

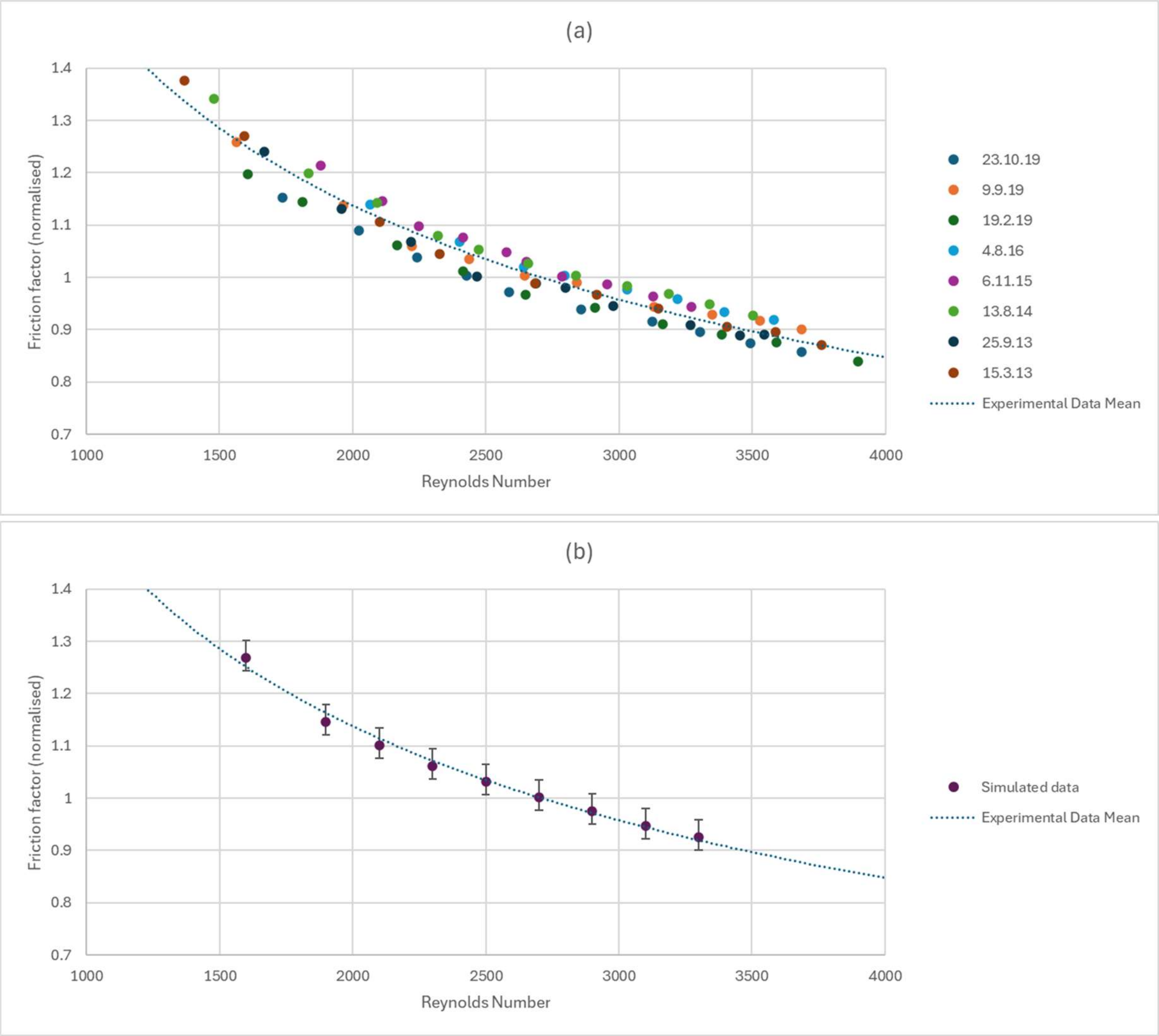

Figure 40. Experimental (a) and simulated (b) friction factor data for HS8 model

The results for the friction factor are shown in Figure 40, (a) shows the experimental results and (b) shows the simulated results, with experimental line of best fit and error limit lines. The experimental data has some scatter, which is reasonable as the test runs occurred across a large period of time. Differences across tests could result from environmental changes, such as the level of humidity, human error, as the tests were likely conducted by different operators, and slight differences in the sit up, like the level of compression applied to the lid of the chamber. The data is normalised to the FNoC fine mesh simulated value, as before. It is clear that the DU element type has a higher overall friction factor than the FNoC, which may be surprising considering it features a relatively open flow notch parallel to the flow direction. However, it is perceived that the undulated section and the corrugated plate create a significant pressure loss.

The data shows that the simulation predicts the pressure drop very well, with slight variances at lower Reynolds numbers. The experimental data is within the modelling error at each test point.

The Colburn factor results are shown in Figure 41, (a) shows the experimental results and (b) shows the simulated results, with experimental line of best fit and modelling error bars. The heat transfer is represented well, however there is some variance from the experimental data average, while remaining within the standard deviation. This is believed to be due to slight differences in the 3D model, because of the previously mentioned difficulty in creating the element in CAD.

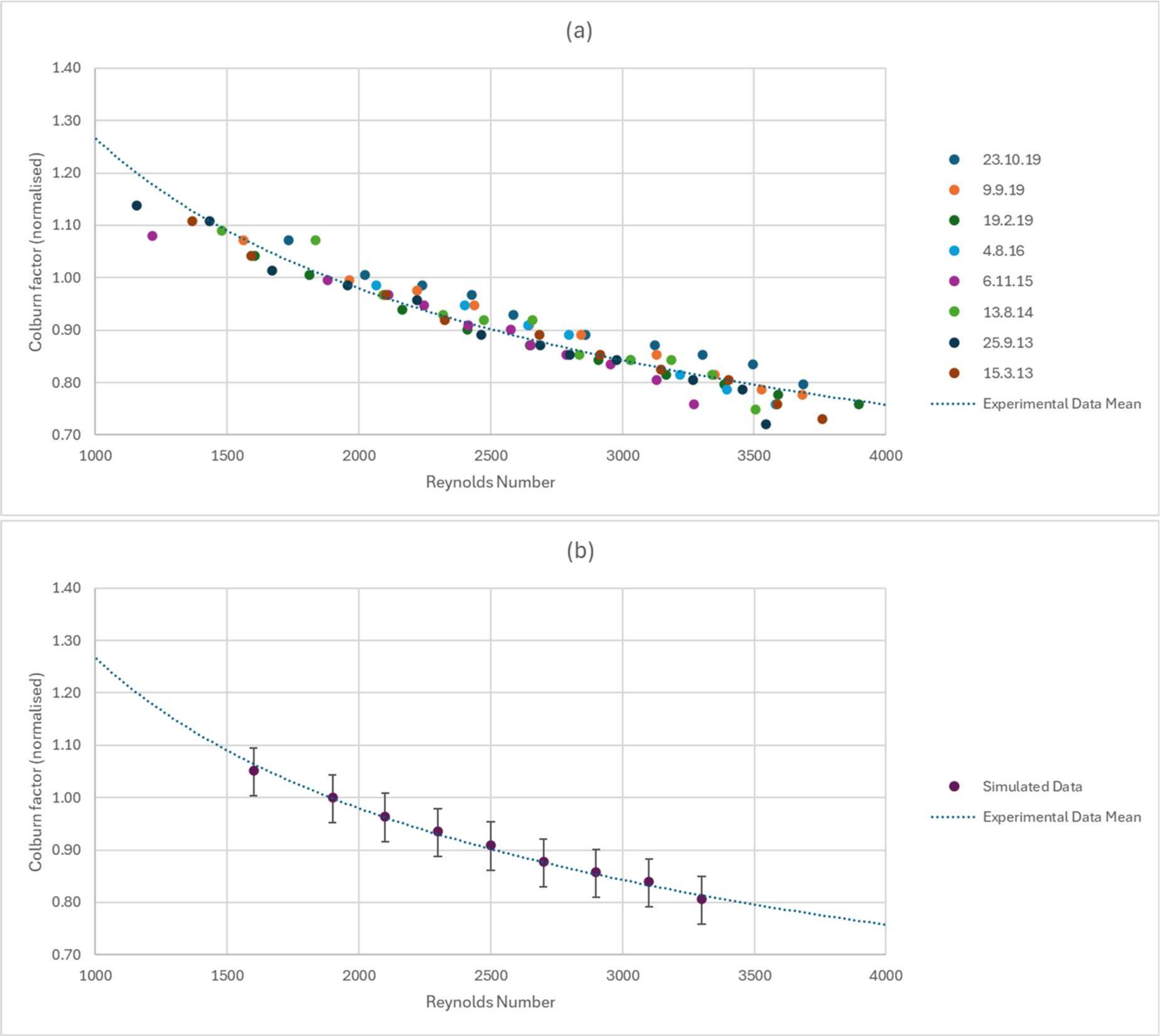

Figure 41. experimental (a) and simulated (b) Colburn factor data for HS8 model

Figure 42 shows the heat transfer across the surface of the plate, represented with the blue-red-yellow colour spectrum, and velocity streamlines to show the direction and speed of the flow. Areas of high heat transfer are on the front side of the undulations, and near the locations where the two plates are in contact. The high heat transfer rate on the front side of the undulations can be attributed to two flow factors: the air impacting the undulation and travelling over the top; and the air impacting the undulation and flowing along the bank until it reaches the notch. These flow phenomena essentially confirm the same fact: the geometry of the part in these areas is creating an extended contact surface, allowing more heat to be transferred.

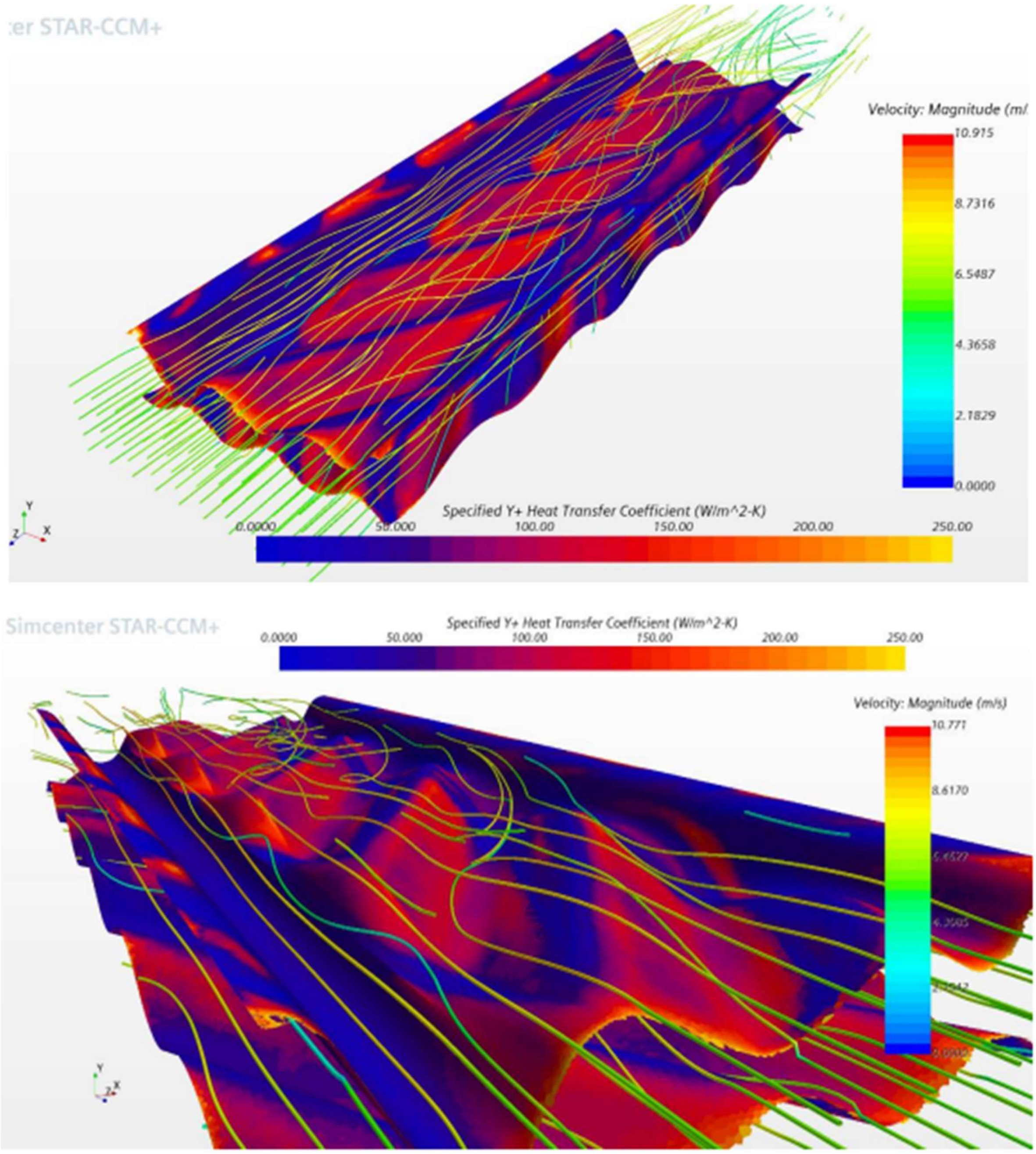

Figure 42. Heat transfer in HS8 with velocity streamlines

A similar statement can be made about the increased heat transfer where element plates are in close proximity: flow is being squeezed into a small area between the two plates, forcing the flow to contact with the plates, resulting in more heat being transferred to the elements. This is also why there is a lower heat transfer rate in the notch on the left side of the model. The flow is not being pushed or manipulated in any way to make contact with the plate in this area, so it simply flows straight through without transferring much heat. It is also important to note that the velocity of the flow is unaffected, which contributes to a lower pressure drop.

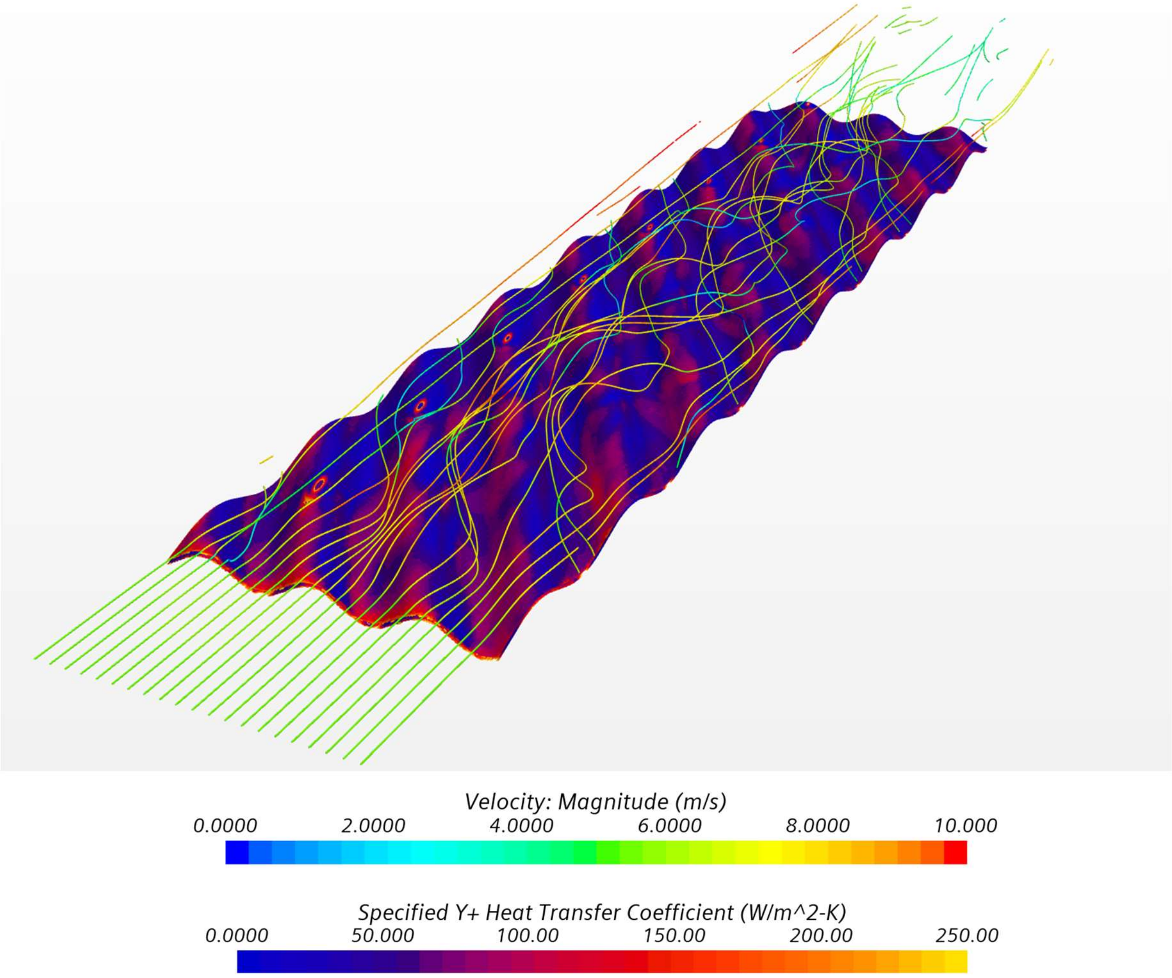

Figure 43. Heat transfer over HS8 bottom plate with velocity streamlines

Figure 43 shows the heat transfer and velocity streamlines over the bottom plate. It can be seen again there is increased heat transfer on the front sides of the undulations. It is also clear that heat transfer is increased in areas where the plates are in close proximity. Additionally, some interesting swirl flows are present here. The top and bottom plate are creating a crossflow effect, similar to the FNoC profile, but without the flat area in between crossed-features. This creates stronger vortex structures, and results in erratic flow, which is inefficient for pressure drop performance. It is clear that the induced turbulence is extremely intense, at some points to the detriment of the performance. The heat transfer over the surface of the FNoC profile increased towards the inlet, as the flow transitioned from laminar to turbulent. In the Double Undulated (DU) profile, the heat transfer appears to be higher near the inlet and decreases towards the outlet. This is a sign that the turbulence generated is inefficient and uncontrolled.

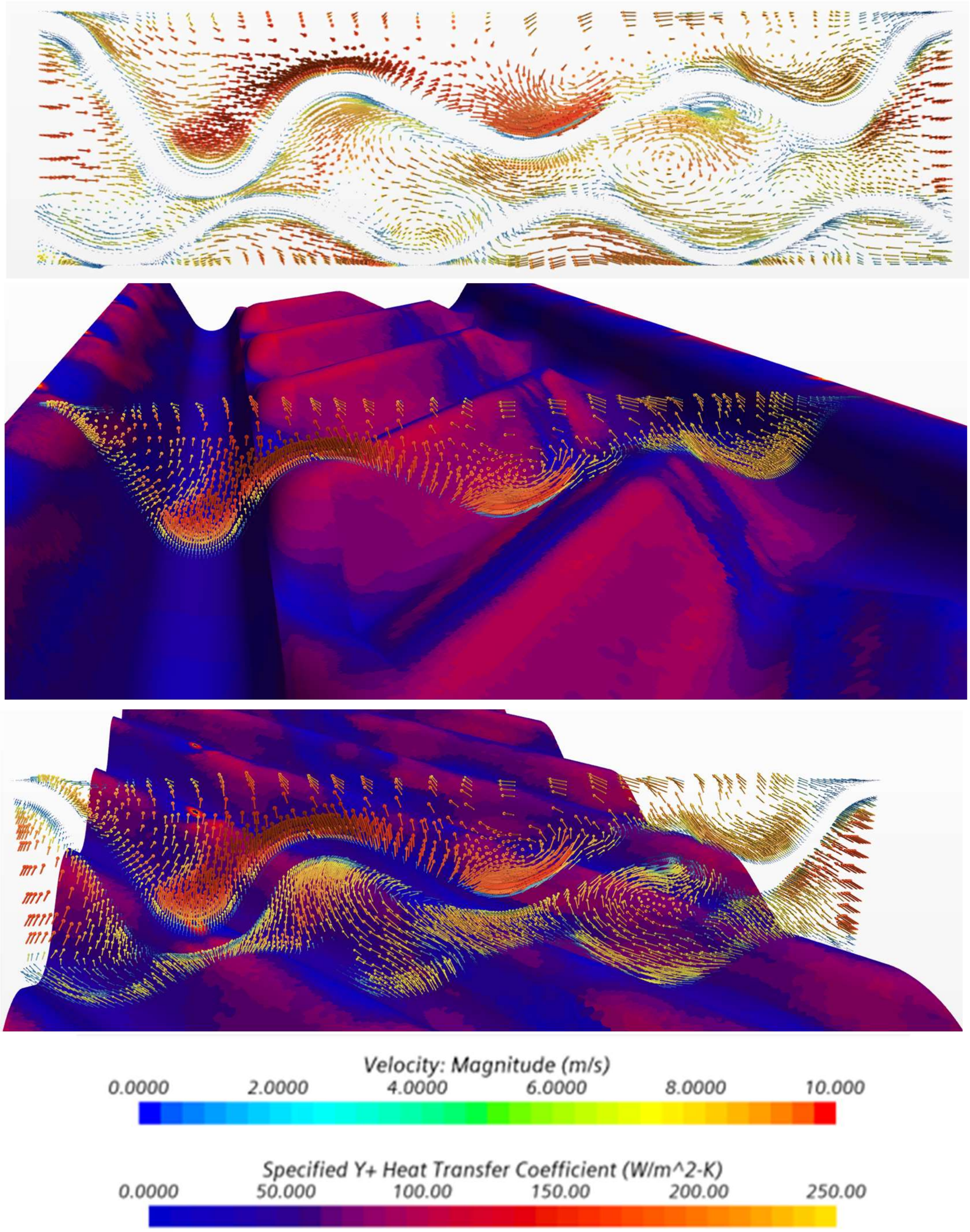

Figure 44. Velocity vector line visualisation in DU element model

This is further shown in Figure 44. It is possible to see vortex structures between the crossing undulated plates. In addition, there are clear swirling flow patterns between undulations over the top plate. There seems to be an interesting longitudinal strip of low heat transfer on both the top plate and bottom plate, which appears to be caused by vortex structures. The flow is pulled away from these areas by vortex structures nearby, resulting in lower heat transfer areas.

4.5 Herringbone corrugated profile

The friction factor results from the HC profile testing are shown in Figure 45, (a) shows the experimental results and (b) shows the simulated results, with experimental line of best fit and error limit lines. There were only three experimental data sets to compare from, and the results were quite varied. However, it is clear that the simulated data, falls inline with the data from 2015 and 2016, and is close to the average. The experimental data covers lower Reynolds numbers than previous experiments as the hydraulic diameter is significantly smaller than the previous element models tested. This inversely caused the Reynolds number to be higher in the CFD results, as the inlet mass flow remained the same, so the velocity

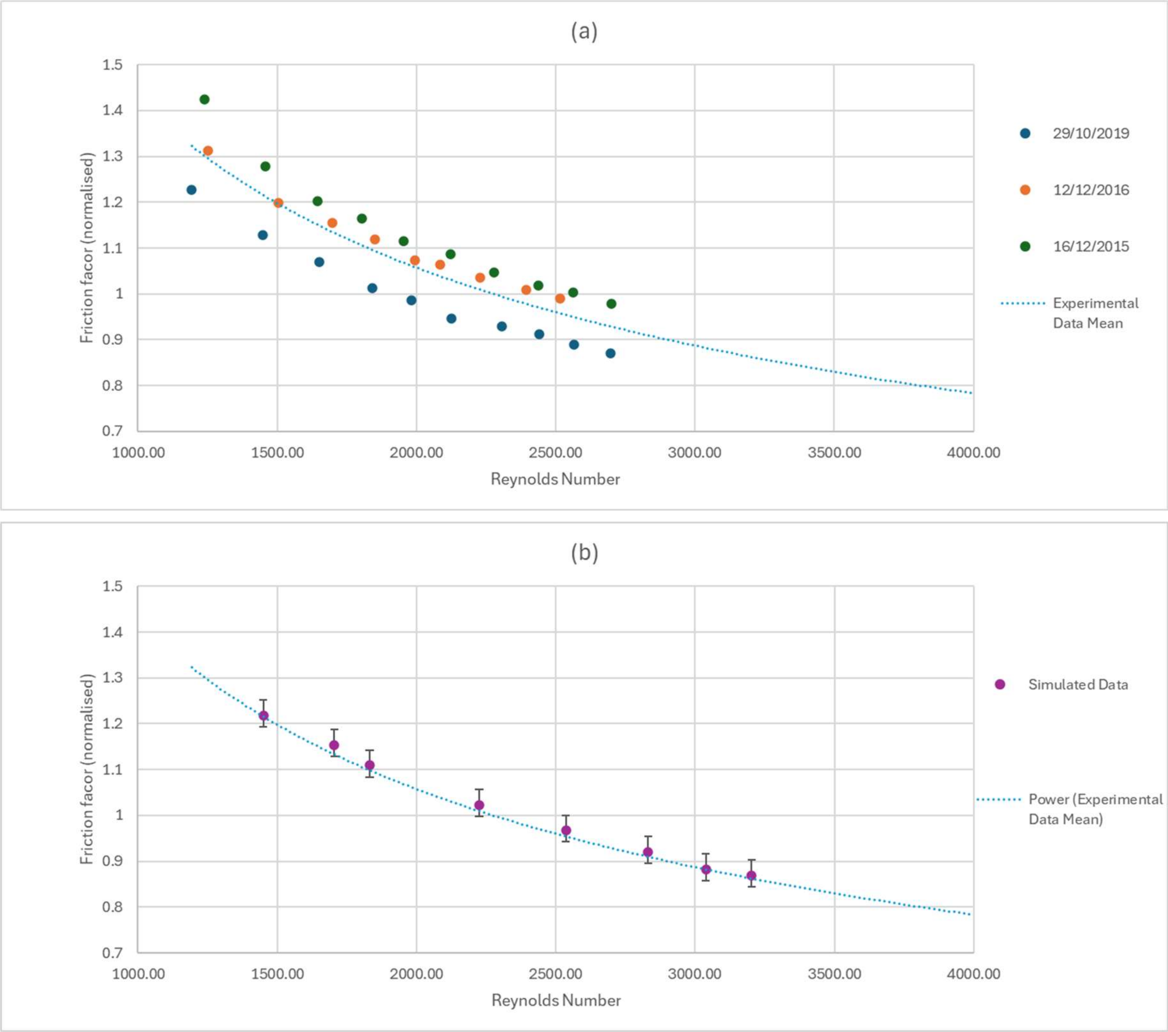

Figure 45. Friction factor through herringbone corrugated element profile, (a) experimental data, (b) CFD data

through the smaller flow channel was higher. Nonetheless, the simulated data matches the experimental data trendline well.

The Colburn factor results from the HC profile testing are shown in Figure 46, (a) shows the experimental results and (b) shows the simulated results, with experimental line of best fit and modelling error bars. The Colburn factor experimental results seem to have an even larger spread than the friction factor, although it is unclear if this is due to the smaller pool of data or if the element profile is more sensitive to atmospheric conditions. Regardless, the CFD data matched the average data well.

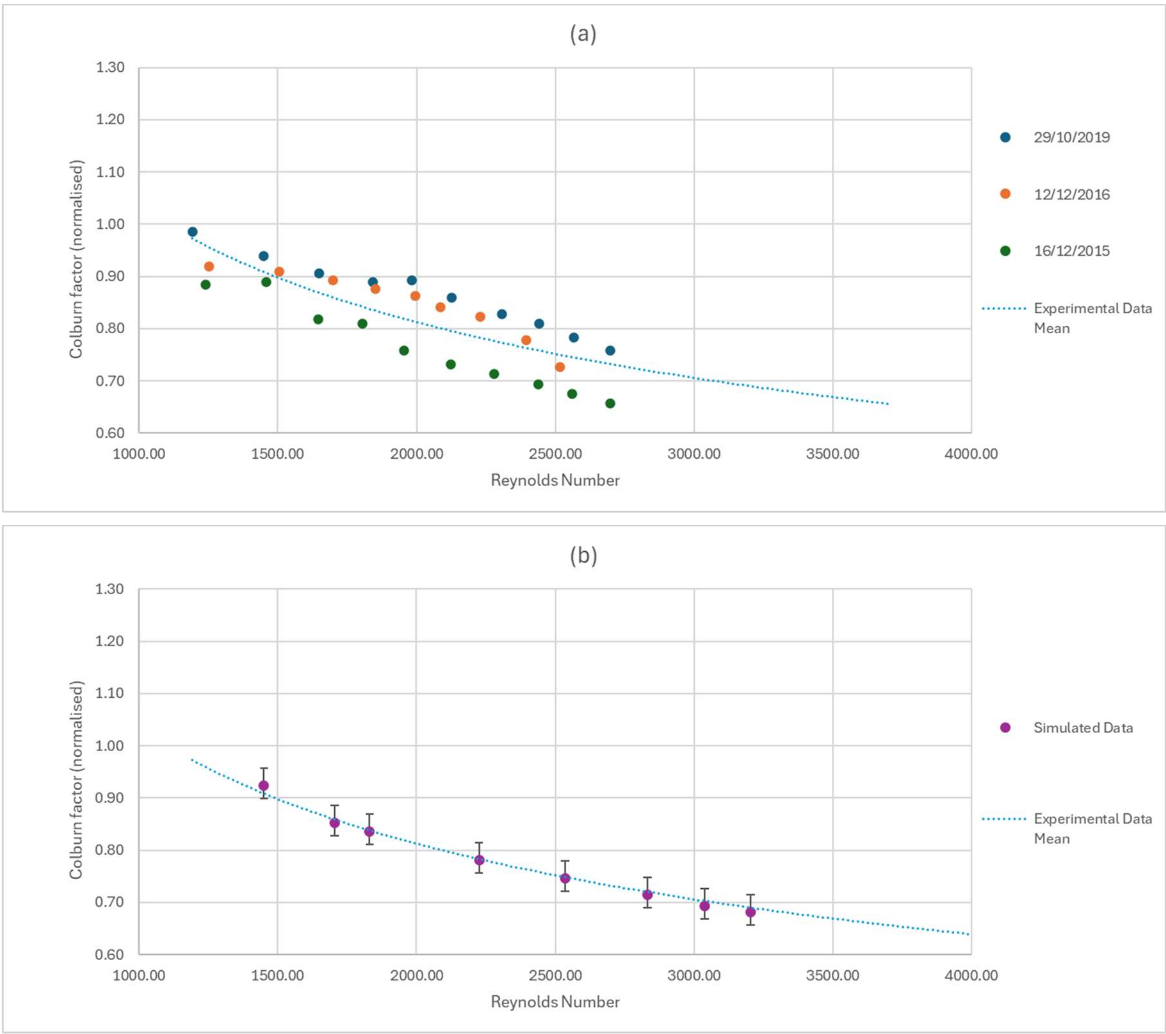

Figure 46. Colburn factor on Herringbone corrugated plate (a) experimental results (b) CFD results

The heat transfer performance of the HC7a has been analysed and visualised in Figure 47 and Figure 49, representing the herringbone and straight corrugated plate, respectively. The peaks of the angled corrugations exhibit the highest heat transfer, whereas the heat transfer is reduced around the areas aligned with the troughs of the straight-corrugated plate above.

There is a high heat transfer area where the where the plate comes into contact with the straight-corrugated plate above, with noticeable flow disturbances around that area as the flow is squeezed and redirected by the contact patch. It is hypothesised that in the current scenario, the proximity between the plates creates a short, closed channel aligning the flow with the direction of the inlet flow, maintaining parallelism to the plate's edge. This ensures that the flow continues over the peaks, resulting in an increased heat transfer in those areas, rather than flowing at an angle along the herringbone corrugations. The reduced heat transfer in the channels between the peaks being in line with the troughs of the straight-corrugated plate supports this hypothesis, as the proximity areas appear as a continuous line of reduced heat transfer. This is confirmed by the heat transfer performance at the chevron area where the opposed angled sections of the herringbone shape meet. A high heat transfer rate would be expected in this area, as the opposing angled flows meeting would induce a great deal of turbulent mixing. However, whilst the heat transfer rate is high in these areas, it is not as high as would be expected. This confirms that the straight corrugated plate is guiding a significant amount of the flow over the peaks, parallel to the edge of the plate.

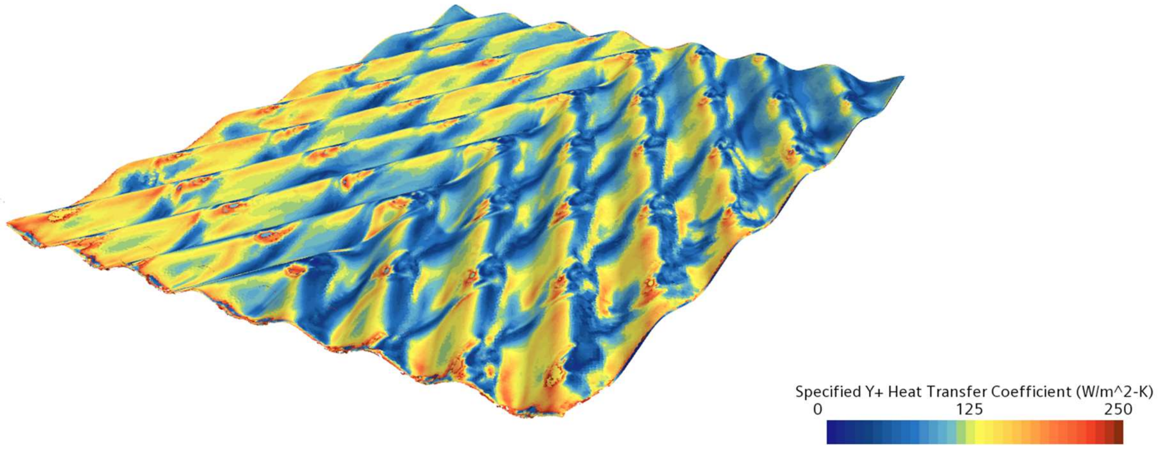

Figure 47. Heat transfer coefficient of herringbone HC7a plate

It is also noted that areas of high heat transfer are present at the edges of the plate, where the periodic boundary simulates a chevron in the opposite direction. This is visualised in Figure 48. It becomes clear that the heat transfer at the inlet is far greater than that at the outlet for the “down” facing chevron, whilst the opposite is true for the “up” facing chevron. This is believed to be a product of the flow regime through the plate, as the “down” facing chevron tends to direct flow away from the area, and the “up” facing chevron tends to attract flow to the area. This results in an extended interaction between the flow and the solid surface, increasing the heat transfer.

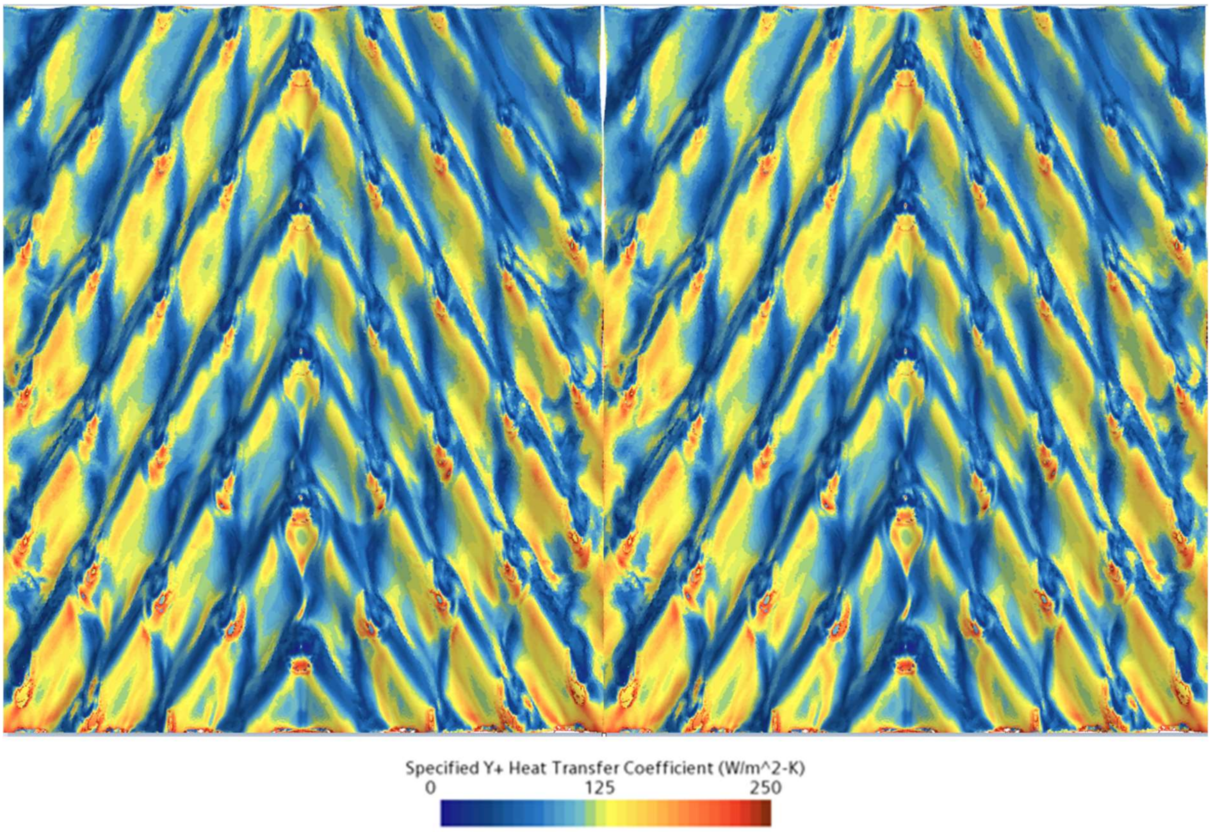

Figure 48. Double width visualisation of heat transfer over herringbone HC7a plate

Over the straight-corrugated plate, shown in Figure 49, there is an increase in heat transfer slightly upstream of each contact point. These areas are smaller in size and have a decreased heat transfer coefficient when compared to the high heat transfer areas in Figure 47. There is also a visible wake downstream of each contact point, displaying as a reduced heat transfer area. Whilst the straight corrugated plate generally shows much lower heat transfer performance than the herringbone plate, its value is shown in other ways. As previously stated, the straight corrugations help to direct flow over the herringbone plate, but it also allows a relatively free flowing area to reduce the overall pressure drop through the element pack.

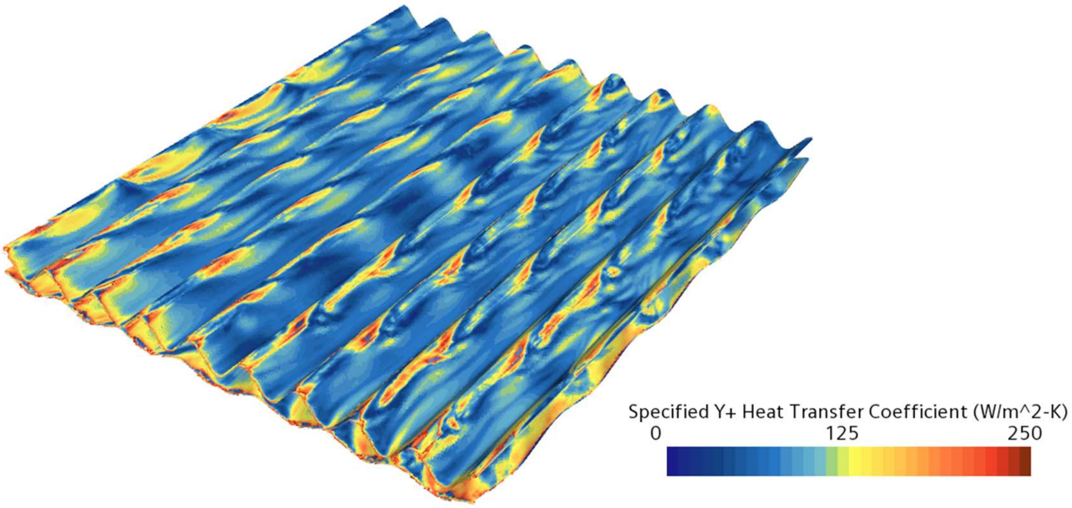

Figure 49. Heat transfer over straight-corrugated HC7a plate

Figure 50 shows the pressure at the midplane of the part. A clear pressure gradient towards the middle of the part can be seen, showing that the flow is generally directed towards the chevron areas. However, small pockets of interesting pressure gradients can be seen in the troughs of the straight corrugated plate, showing the re-direction effect.

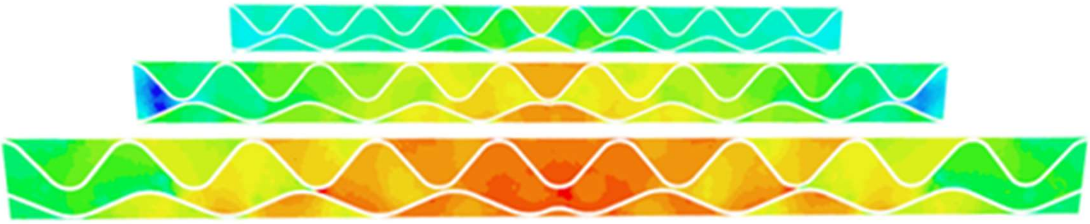

Figure 50. Pressure gradient through HC7a part

Figure 51 features velocity streamlines over the HC element profile, with the surface coloured to show the heat transfer coefficient. It is clear that the corrugated plates help maintain straight flow through the passage, reducing the skew flow towards the point of the chevron, although a large portion of the flow is attracted towards the centre. Swirl flows can be seen as the fluid travels over the angled corrugations, and the high heat transfer in these areas is representative of the positive turbulence regime created.

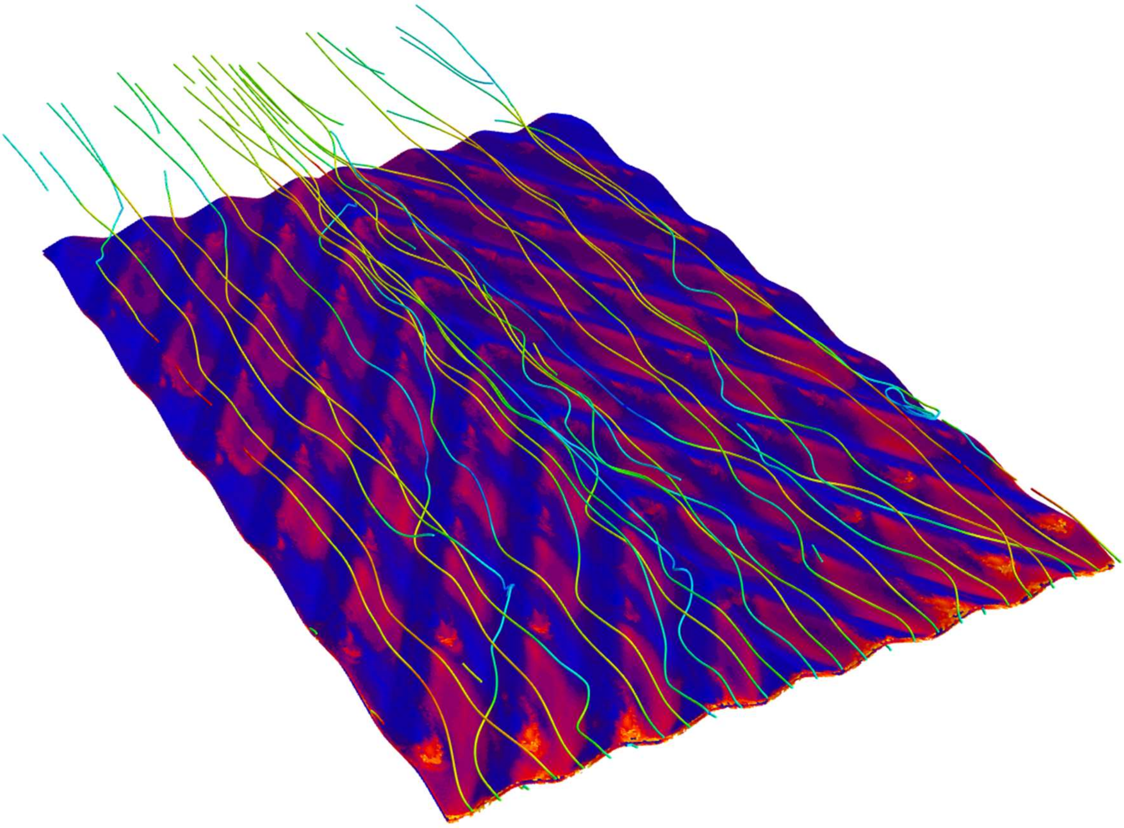

Figure 51. Velocity streamlines through over HC element profile

4.6 Simulated Model Validation Summary

Three completely different element profiles have been modelled with a CFD simulation and compared to experimental data. The comparisons show that the CFD model is accurate, and the variety of element profiles tested ensure its robustness across a wide range of problems. The simulated model is now considered a valid "virtual test rig" and the future experimentation results can be trusted to be accurate in reality.

5. FNoC Geometric Optimisation Scheme

5.1 Introduction

Howden have refined the FNoC style plate model over time, with the latest iteration being the HS20. The refinement process relies on a "trial and error" approach, with each iteration of the design having to be manufactured and tested in the experimental test rig. This process can be expensive and time consuming, with each new design requiring new rollers to manufacture. Due to the nature of the manufacturing process, the number of configurations was limited, resulting in a lack of understanding of the performance over the range of dimensions. For example, the notch pitch values tested were 30 mm, 35 mm, and 40 mm, with 35 mm performing 11% better than the lowest performing configuration. However, the optimal value may be 33 mm or 37 mm, which wouldn't be found in testing. To fully understand the performance of this model, more experiments must be undertaken. The cost and time consumption of the additional experiment runs can be minimised through the use of CFD.

This chapter will focus on the optimisation of the FNC model through modifying the dimensions of notch pitch and radius.

5.2 Methodology and Optimisation strategy

The CFD simulation was set up identically to the previous simulations used in the model validation, to ensure that the results are accurate.

The optimisation strategy involves varying the pitch (normal peak-to-peak distance between notches), and radius of the notches on the Flat Notched Crossed (FNoC) platform, shown in Figure 52. The performance measures include pressure drop, measured by friction factor, and heat transfer, measured by Colburn factor.

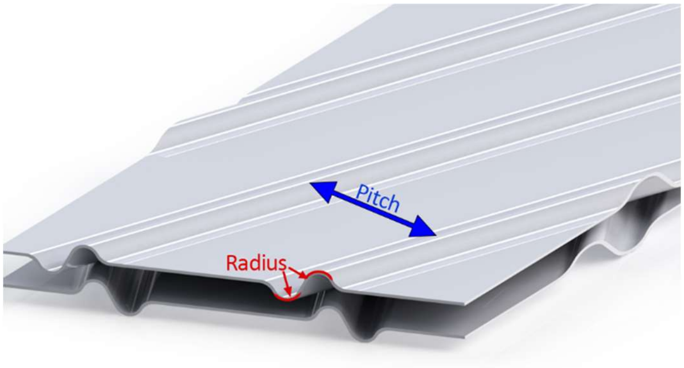

Figure 52. Pitch and radius dimensions of FNC

This paper uses Latin Hypercube sampling (LHS). It is a quasi-random technique which aims for a good distribution of values across the range of each of the factors. This ensures each variable is properly explored and defined, leading to a better understanding of the optimisation problem. This technique is particularly useful for variables with a wider range, such as the current study, where the distance between notches could be varied from 30 mm to 40 mm, for example, (100). A set of 10 configurations were required for two variables and two outputs. Pitch was varied from 30 mm to 40 mm, and radius of notches from 2 mm to 4 mm. The configurations are shown in Table 6, and displayed visually in Figure 53.

Table 6. Tabulated Latin hypercube configurations for FnoC geometric optimisation

Configuration	Pitch	Radius
LH1	32.25	2.63
LH2	31.74	3.75
LH3	38.49	3.44
LH4	39.30	2.35
LH5	30.11	2.01
LH6	34.04	3.13
LH7	33.45	3.96
LH8	35.86	2.95
LH9	36.85	3.28
LH10	37.74	2.51

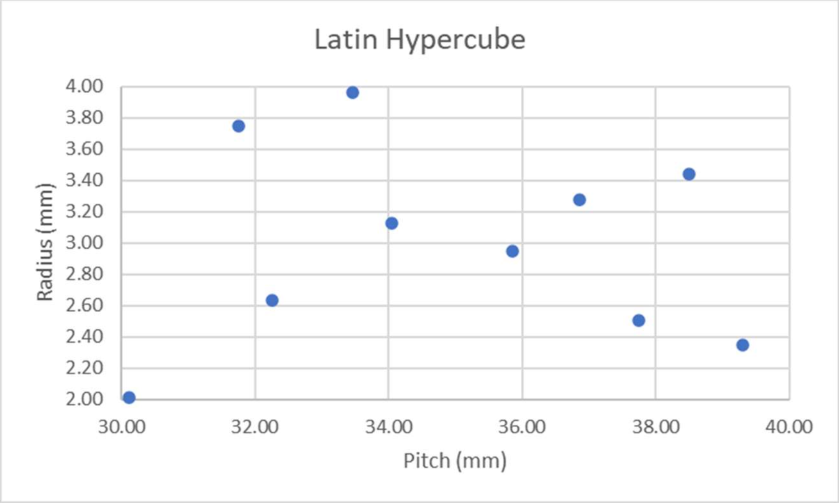

Figure 53. Graphed Latin Hypercube configurations for FNoC geometric optimisation

A kriging script was created in MATLAB utilising the ooDACE MATLAB kriging tool suite. The script takes the raw data from the simulations, runs it through the ooDACE tool, and plots the kriging function for each output over the range of the two variables. This method gives two plots, showing how both variables affect each performance measure.

In this study, a kriging script was developed using the ooDACE MATLAB kriging tool suite to analyse raw data obtained from simulations. The script was designed to process the data through the ooDACE tool and generate a kriging function relating the outputs to the variables. The data is shown in two 3D plots, showing each performance measure output against the two input variables. This is visualised as a surface, facilitating straightforward visual analysis.

An objective function was implemented to minimise the friction factor and maximise the Colburn factor. The scalarisation method was utilised to combine the objectives into a single function with weighting factors established to balance the objectives and assign priority. This method involves normalising each objective to a reference value, which is typically taken as the mean value of the objective across the design range. This is a relatively simple approach which provides a balanced and interpretable means of comparing designs across the design range (153).

The general form of the objective function is shown in Equation 5.2.1. This function is minimised to find the optimal result. Colburn factor is set as negative to maximise it.

$$Objective = w_f \cdot \left(\frac{f}{f_{ref}}\right) - w_J \cdot \left(\frac{J}{J_{ref}}\right) \tag{5.2.1}$$

Where w denotes the weighting factor, f is the friction factor and J is the Colburn factor.

To account for the relative importance of the two objectives, unequal weights were applied during scalarisation. The Colburn factor was assigned a higher weighting (0.7) than the friction factor (0.3), reflecting its greater impact on overall system efficiency and cost. While reductions in friction factor are beneficial, they tend to be more readily achieved and less influential on design outcomes. However, some weight must be assigned to friction factor to ensure that high friction factor configurations are not selected. In contrast, increases in the Colburn factor directly improve heat transfer performance and allow for a reduction in the depth of the RRHE, which can in turn lower total pressure losses. By favouring the Colburn factor in the objective function, the optimisation process was guided towards solutions that offer meaningful thermal performance gains without entirely disregarding pressure drop improvements.

Therefore, the objective function is displayed in Equation 5.2.2.

$$Objective = 0.3 \cdot \left(\frac{f}{f_{ref}}\right) - 0.7 \cdot \left(\frac{J}{J_{ref}}\right) \tag{5.2.2}$$

5.3 FNoC geometric optimisation results

The results from the optimisation code are presented in Figure 54 as 3D plots, with the variables on the horizontal X and Y axes and the results on the vertical Z axis. There are some clear areas of interest upon visual inspection: the valley around pitch = 37 mm in the friction factor plot, with a corresponding high area in the Colburn factor plot, and the trough in the pitch = 30 mm / radius = 4mm corner in the friction factor plot, with the corresponding peak in the Colburn factor plot. The low friction factor and high Colburn factor areas are undoubtedly the best performing areas.

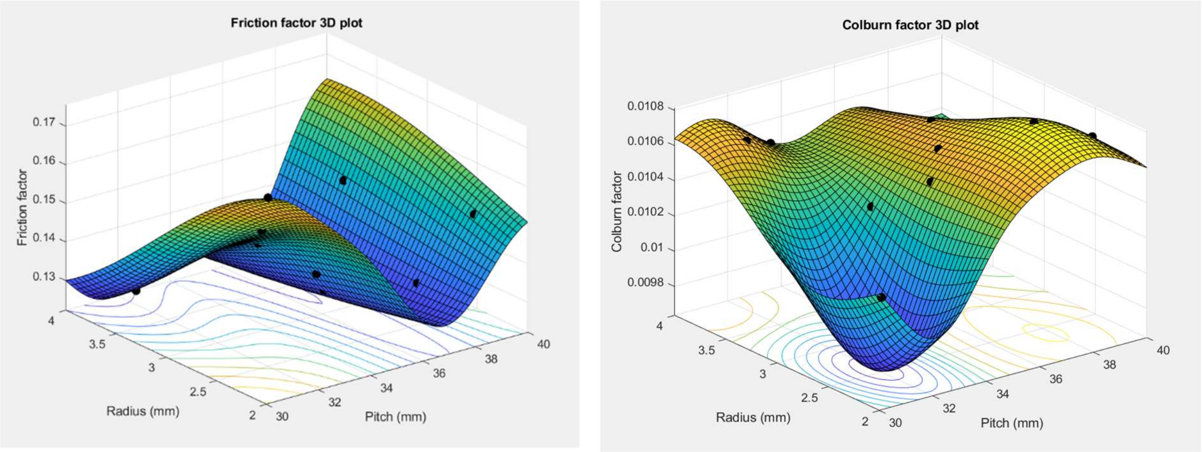

Figure 54. 3D kriging surface plot of friction factor (left) and Colburn factor (right).

Using the MATLAB pareto-search function, the optimal points in these areas were found (Table 7). As predicted, the best performing points are located within the pitch = 37 mm valley and the pitch = 30 mm / radius = 4 mm corner. “Optimal Result 1” has a reasonable improvement in both the friction factor and Colburn factor, and “Optimal Result 2” has a much higher improvement in friction factor with a lesser improvement in Colburn factor. “Optimal Result 1” is the appropriate choice for this study.

Table 7. FNoC geometric optimisation results

	Pitch (mm)	Radius (mm)	FF % difference	CF % difference
Original FNC			0.0	0.0
Best FF	31.6	4	-10.7	+1.6
Best CF	37.9	2.43	-1.9	+2.9
Optimal result 1	36.9	2.67	-7.3	+2.3

A model was created from the dimension listed in “Optimal Result 1” and a CFD simulation was run on it. The results are shown in Table 3. Note that the percentage difference term is taken as a difference in calculated friction factor and Colburn factor values, not the percentage improvement values. The friction factor result is 1% higher than the predicted result. This particular difference can be attributed to the sensitivity of the friction factor to minute differences in the design. This is believed to be due to rounding in the pitch and radius variables. This issue is unavoidable, as the tolerances for manufacture for the element plates will not realistically achieve accuracy for measurements smaller than 0.3mm.

Table 8. Predicted vs simulated results

	FF % difference	CF % difference
Predicted	-7.30	2.28
Simulated	-6.34	2.35
% Difference	1.04	0.09

The local heat transfer coefficient across the surface of the Flat Notched Crossed plate is shown in Figure 56, along with the velocity profile in the flow direction at 3 planes across the plate. The optimised plate design is shown for comparison, and the areas where heat transfer is augmented are clear.

The lighter coloured areas on the flat area of the plate correspond to higher local heat transfer rates from vortices created by the crossflow of the opposing notch angles of the two plates. This appears to show that the pitch and radius dimensions play a large part in allowing these vortices to fully develop, improving the overall turbulent mixing through the heat exchanger. These vortex structures can be clearly seen on the velocity flow planes, with circular low velocity areas surrounded by a ring of higher velocity, indicating the swirling flow of a vortex structure. It is also apparent that some parts of the element have significantly less “contact” with the flow, showing there is still room for further heat transfer augmentation.

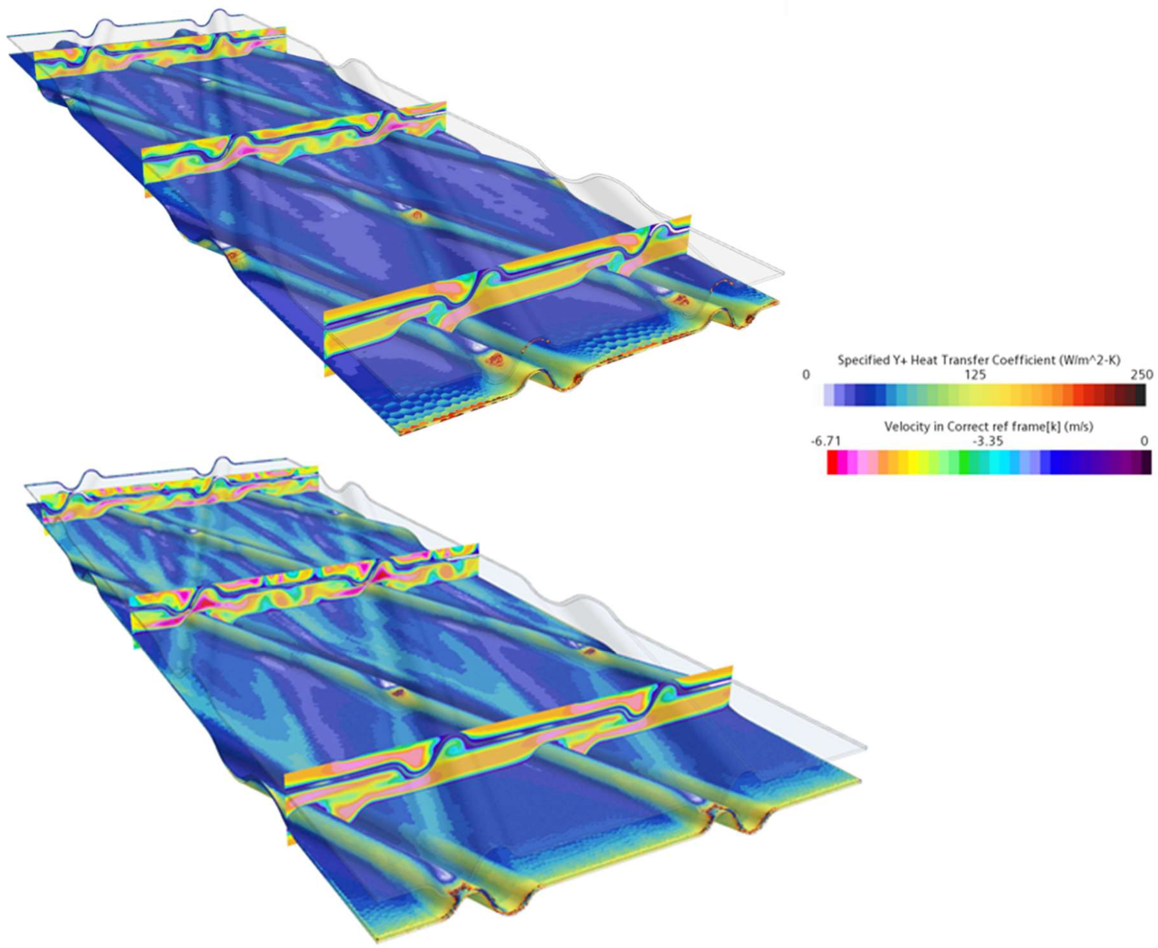

Figure 56. Local heat transfer and velocity flow planes over bottom Flat Notched Crossed plate

The stronger vortices can be seen clearly when comparing the velocity flow planes side by side (Figure 55). In the “middle” plane there are 2 clear vortices in the flat areas in between the two plates, with several other less obvious vortices in other areas. The vortices are remarkably stronger and more visually obvious in the optimised model. This leads to the conclusion that the strength and control of these flow structures is key to the increased performance of the plate design.

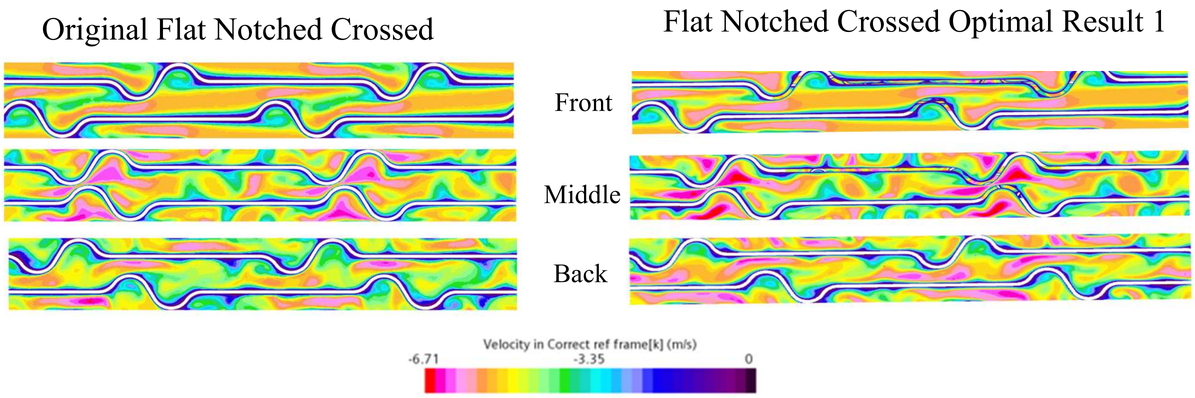

Figure 55. Velocity flow plane view in Flat Notched Crossed plate

From the pressure plane comparisons (Figure 57), the same effect can be seen, with low pressure areas outlining vortex flow systems, clearest in the “middle” planes. The two models have a similar vortex structure in the flat area between the notches, but the optimal configuration features a lower pressure in the core, which is likely due to a stronger vortex.

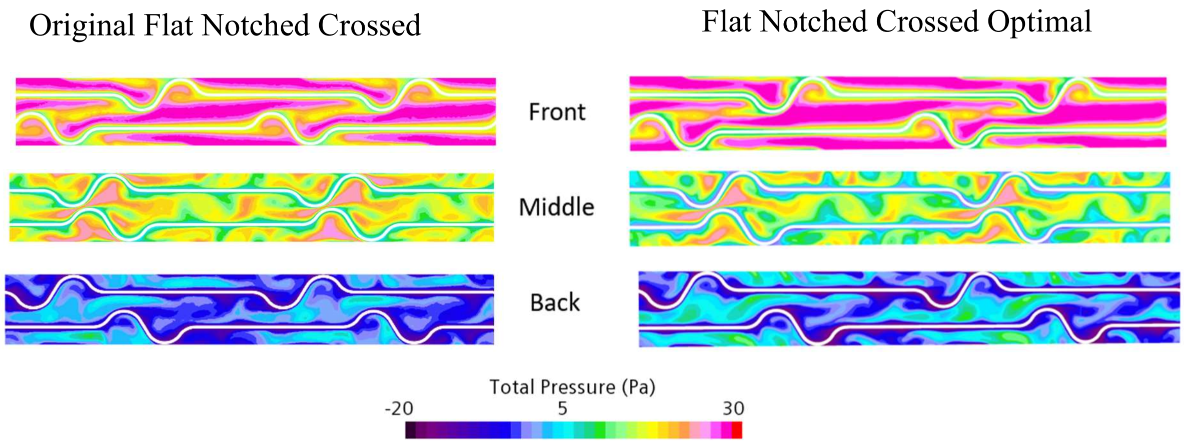

Figure 57. Pressure plane view in Flat Notched Crossed plate

The best configurations were created and modelled. CFD simulations were run to analyse the performance of the configurations across the full Reynolds number testing range. The results are shown in Figure 58. This data serves to prove the accuracy of the Kriging approximation used in the optimisation scheme.

It is clear to see that each of the configurations perform significantly better than the original FNoC across the entire Reynolds number range. Interestingly, the performance curves follow a similar shape to that of the original model, showing a predictable yet improved performance within the range of Reynolds number testing.

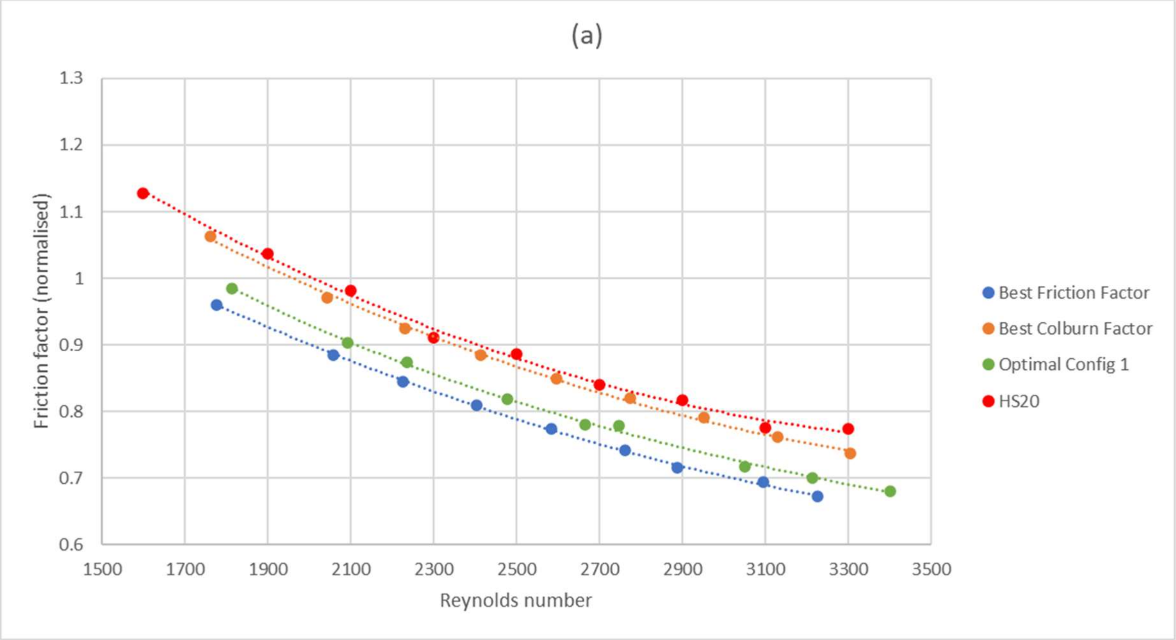

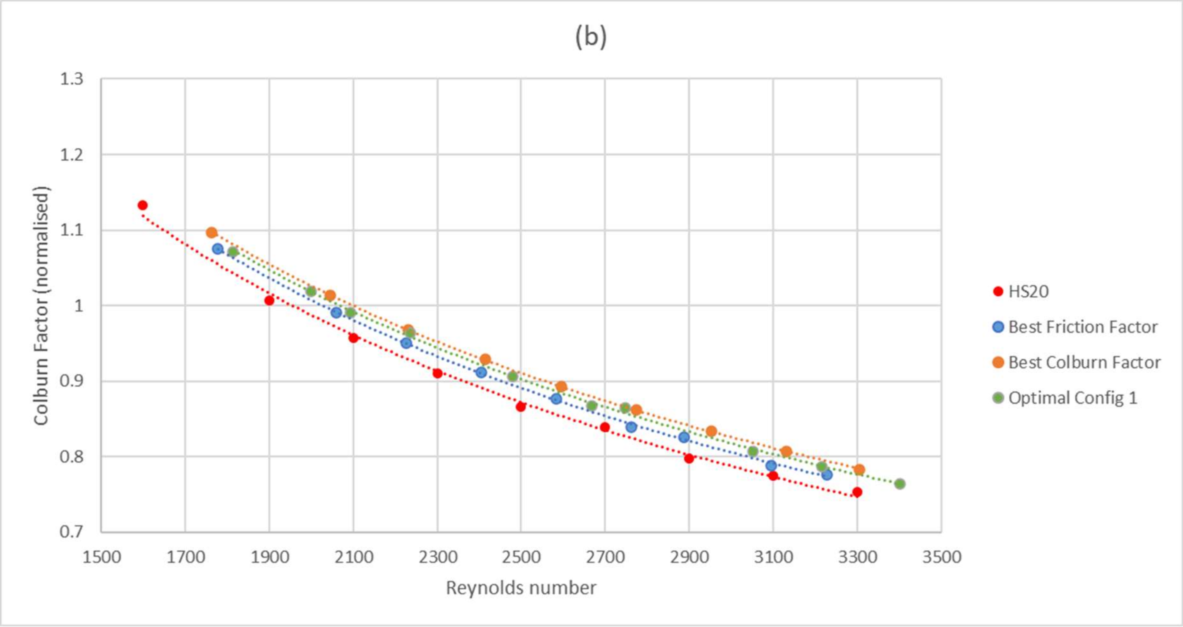

Figure 58. Friction factor (a) and Colburn factor (b) of optimal FNoC configurations compared

5.4 Tolerance Sensitivity Analysis

To properly analyse the performance across the tolerance range, a tolerance sensitivity analysis was conducted. Optimisation methods were employed in order to efficiently measure the impact of deviations from the dimensions within the accepted manufacturing tolerances.

5.4.1 Methodology

The existing manufacturing tolerances are shown in Table 9. Pitch is defined as the centre-to-centre distance between notches, radius of notch describes the outer radius of the notch, and packed pair height is the full height of a pair of FNoC plates.

Table 9. Manufacturing tolerances on FNC plate

Dimension	**Tolerance**
Pitch	±1mm
Radius of notch	±0.5mm
Packed pair height	±0.3mm

The sensitivity analysis is set up with the purpose of measuring the friction factor and Colburn factor at the extreme ends of the tolerance range, with a view to predicting a “worst-case” scenario. The change in performance across the range of tolerance boundaries was analysed to determine the feasibility of manufacturing with the current tolerances and establish design tolerances for the optimised FNoC profile if required.

The Box Behnken design of experiments method was deemed a good fit for the study. This method allows for 3 dimensions with 3 levels each. The experiments are set up such that the levels constitute maximum lower tolerance, design value, and maximum upper tolerance in each dimension, represented by -1, 0 and 1. The design points are shown in Table 10.

Table 10. List of experiments for sensitivity analysis

Designation	Pair height	Radius	Pitch
BB1	-1	-1	0
BB2	-1	1	0
BB3	1	-1	0
BB4	1	1	0
BB5	-1	0	-1
BB6	-1	0	1
BB7	1	0	-1
BB8	1	0	1
BB9	0	-1	-1
BB10	0	-1	1
BB11	0	1	-1
BB12	0	1	1

A Kriging algorithm was created to predict the performance across the tolerance range. The code was again set up with the ooDACE software, and 3D surface graphics were generated to visualise the performance across the tolerance range.

A multi-objective search function was set to maximise friction factor and minimise Colburn factor in order to find the largest decrease in overall performance. Additionally, single objective optimisation search functions were employed to find the largest performance drop in Colburn factor and friction factor separately.

The weights of the function are equivalent to the weights used in the previous optimisation work to maintain consistency in evaluating the robustness of the design. This ensures that the sensitivity assessment is aligned with the priorities of the performance optimisation, and therefore the worst-case deviations are relevant to the desired performance goals. The objective function for the sensitivity analysis is shown in Equation 5.4.1. For the sensitivity analysis, this function is maximised.

$$Objective = 0.3 \cdot \left(\frac{f}{f_{ref}}\right) - 0.7 \cdot \left(\frac{J}{J_{ref}}\right) \tag{5.4.1}$$

5.4.2 Results

The performance graphs are shown in Figure 59. It is clear that there is a general decrease in performance toward the tolerance boundaries, away from the design values. However, there are also areas where the performance increases slightly. The optimisation search functions returned a variety of interesting results, which are tabulated in Table 11. Positively, each “worst-case” scenario remained an improvement over the original HS20 FNoC design in both friction factor and Colburn factor. Further, due to the often-opposing nature of the two performance measures, in the individual worst cases, the other quantity seemed to slightly increase in performance. The largest drop in Colburn factor performance from design specification was 1.18%, whilst the largest drop in friction factor performance was 6.73%.

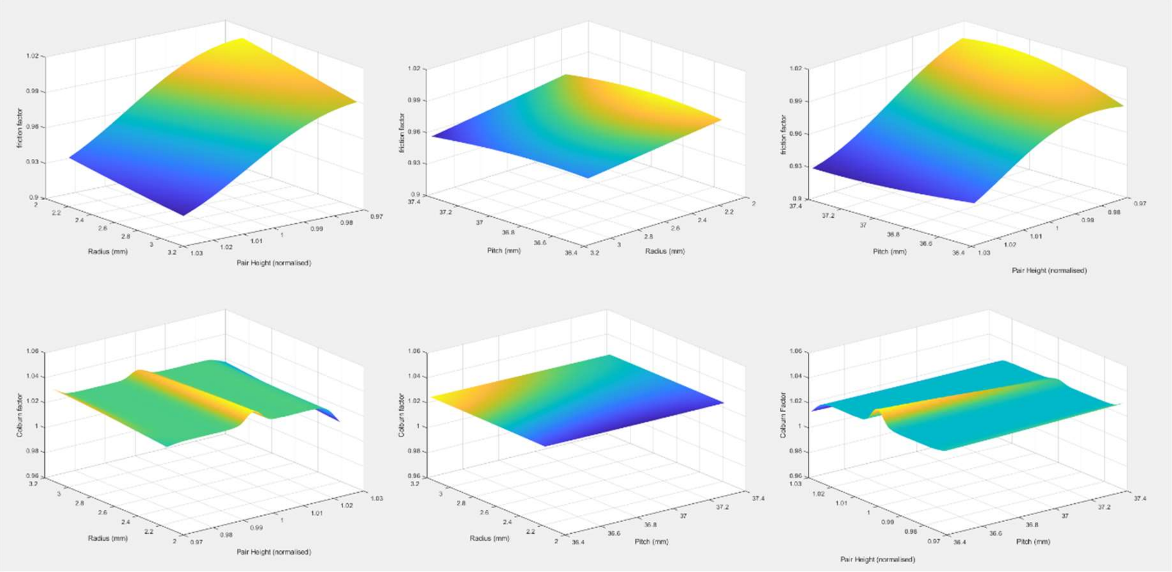

Figure 59. Tolerance sensitivity analysis graphical results

From the graphs (Figure 59), it appears that the packed pair height was the most significant dimension in altering performance, and in each of the cases presented, the worst-case result value was found at either the minimum or maximum point of the tolerance range. The friction factor in particular was greatly affected, as the lower bound of the dimension reduced the size of the closed channels. This altered the overall porosity of the element pack, effectively restricting the flow. However, the reduction in channel size caused an increase in velocity, leading to an increase in the turbulent mixing and energy transfer. This promotes a greater Similarly, at the upper tolerance bound, the friction factor is reduced, as the larger channels allowed the fluid to flow more freely, causing a reduced flow velocity through the channel. This led to a reduction in turbulent mixing and energy transfer, resulting in a reduced heat transfer coefficient across the plate. Overall, the design value for pack pair height seems to be the optimal value.

Based on this data, the tolerances in the packed pair height dimension should be evaluated and tightened. However, the dimensions which were optimised previously, the radius and pitch have acceptable tolerances, and even in the worst-case scenario, an improvement can be found over the original FNoC design.

Table 11. Results of the tolerance sensitivity analysis

Sensitivity Analysis Results							
	Dimensions			Original FNoC Comparison		Optimised FNoC Comparison	
	Pair height	**Radius**	**Pitch**	**ff % diff**	**cf % diff**	**ff % diff**	**cf % diff**
Original FNoC				0.00%	0.00%	100.00%	-100.00%
Optimal Result 1	0	0	0	7.30%	2.33%	0.00%	0.00%
CF Worst Case	1	-1	0	8.67%	1.12%	1.48%	-1.18%
FF Worst Case	-1	-1	0	1.06%	2.76%	-6.73%	0.42%
Combined Worst Case 1	-1	-1	-1	3.49%	2.56%	-4.11%	0.22%
Combined Worst Case 2	1	-1	-1	8.16%	1.26%	0.93%	-1.05%

5.5 FNoC geometric optimisation summary

The FNoC element profile has been successfully optimised using a Latin hypercube design of experiments and kriging surrogate model, with a satisfactory performance improvement in both the heat transfer and pressure drop characteristics. The flow through the optimal part was analysed, and the key difference identified was an improvement in the control and definition of longitudinal vortex structures.

A sensitivity analysis was undertaken to ensure reliable performance within current established manufacturing tolerances. The methodology included a Box-Behnken design of experiments and Kriging surrogate model, which predicted that the two worst case scenarios would still be an improvement over the original FNoC design. The results showed that the performance depended most on the packed pair height dimension.

6. Heat Transfer Enhancement – Delta Winglets

Existing research shows that the addition of vortex generating devices can greatly alter the performance characteristics of a heat exchanger. This effect is achieved by altering the geometry of the heat transfer surface, or through the addition of a vortex generator. The purpose of these alterations is to create vortex structures, control existing vortex structures, or promote an early transition to turbulent flow. This in turn can increase turbulent mixing and direct flow to desired areas to increase heat transfer.

In this section, delta winglets are added to the optimised FNoC model. The original intention of the delta winglet design is threefold: inspire an earlier transition to turbulence, create longitudinal vortex structures to control and direct flow, and guide flow towards the high heat transfer notch areas to increase the efficiency of the existing model design.

6.1 Methodology

An optimisation scheme was fulfilled on the addition of delta winglets to the “Optimal Result 1” optimised FNoC model. A single row of delta winglets was placed along the flat section of the plate near the inlet. Four winglets were equally spaced between the notches, representing the maximum number that could be accommodated within the available space at the upper bounds of the optimisation variables. This configuration was chosen to maximise the aerodynamic disturbance and thus highlight the potential impact of winglets on thermal performance. However, it is acknowledged that in practical applications, maximising the number of winglets may not be ideal due to the increased manufacturing complexity and cost associated with intricate geometries.

The variables were chosen as the length of the winglet, angle of the winglet with respect to the flow (or angle of attack), and distance from the leading edge of the plate.

The variables are shown in Figure 60, with ranges set as:

- length = 2 mm – 10 mm
- angle = 20° - 40°
- distance from front = 0 mm – 20 mm.

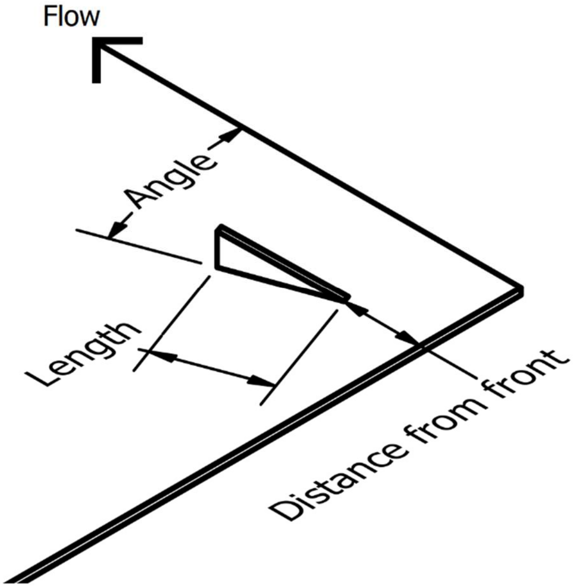

Figure 60. Winglet dimensions

To ensure the perturbations in flow around the winglets were captured, the mesh was locally refined in the vicinity of the winglet surfaces. This involved reducing the base cell size near the winglet surfaces. Particular attention was paid to the Y+ value, ensuring a value of around 1 was achieved. Additionally, the growth rate of the fluid cells downstream of the winglets was lowered to ensure high resolution in the wake of the winglets.

A similar optimisation script to the FNoC shape optimisation was set up, with the design of experiments utilising Latin Hypercube methodology, and a Kriging algorithm was set up with the ooDACE software to predict the performance over the variable range. The scalarisation method employed in the previous section is utilised again for this methodology. In this case, the weights were modified to 0.8 for the Colburn factor and 0.2 for the friction factor, as the objective function tended to favour solutions with lower friction factor and minimal change in Colburn factor. This appears to be a result of the highly localised nature of the friction factor results, which may cause the normalising nature of the objective function to over represent the friction factor performance.

$$Obj = 0.2 \cdot \left(\frac{f}{f_{ref}}\right) - 0.8 \cdot \left(\frac{J}{J_{ref}}\right) \tag{6.1.1}$$

6.2 Results

The graphical results are displayed in Figure 61. Note that in optimisation schemes with three dimensions, in order to display a surface graph, 2 dimensions are shown, and one dimension is set at a constant value. This can be thought of as showing a slice of the 3-dimension surface. In this case, the dimension was set at the optimal value for each of the graphs.

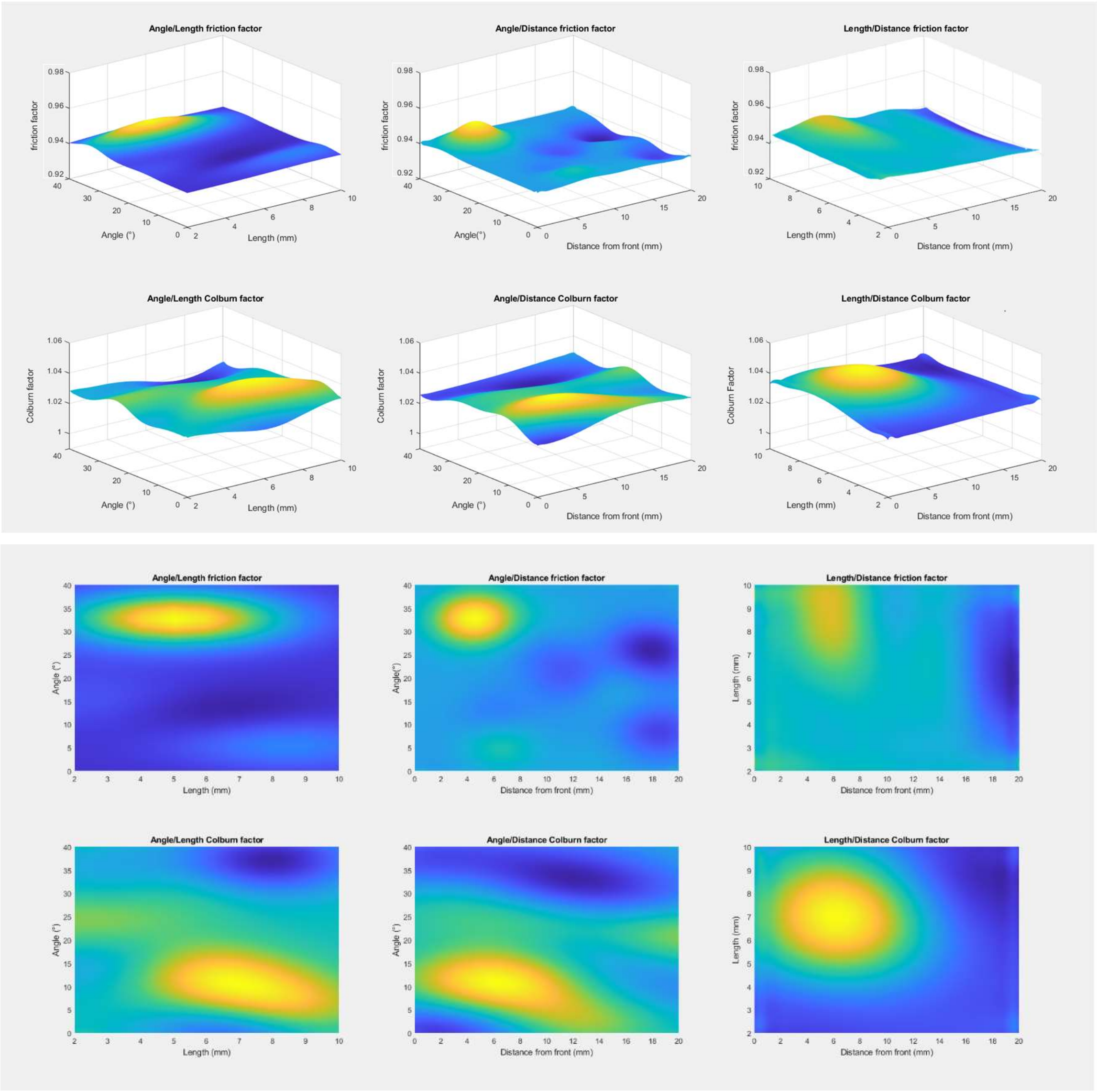

Figure 61. Graphical results of delta winglet optimisation scheme with friction factor and Colburn factor normalised to the mesh sensitivity simulated value

6.2.1 Winglet Angle/Length relationship

The relationship between the length and the angle is shown in the Angle/Length graphs in Figure 61. There is a high heat transfer ridge across the length spectrum, spanning angles of 20-25° at lower length and moving to angles of 10-15° at higher length. This shows that at shorter lengths, steeper angles are required to effectively direct the flow towards the notch area. As the length increases, the larger winglet can do more work on the flow, so the larger angle is not required. Further, a steeper angle with the larger winglet begins to become disruptive, preventing the flow from developing and redirecting smoothly. The heat transfer performance peaks at angles of around 8-12° and lengths of 6-8mm.

This configuration appears to effectively direct the flow towards the notch without causing excessive pressure drop. The moderate angle facilitates higher winglet effectiveness, as increasing the angle results in a drop off in heat transfer performance. The higher angled winglets cause excessive flow disruption, acting more like a barrier than a winglet. The increased turbulence as a result in turn creates higher aerodynamic drag and stronger wake regions downstream of the winglets, reducing heat transfer throughout that area.

In the friction factor graph, there is an area of high pressure drop at angles of 30-40°, further showing the disruption and blocking effect created by higher winglet angles. There is also a lower pressure drop area corresponding to the high heat transfer region at angles 8-12° and lengths of 6-8mm, showing that the configuration in this area is highly effective in improving the overall performance of the model, through promotion of effective turbulence generation and flow control.

6.2.2 Winglet Angle/Distance relationship

The relationship between the winglet angle and the distance from the front edge of the element plate is shown in the Angle/Distance graphs in Figure 61.

The peak in pressure drop at higher angles of 30-40 degrees and closer distances of 3-8mm results from the combination of a sharp flow redirection at a short distance from the front edge, where the flow is already disrupted from impacting the front face of the plate, and has not had time to stabilise. The lower pressure drop regions at angles of 2-25° and distances of 15-18mm suggest that in this range of configurations, the winglet is offering minimal flow resistance. This could be due to the flow having more time to stabilise and develop naturally before reaching the winglets, and the shallower angle smoothly redirecting the flow and creating advantageous turbulence structures.

In the Colburn factor graph, a low heat transfer performance region is seen at high angles of 30-40°, across the full range of distance. A similar region was observed in the Angle/Length graph, meaning winglet angle values over 30° are not beneficial to the heat transfer performance. The steep angle creates an overly strong redirection, creating excessive turbulence, resulting in poor interaction between the flow and surface. High heat transfer performance is present at angles of 10-20° and distances of 3-11mm. The optimum angle range matches that of the winglet/angle relationship, showing that this range of values effectively and efficiently directs the flow towards the notch in a fashion that minimalises aerodynamic resistance, whilst generating appropriate turbulent flow features. The distance from the front of the plate peaks in performance around 6mm, showing that this distance is sufficient to allow the flow to stabilise after reaching the front edge of the plate, whilst short enough to maximise the effectiveness of the winglet.

6.2.3 Winglet Length/Distance relationship

The relationship between the winglet length and the distance from the front edge of the element plate is shown in the Length/Distance graphs in Figure 61.

On the pressure drop graph, a peak at shorter distances of 5-7mm can be seen, with pressure drop increasing with length from 5-9mm, peaking around 8.5mm. This shows at lower lengths, the winglets are positioned optimally, resulting in low pressure drop. As length increases, the increased winglet area results in a larger interaction with the flow, generating turbulence and redirecting the flow as required, with a slight increase in pressure drop. At high lengths, this effect leads to excessive turbulence and flow disruption, escalating the pressure drop further. There is a low pressure drop region at distances of 15-20mm across all winglet lengths. A corresponding low heat transfer zone shows that winglets placed at this distance lose effectiveness, likely due to the smooth and well-developed flow reacting minimally with the winglets. Additionally, the increased boundary layer thickness at this distance will result in a reduction in the redirection effect of the winglets on the main flow.

There is a broad peak in heat transfer at distances of 3-10mm and lengths of 5-8.5mm, with maximum performance around 7mm in length and 6mm distance from front. These values match the optimum values observed in previous comparisons, strengthening this choice of values as an optimum configuration of the delta winglet.

In summation, winglet angles of 10-20° redirect the flow and boost heat transfer efficiently, keeping pressure drop low, lengths of around 6-8mm disrupt the boundary layer effectively and are large enough to achieve the flow redirection effect without causing excessive restrictions and blockages, and winglets placed 2-10mm from the front are situated in the ideal location for maximum effect.

6.2.4 Optimal Results

The results from the objective function are presented in Table 12. The optimal result aligns with the observations made from the comparison graphs. The low friction factor configuration matches the low pressure drop regions identified from the graphs, with a longer distance to front allowing for smooth development, shallower angle resulting in less disruption to the flow, and a short length to reduce the overall winglet area, decreasing drag. This naturally results in a reduced Colburn factor.

The optimal Colburn factor result features a larger winglet length, steeper angle and much shorter distance from front. The longer length allows for a larger surface area, ensuring the winglet can achieve maximum effectiveness. The steeper angle increases the redirecting effect of the winglet. The shorter distances effectively disrupts the boundary layer early, promoting turbulence and ensuring maximum effectiveness of the delta winglet.

Naturally, the optimal point lies in between the lowest friction factor and highest Colburn factor points.

Table 12. Multi-objective pattern search results for delta winglet optimisation

	Length (mm)	Angle (°)	Distance from front (mm)	R1 FF % Difference	R1 CF % difference	Original FNoC FF% Difference	Original FNoC CF% Difference
Best FF	2.60	8.74	17.51	0.47	-1.58	-6.86	0.76
Best CF	7.22	19.27	6.66	1.73	2.14	-5.69	4.57
Optimal Result 1	5.92	14.21	12.03	1.02	1.49	-6.35	3.90

A simulation of the optimal result was fulfilled to ensure accuracy, and to investigate the resultant flow phenomena.

6.3 Verification of results

A simulation was performed to verify the observed optimal results from the surrogate model. The results are shown in Table 13, compared to the predicted results from the Kriging model. There is about a 0.1% difference in both friction factor and Colburn factor, which is well within the CFD modelling error.

Table 13. Comparison of simulated results to predicted results for delta winglets optimal configuration

	FF % Difference	CF % difference
Predicted	1.02	1.49
Simulated	1.10	1.39
Difference	0.08	-0.09

The performance of the optimal model was tested across the Reynolds number range, and the results are displayed in Figure 62, compared with the original FNoC and the optimised FNoC. Interestingly, at higher Reynolds numbers, the friction factor is lower than the optimised FNoC element. In this case, it appears that the delta winglets generate more efficient turbulent flow structures than those originally generated by the optimised FNoC design, leading to a reduction in pressure losses. The Colburn factor in this area also increases for the same reasons.

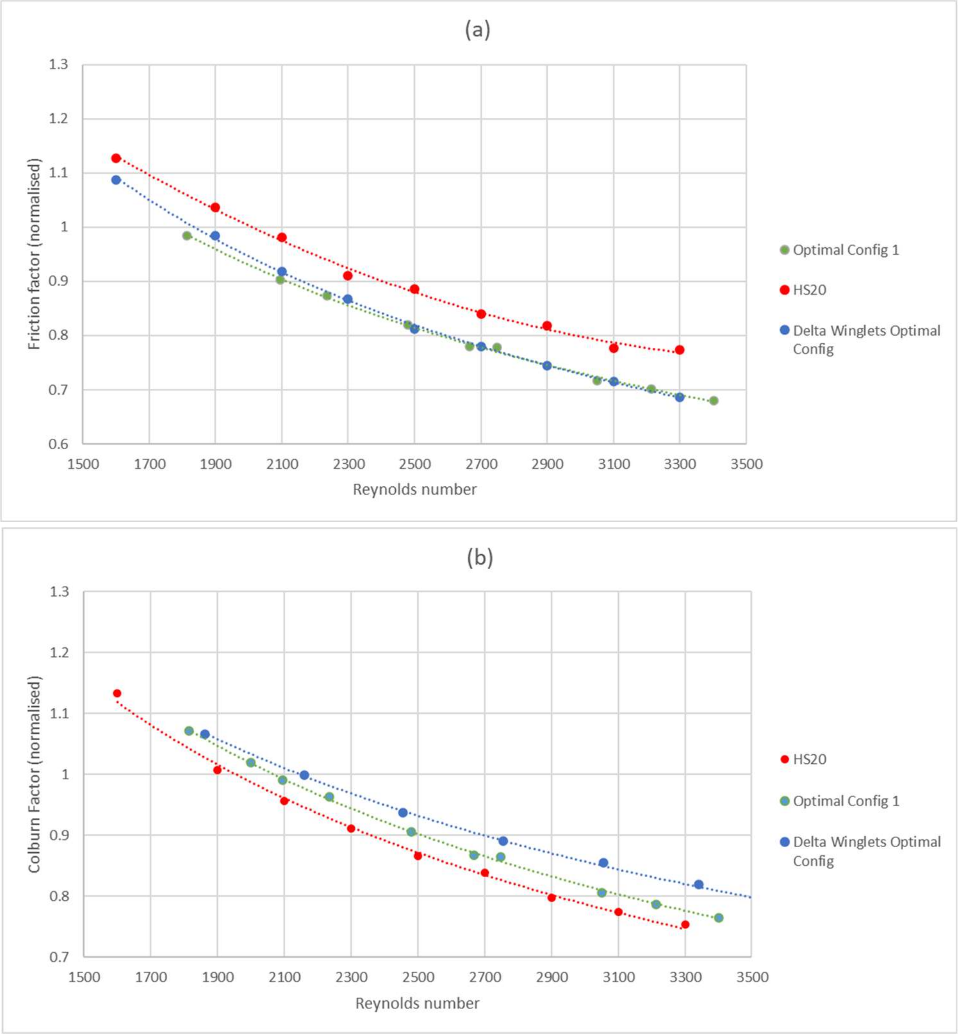

Figure 62. Performance across Reynolds number range of original FNoC, optimised FNoC and optimised FNoC with optimised delta winglets added

6.4 Analysis of flow behaviour

The flow through the part is shown in Figure 63 compared with the optimised FNoC model. Immediately, it is observed that the transition to turbulence occurs much earlier, and stronger vortex structures are generated. Specifically, there is a longitudinal vortex structure created by flow travelling over the peak of the notch, where the flow gathers and swirls in the following valley. This swirl flow develops into a longitudinal vortex through the length of the valley, increasing heat transfer on the downstream edge, where there was little activity prior to the addition of delta winglets. This effect is also present in other locations, and it is clear that low heat transfer zones are being activated by these longitudinal vortex structures.

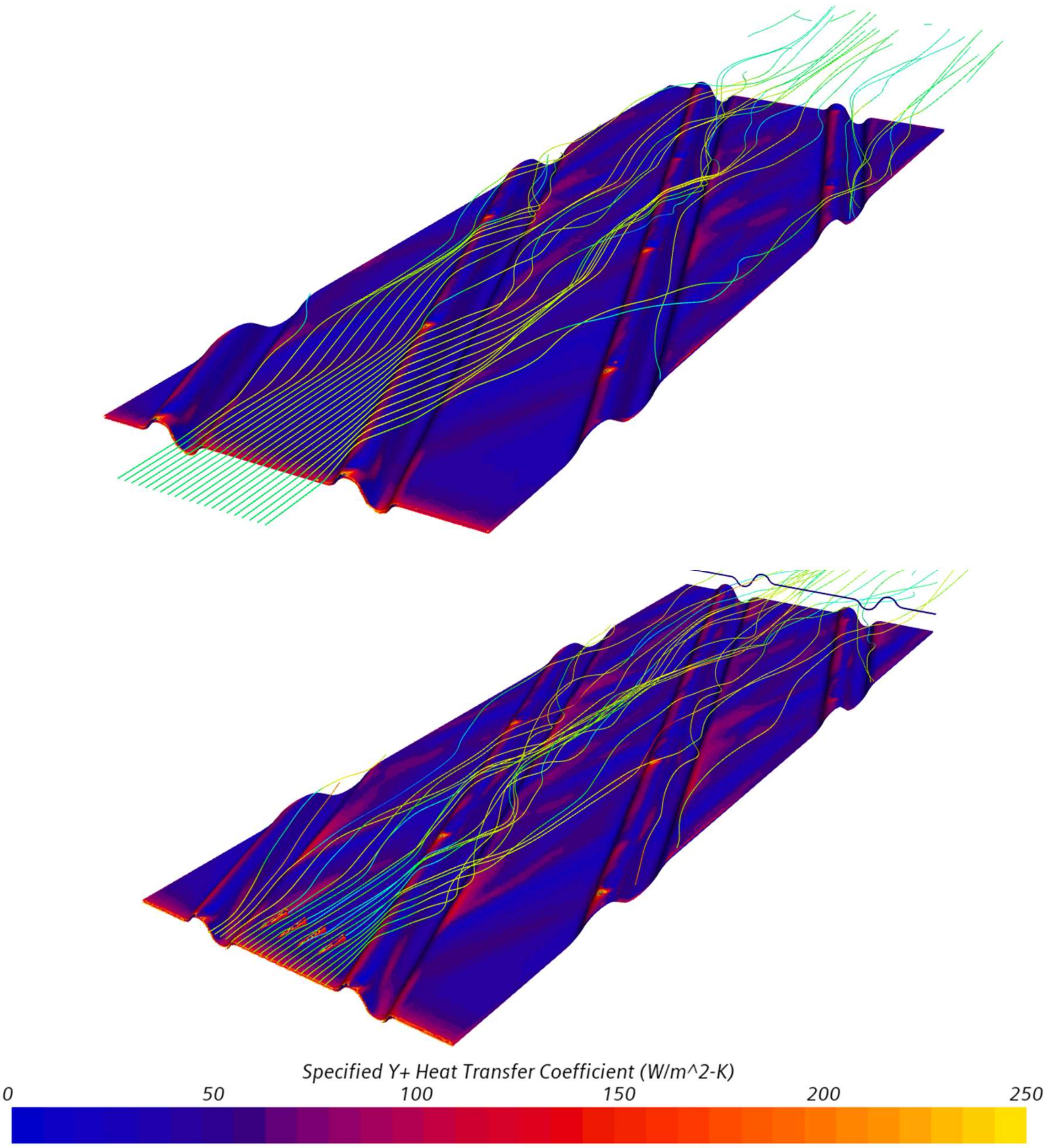

Figure 63. Comparison of flow behaviour through optimised FNoC (top) and optimised FNoC with optimal delta winglets added (bottom)

The heat transfer coefficient over the surface of each of the plates is shown in Figure 64. It is clear to see that there is an increase in heat transfer at the inlet of the plate, where the delta winglets are place. The longitudinal vortex structures create slim tendril-like areas of increased heat exchange across the surface of the plate. In the delta winglet model, these areas are brighter, indicating an increase in heat transfer, and by extension, vortex strength.

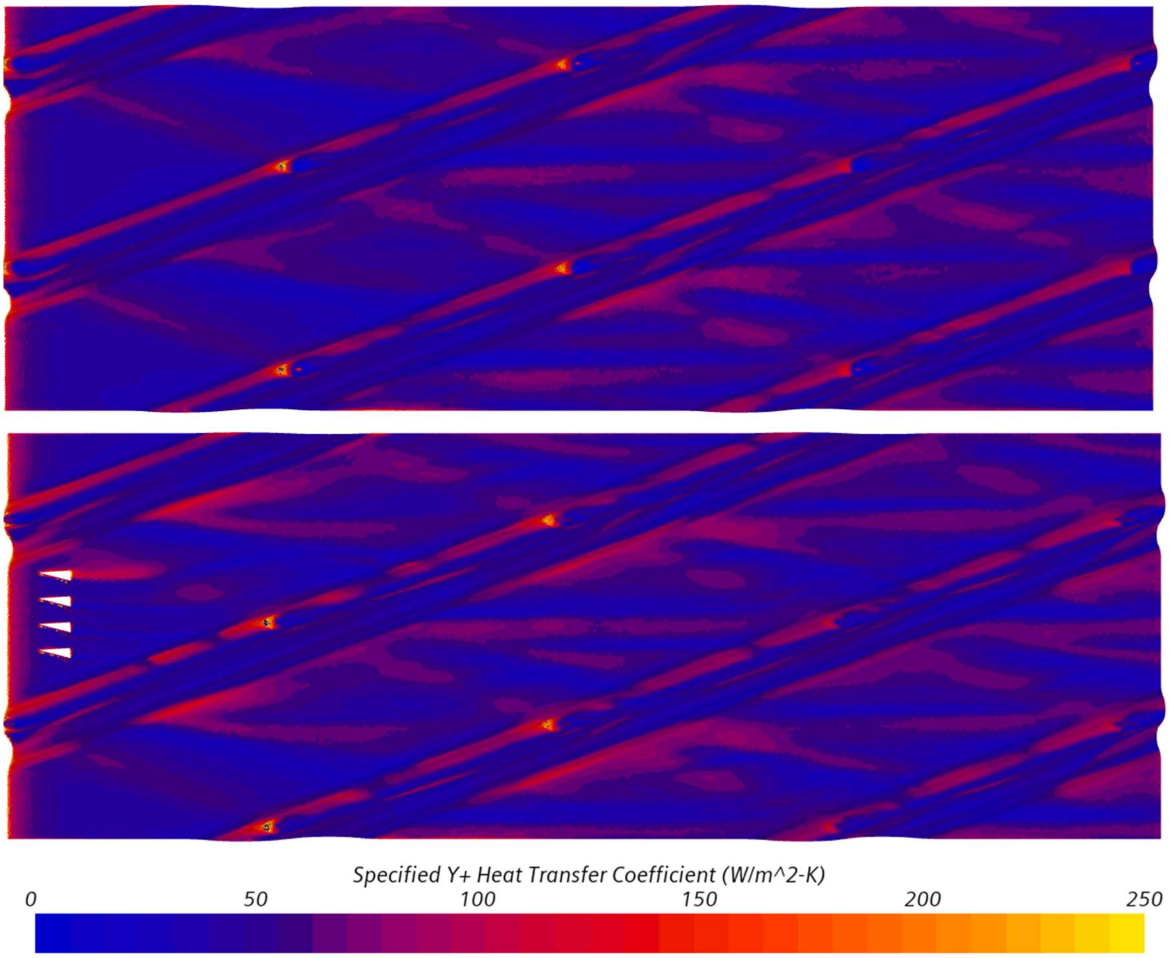

Figure 64. Comparison of heat transfer coefficient on surface of optimised FNoC (top) and optimised FNoC with DW (bottom)

A vector line visualisation is shown in Figure 65 for the optimised FNoC profile and the optimised FNoC profile with optimal delta winglets, In the optimised FNoC profile the vortex structures are clearly visible. There appears to be one strong vortex per each flat area of the plate, as well as some developing swirl flow within the curved areas of the notches. However, with the addition of delta winglets, the singular vortex is replaced by multiple counter-rotating vortices. As discussed previously, a vortex structure causes increased heat transfer at the plate surface. Splitting the large vortex into several smaller vortex structures evens out the heat transfer, resulting in a more uniform temperature distribution through the channel. This in turn raises the overall heat transfer effectiveness, as the area near the original strong vortex was previously saturated. By introducing multiple smaller vortices, the heat transfer across the plate becomes more efficient.

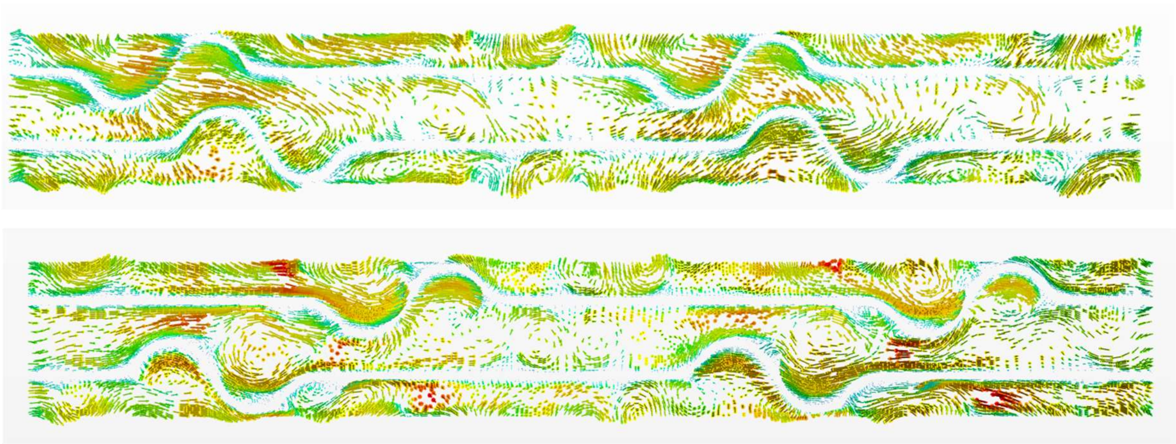

Figure 65. Velocity vector line visualisation at midplane of optimised FNoC (top) and optimised FNoC with optimal delta winglets added (bottom)

6.5 Delta winglet optimisation summary

In this section, the focus is on the optimisation of delta winglets added to an already optimised flat notched crossed plate to enhance its heat transfer capabilities. The delta winglets were strategically implemented to generate additional vortical structures that promote better mixing and heat transfer within the flow.

To identify the optimal configuration of the delta winglets, a Latin Hypercube Design of Experiments was conducted in conjunction with a Kriging surrogate model. This approach efficiently explored the design space by sampling various combinations of winglet parameters, including size, orientation, and placement.

The optimisation process yielded results that increased the overall heat transfer by 1.4%, with pressure losses increasing by 1.1% compared to the baseline optimised plate without winglets. The predicted optimal design was validated through CFD simulations, confirming the accuracy of the surrogate model's predictions and the effectiveness of the optimised winglet configuration.

Visualisation of the flow patterns and heat transfer distribution revealed significant enhancements. The addition of delta winglets led to the formation of longitudinal vortices generated as the flow moved over the notches and impacted the trailing edges of the troughs. These vortices replaced the main rotating vortex structure observed in the original flat notched crossed design with multiple smaller vortices. This transformation resulted in a more even distribution of heat transfer across the plate surface.

The smaller, counter-rotating vortices enhanced mixing and disrupted thermal boundary layers more effectively than the singular large vortex. This change not only increased the local heat transfer rates but also contributed to a more uniform temperature distribution throughout the channel. The redistribution of vortical structures was key to achieving the observed improvement in thermal performance, demonstrating the success of the optimisation strategy in leveraging aerodynamic features to enhance heat transfer.

7. Significance and Impact

This section evaluates the statistical significance of the results obtained in this thesis, with particular focus on the estimated modelling and experimental uncertainties. The aim is to determine the degree of confidence that can be placed in the observed improvements in performance parameters, such as the friction factor and Colburn factor. Beyond statistical interpretation, the potential commercial impact of these improvements is analysed, taking into account both operational and capital cost savings. Finally, the practicality of implementing the optimised designs in a real-world manufacturing context is considered, including any constraints or trade-offs that may arise during production and deployment. Together, this discussion provides a holistic view of the value and feasibility of the optimised delta winglets element type and Virtual Test Rig methodology.

7.1 Significance

The overall improvement of the FNoC element performance from the geometric optimisation scheme and addition of delta winglet vortex generators is a 6.35% reduction in friction factor and a 3.9% increase in Colburn factor. Based on the estimated modelling error, which ranges from +3.3% to −2.5% for friction factor and +4.4% to −4.8% for Colburn factor, the friction factor improvement exceeds the lower uncertainty bound by 3.85%. This suggests that the reduction in flow resistance is statistically significant and likely to be realised in practice. In contrast, the improvement in Colburn factor lies within the bounds of modelling uncertainty, falling 0.5% below the upper limit. As a result, this gain in heat transfer performance cannot be confidently classified as statistically significant based on the current uncertainty estimates.

The significance of the Colburn factor results may be improved by reducing the modelling error. A major contributor to this error is the experimental uncertainty, particularly the measurement uncertainty associated with the outlet temperature amplitude. While it may not be feasible to reduce the uncertainty of the testing apparatus itself, increasing the outlet temperature amplitude would result in a reduction in the percentage uncertainty. This can be implemented by reducing the length of the element plates, which would result in less heat transfer from between the flow and the plates, and a reduced outlet temperature amplitude, or increasing the amplitude of the inlet temperature. These factors are accounted for in the cyclic method, so the calculated heat transfer rate should not change. Similarly, another notable source of uncertainty arises from the measurement of plate thickness. This could be reduced by employing higher-precision instrumentation, such as an ultrasonic thickness gauge. These improvements would enhance the statistical significance of the observed improvements in performance and strengthen confidence in both the simulation outcomes and the reliability of the experimental testing process.

The improvements in Colburn factor, along with analysis discussed in this thesis, can provide a foundation for further research in the area. Broadening the scope of the delta winglet optimisation, and testing of other types of vortex generators could result in a Colburn factor improvement that is statistically significant.

From the optimisation charts, a clear and consistent trend is observed in which the Colburn factor increases toward the region of the optimal configuration. This convergence towards an optimum across multiple points on the response surface provides a level of robustness to the optimisation process. Even in the absence of statistically significant improvements within the experimental uncertainty bounds, the presence of a well-defined trend supports the validity of the model and offers an alternative form of confidence in the results. It suggests that the optimisation is not simply finding a local anomaly, but rather identifying a genuine performance improvement that aligns with underlying physical behaviour. This confidence can be strengthened by manufacturing the optimal configuration and testing it experimentally. Physical validation would provide a direct comparison with the baseline FNoC model and strengthen the credibility of the design improvements.

Another way to assess the significance of the results is by considering the broader performance balance. While the increase in Colburn factor falls within the bounds of modelling uncertainty and therefore may not be statistically significant, the reduction in friction factor exceeds the uncertainty range and is considered significant. From a practical perspective, this means that the optimised design achieves a measurable reduction in pressure drop without compromising heat transfer performance. In other words, the original thermal effectiveness is retained while improving flow efficiency, a highly desirable outcome in heat exchanger design.

7.2 Commercial Impact

The commercial impact is measured by using the change in friction factor and Colburn factor to determine the change in fan power, surface area, and length requirements for equivalent heat exchanger performance. The ideal improvement is utilised on the assumption that physical manufacture and testing shall be undertaken to verify the accuracy of the simulated results. To measure the impact, a case study of a rotary air preheater implemented in to a 125MW coal boiler energy generation process is examined. Comparative performance ratios will be calculated for the original FNoC element type and optimal delta winglets configuration, and used to calculate the economic benefit of the performance improvement. The cost of the elements is found from a case study undertaken in this area (154), and along with performance assumptions derived from typical specifications of a rotary heater of this size, provided by Howden. These assumptions enable a monetary estimate to be made from the performance improvements demonstrated in this thesis. However, it is acknowledged that this value may vary across the broad range of rotary heater designs and between different regions globally. As such, the estimate should be considered a comparative indicator of the potential economic benefit of improved element performance, rather than an absolute value.

7.2.1 Colburn factor

The commercial impact of the Colburn factor manifests in a reduction of the required heating surface area, which in turn drives a reduction in depth. The economic benefit is mainly in a reduction of the amount of elements required.

To gain insight into the cost of elements, the price of replacement elements in the rotary heater is listed as $251,000 in 2005 (154). In 2025, assuming the price tracks with inflation, this translates to $411,006.40, or £309,582.52 at the current exchange rate.

The Colburn factor can be related to the area by expanding the Stanton number equation, and utilising Newton's law of cooling to expand the heat transfer coefficient, as shown in Equation 7.2.1.

$$J = StPr^{\frac{2}{3}} = \frac{h}{\rho c_f \bar{u}} \cdot Pr^{\frac{2}{3}} = \frac{\dot{q}}{A_{surface} \Delta T} \cdot \frac{Pr^{\frac{2}{3}}}{\rho c_f \bar{u}} \tag{7.2.1}$$

Assuming that the fluid properties, overall velocity, temperature difference and overall heat transferred are constant, the change in Colburn factor can result in a change of area, as shown in Equation 7.2.2.

$$\frac{A_{surface_1}}{A_{surface_2}} \approx \frac{J_1}{J_2} \tag{7.2.2}$$

For constant thickness plates, the volume can be approximated to that of a flat rectangular plate as the notch pattern is periodic and uniform across the length of the plate. The volume is therefore equal to the cross-sectional area multiplied by the length, and the surface area multiplied by the thickness. The cross-sectional area of the plate is equal to the length of the top edge of the cross-section multiplied by the thickness. The volume can then be found using Equation

$$V_{element} = A_{surface} \cdot thickness = L \cdot p_{top} \cdot thickness \tag{7.2.3}$$

Where p_{top} is the perimeter of the top side of the cross-section of the element plate.

Therefore, assuming constant thickness, the ratio of volumes can be stated as Equation 7.2.4

$$\frac{V_{element_2}}{V_{element_1}} = \frac{A_{surface_1}}{A_{surface_2}} \tag{7.2.4}$$

Therefore, an increase in Colburn factor of 3.9% results in a volume reduction of 3.75%. Assuming that the elements are priced at a constant material and volume, this results in a cost saving of £11,609.34 in the cost of the elements alone.

7.2.2 Friction Factor

The impact of the reduced friction factor is seen in a reduced fan power requirement.

$$f = \frac{2 \cdot \Delta P \cdot D_h}{L \cdot \rho_f \cdot \bar{u}^2} \tag{3.1.10}$$

Assuming fluid density and average velocity are constant, hydraulic diameter may change marginally from the change in geometry, length will change from reduction in element surface area requirement, the pressure drop can be expressed as Equation 7.2.5.

$$\Delta P = \frac{f \cdot L}{D_h} \cdot (2 \cdot \bar{u}^2 \cdot \rho_f) \tag{7.2.5}$$

The overall change in pressure drop can then be related to the change in friction factor, hydraulic diameter and length. The ratio of pressure drops between the two geometries can be expressed in Equation 7.2.6:

$$\frac{\Delta P_2}{\Delta P_1} = \frac{D_{h_1}}{D_{h_2}} \cdot \frac{f_2}{f_1} \cdot \frac{L_2}{L_1} \tag{7.2.6}$$

From Equation 7.2.3, the surface area can be expressed in terms of length and top perimeter of the cross-section, as in Equation 7.2.7.

$$A_{surface} = Length * p_{top} \tag{7.2.7}$$

The ratio of lengths can then be expressed in terms of the ratio of surface area and top perimeter, as in Equation 7.2.8.

$$\frac{L_1}{L_2} = \frac{A_1}{A_2} \cdot \frac{p_{top_2}}{p_{top_1}} \tag{7.2.8}$$

As calculated previously, the inverse area ratio is $\frac{A_1}{A_2}$ = 1.039, top perimeter is found from CAD to be $\frac{p_{top_2}}{p_{top_1}}$ = 1.108, therefore $\frac{L_1}{L_2}$ = 1.15. This results in a reduction of length of 13.1%.

Therefore, from Equation 7.2.6, with a calculated hydraulic diameter ratio of $\frac{D_{h_1}}{D_{h_2}}$ = 1.023 and the simulated friction factor ratio as $\frac{f_2}{f_1}$ = 0.9365, the overall pressure top ratio between the two geometries $\frac{\Delta P_2}{\Delta P_1}$ is 0.832.

The fan affinity laws allow the performance of fans to be compared across different variables (155). Assuming the fluid density and the fan dimensions remain constant, the pressure drop ratio can be related to the rotational speed of the fan, as in Equation 7.2.9.

$$\frac{\Delta P_2}{\Delta P_1} = \left(\frac{rpm_2}{rpm_1}\right)^2 \tag{7.2.9}$$

With the same assumptions, the shaft power ratio can be related to the rotational speed of the fan, as in Equation 7.2.10.

$$\frac{Power_2}{Power_1} = \left(\frac{rpm_2}{rpm_1}\right)^3 \tag{7.2.10}$$

With $\frac{\Delta P_2}{\Delta P_1} = 0.832$, $\frac{Pow\quad_2}{Power_1} = 0.759$, leading to a reduction in required power of 24.1%.

The fan shaft power can be calculated using Equation 7.2.11. A fan efficiency is typically taken into account, but for simplicity the efficiency will be taken as 100%.

$$Power_1 = \Delta P_1 \cdot \dot{V} \tag{7.2.11}$$

Where $\dot{V}$ is the volumetric flow rate.

An air side pressure drop of around 1.2 kPa is common on 125MW coal boiler rotary air preheaters. An estimate of 30 kg/s mass flow rate through each side of a heater attached to a 125MW boiler is reasonable. Air temp increases from 30°C to 340°C through the rotary heater, an average of 185°C is used to find the density, which is 0.9005 kg/m3. This translates to a volumetric flow rate of 33.31 m3/s.

The air side fan power is therefore 39.98 kW. At an electricity price of £87.68 per MWh (156), the airside fan operational cost would be £3.52 per hour. A reduction in power requirement would save 24.1% of costs, or £0.85 per hour. The 125MW case study uses a value of 8,760 hours per year, assuming the process has no downtime. A 75% operational time is more reasonable, resulting in 6,570 hours per year. With this value, the implementation of the optimal winglets element type could save £5,566.31 per year through the reduction of pressure losses in the air side of the heater. A similar saving could be seen in the gas side. Coal flue gas has slightly different properties to air, and a gas side pressure drop of 1.8kPa is typical for this case. The volumetric flow rate is assumed to be equal to air. Evaluating the power using Equation 1 results in a power value of 59.9 kW, result in an operating cost of £1.27 per hour. With a reduction in power requirement of 24.1%, a saving of £1.27 per hour is found, resulting in a saving of £8,349.47 per year. Therefore, a total saving of £13,915.78 can be realised per heater per year.

7.2.3 Commercial Impact Summary

The total saving from both the friction factor and Colburn factor improvements is estimated at £13,915.78 per heater per year operational saving, along with a reduction in capital expenditure of £11,609.34 per heater at today’s exchange rate.

Additional cost reductions may arise from decreased material usage, simplified manufacturing, and lower transportation costs for the rotor, housing, and other structural components. Furthermore, the reduced number of elements and shallower rotor depth would likely decrease the torque required by the drive motor, contributing to further operational savings. While these benefits are more challenging to quantify accurately, they represent meaningful value. The benefit to the manufacturer lies not only in reduced production costs but also in delivering a more efficient, cost-effective, and competitive product to market.

Table 14. Summary of commercial impact case study

Factor	Value
Colburn factor increase, $\frac{J_2}{J_1}$	1.039
Surface Area decrease, $\frac{A_{surface_1}}{A_{surface_2}}$	0.9625
Cost of elements	£309,582.52
Reduction in cost of elements	£11,609.34
Element length decrease, $\frac{L_2}{L_1}$	0.869
Pressure drop decrease, $\frac{\Delta P_2}{\Delta P_1}$	0.832
Fan power requirement decrease $\frac{Power_2}{Power_1}$	0.759
Mass flow rate of air, $\dot{m}_{air}$	30 kg/s
Volumetric flow rate, $\dot{V}$	33.31 m3/s
Air fan power requirement	39.98 kW
Gas fan power requirement	59.97 kW
Operational hours per year	6570 hours
Electricity cost	£88 / MWh
Air fan power cost reduction	£5,566.31
Gas fan power cost reduction	£8,349.47
Total power cost reduction	£13,915.78

7.3 Practicality of implementation

Implementing the Virtual Test Rig as an intermediate step in the development of heat transfer elements represents a valuable enhancement to the overall efficiency and reliability of the design program. By incorporating accurate CFD-based predictions into the workflow, the reliance on costly and time-consuming physical prototyping can be significantly reduced.

Currently, the element development process begins with CAD modelling of a new design, followed by the fabrication of custom rollers required for the cold-rolling manufacturing process. A batch of elements is then produced, shipped to the test location in Glasgow, and evaluated using a physical test rig. In Howden, this full cycle typically takes around six months, although it can take longer if manufacturing resources are committed to customer projects. The process also incurs substantial costs: the creation of new rollers is capital-intensive, and further expenses arise from manufacturing the batch of elements, shipping logistics and the labour required for testing. If a novel geometry fails to meet performance expectations, these resources have been essentially wasted.

By integrating the Virtual Test Rig into this workflow, the performance of new geometries can be accurately predicted before physical production begins. This greatly reduces the risk of failure, enabling engineers to test bolder or more experimental designs without fear of incurring high costs. Moreover, the CFD-led process makes it feasible to explore a broader range of design variations than would be practical with physical testing alone.

The optimisation methods developed in this thesis also offer a major improvement over a traditional trial-and-error approach. Previously, a handful of discrete configurations might be tested, for example, notch pitches of 20 mm, 30 mm, and 40 mm, with the best result chosen. However, the true optimum may lie between those points, such as at 33 mm. Using CFD-driven optimisation, a much finer resolution of the design space can be explored, increasing the likelihood of identifying the true performance peak. This also reduces the number of physical variants that need to be manufactured and tested.

Importantly, the optimisation methodology can be automated using commercially available CFD software suites with integrated CAD capabilities, many of which are already in use in industry. The methodology relies on accessible solvers and standard design-of-experiments techniques, making it immediately deployable by engineering teams familiar with simulation-led design.

By replacing iterative physical testing with validated CFD-based surrogate models, the design cycle for new heat transfer elements can be significantly shortened, enabling faster product development with fewer resource demands.

To demonstrate the potential cost and time savings in a real-world context, a case study has been developed through information gathered from Howden.

7.3.1 Cost of implementation Case Study

A case study has been generated to estimate the implementation costs of the virtual test rig methodology. A comparative estimation of the price of physical testing has been developed.

The cost of an appropriate specification high-performance compute server is estimated to be around £50,000, although cloud computing HPC services are available. For a simple comparison, cloud computing prices can be easily found and extrapolated to calculate a total cost for an optimisation and testing scheme.

The virtual test rig takes around 100 hours on 32 cores to run 10 simulations covering the range of velocity test points. An optimisation scheme of 20 configurations at one velocity test point, plus a verification run of the optimal results at 10 test points takes around 300 hours on 32 cores.

Amazon Web Services offer a high-performance cloud computing program tailored to scientific and engineering modelling and simulations. The pricing for a 32 core cluster is listed as $1.4512 per hour, equating to an hourly fee of £1.09 plus £0.218 VAT, for a total of £1.308 per hour at the time of writing. For a 300 hour optimisation run, this results in a cost of £392.40. Data storage costs $0.088 (£0.0792 including VAT at the time of writing) per gigabyte per month. Each simulation file is around 11 gigabytes resulting in a total of 330 gigabytes for the 30 total simulations in an optimisation scheme. Assuming storage is required for one month, this results in a storage cost of £26.14 (157).

An estimated 20 hours of labour is required to set up the optimisation scheme, gather results and present data. At a standard consultancy rate of £100/hour, this would result in a cost of £2000.

The total cost of running an optimisation scheme on the virtual test rig is therefore £2418.54. It is worth noting that since the compute cost is relatively low compared to labour, expanding the number of configurations in the optimisation scheme may improve the quality of results without a substantial increase in total cost.

Table 15. Itemised costing of an optimisation scheme on the Virtual Test Rig

Item	Cost
HPC cost	£392.40
Data storage	£26.14
CFD Labour	£2,000.00
Total	£2,418.54

Traditional testing involves manufacturing physical prototypes and running controlled experiments. According to cost data provided by the Howden product development department, the fabrication of tooling, manufacture of an element test pack and associated logistics costs total around £20,000.

The physical element testing requires around 8 hours of labour, for measuring the elements, installing them into the test rig, running the experiments and gathering the results. Using the consultancy rate of £100/hour as previously, this results in a cost of £800.

Table 16. Itemised cost of manufacture and testing of elements

Item	Cost
Manufacture	£20,000.00
Testing	£800.00
Total	£20,800.00

In the specific case of the FNoC plate discussed previously, the generation of three prototype test packs at varying pitch values cost around £60,000, with a testing cost of £2400, for a total of £62,400. By implementing the virtual test rig, the cost of the optimisation scheme would have been £2418.54, the manufacture of the optimal configuration would cost £20,000, and the testing would have cost £800, for a total of £23,218.54. Therefore, a saving of £39181.46 could be realised. Moreover, additional value is provided through an overall improved final product, deeper insight into the fluid and thermal behaviour through CFD analysis, and reduced time and material waste from unnecessary physical trials.

Table 17. Cost saving of virtual test rig compared to prototype approach

Approach	Cost
Virtual Test Rig + physical testing	£23,218.54
Testing of 3 prototypes	£62,400.00
Difference	£39,181.46

This case study illustrates the substantial economic and technical benefits of incorporating the Virtual Test Rig into the heat transfer element design process. While the costs and assumptions may vary depending on the element type and design complexity, the demonstrated savings and improvements in design quality suggest that the Virtual Test Rig is a valid and beneficial intermediate step in the design process.

To reduce the risk stemming from the estimated modelling error, a hybrid approach may be adopted. This would involve utilising the Virtual Test Rig to explore a wide range of design configurations, followed by the physical manufacture and testing of two to three selected optimal designs. This strategy will confirm that the predicted performance trends are accurate, the assumptions made in the simulation set up are valid and will ensure a broader understanding of the performance across the variable ranges.

A brief cost analysis of this is strategy is shown in Table 18. An estimation of 50 design configurations, and full velocity range analysis runs of 3 optimal results should take around 800 hours on 32 cores, for a total cost of around £1700. The data storage for 80 simulation files for 2 months will cost £226.51. An additional 20 hours of labour is estimated to be sufficient, as with automated optimisation techniques the 50 design configurations shouldn't take much longer than 20. The total cost is £68,326.91, around £6000 more than the cost of testing the FNoC prototypes.

Table 18. Itemised cost of hybrid testing approach

Item	Cost per	Amount	Total Cost
AWS HPC	£1.31	1300	£1,700.40
Data storage	£0.08	2860	£226.51
Labour	£100.00	40	4000
Manufacture	£20,000.00	3	£60,000.00
Testing	£800.00	3	£2,400.00
Total			£68,326.91

8. Conclusions and Further Work

This thesis investigates the heat transfer and fluid dynamic characteristics of complex-profiled element plates within a rotary regenerative heat exchanger. The main focus is determining the factors that influence the performance of the element plates and understanding how to manipulate those factors to improve the heat transfer effectiveness.

This thesis has discussed the state of the art of the rotary regenerative heat exchanger, including its place in industry, current areas of research, and the importance of the heat transfer element plate geometry. Heat transfer enhancement techniques were reviewed and compared, with delta winglets selected as a key area of interest. Gaps in the literature were identified pertaining to the analysis of flow regimes within the heat storage matrix of RRHEs and the addition of heat transfer enhancement techniques to heat transfer elements plates.

A computational fluid dynamics model was set up using the large eddy simulation physics model to replicate the flow conditions of a physical element test rig. The CFD simulation was compared with multiple data sets of experimental results from three different element profiles.

The element profiles were successfully and accurately modelled in CFD, creating a valid “virtual test rig” to experiment and analyse the flow through complex geometry channels between heat transfer elements. The simulation model error bounds were calculated to be +3.3%, -2.5% friction factor, and +4.4%, -4.8% for Colburn factor. Crucial features of the flow were identified to create significant impact on the heat transfer and pressure drop characteristics, including longitudinal vortex structures, turbulent mixing and recirculation zones.

An optimisation scheme was carried out on the FNoC element profile, using a Latin Hypercube Design of Experiments and kriging surrogate model methodology to optimise the pitch and radius geometry dimensions by maximising heat transfer and minimising pressure drop. The scheme was a success, with the optimal configuration showing improvement of 2.3% in heat transfer and 7.3% in pressure drop. The results showed that a simple change in dimensions can completely change the flow characteristics of a rotary heater element plate, with the optimal geometry increasing the strength of the main longitudinal vortex structure and altering the process of turbulence generation across the element.

The optimisation scheme showed that the main driver of heat transfer enhancement was turbulent mixing and longitudinal vortex structures. The optimal configuration provided the best geometric layout to control and enhance the turbulence generated by the crossing notches. The visualisation of this turbulence can aid in the development of future element profiles by ensuring constructive turbulence structures are generated by geometry features.

Delta winglets were added to the optimised FNoC model, and optimised for length, angle and location. The optimal result improved the heat transfer of the optimised design by a further 1.49% while also increasing pressure drop by 1.02%. The delta winglets broke up the main longitudinal vortex structure into multiple smaller structures, resulting in more evenly distributed heat transfer across the plate. This can be especially useful in some plate geometries where “dead zones” are present, where very little heat transfer occurs. Distributing flow across the plate can allow these zones to activate and contribute to an increase in the overall heat transfer.

While the performance improvement from the delta winglets was not as significant as that of the geometric optimisation, it is still a valid demonstration of the usefulness of delta winglets in controlling flow.

The overall significance of the results was measured. The friction factor performance increase fell 3.85% outside of the model error bounds, however the Colburn factor improvement was 0.5% within the model error bounds, meaning that the friction factor results were statistically significant while the Colburn factor results were not.

The commercial impact of the simulated performance improvements on a typical rotary air preheater for a 125MW coal boiler showed an estimated operational cost reduction of £13,915.78 and a capital expenditure reduction of £11,609.34. The practicality of implementation of the Virtual Test Rig was studied, and an estimated saving of £39,181.46 was found compared to the physical prototype approach. A hybrid approach was suggested to improve the overall element design process and broaden the understanding of each element type, estimated to cost around £6000 more than the previous physical prototype method.

Work shall continue on this project into the future. Physical models of the optimal element designs shall be manufactured and tested to further strengthen accuracy and compliance of the CFD model with the test rig. Modifications to the test rig are recommended to reduce the experimental error in order to increase the significance of the Virtual Test Rig results. Further research into the optimal configurations and dimensions of plate styles should be researched, such that empirical correlations can be generated to minimise costs associated with trial-and-error style product development.

Further research shall be conducted in the area of vortex generators applied to rotary regenerative heater element plates. Whilst delta winglets were covered in the scope of this project, far more work could be done in several key areas. Further research into delta winglet configurations including height, number of winglets, multiple rows of winglets and others could result in further improvements in performance and fill gaps in current knowledge. Additionally, other types of winglets should be researched, specifically in regard to use with rotary heater element plates. Examples such as curved, spline-shaped, and rectangular punched configurations are promising novel technologies that could push heating performance further. Other types of vortex generation techniques such as artificial roughness, ribs, and dimples could also prove to be beneficial. Analysis of flow conditions compared across these scenarios could provide key insights into the detailed flow mechanisms present within these specific closed channel flows.

Additionally, studies involving the combination of multiple styles of vortex generators have shown that it is possible to compound heat transfer performance improvements, with examples of delta winglets combined with dimples resulting in the dimples transferring heat more effectively. This is a promising area of research that shall be investigated further.

Analysis of fouling conditions is a key area which fell outwith the scope of this project. Fouling is a significant issue for most complex element profile designs, as intricate areas can become clogged with dust, soot or other particulates. The development of a method to analyse a design and calculate a “fouling control factor” of some kind could provide significant upgrades to the current limited range of suitable solutions for high fouling applications.

Through this new understanding, a new development ethos could be built, to optimise future element profile designs, ensuring maximum efficiency is achieved.

9. Appendix

9.1 References

1. Singer JG. Combustion, fossil power : a reference book on fuel burning and steam generation [Internet]. Combustion Engineering; 1991. Available from: https://search.worldcat.org/title/26017244

2. Hansson S. A. Birger and Frederik Ljungstrom - Inventors. Finspong: Svenska turbinfabriks AB Ljungström; 1955.

3. Howden. Rotary Heater Technology. [cited 2022 Apr 24]; Available from: https://www.howden.com/getattachment/products-and-services/Heaters/Air-20Pre-20Heater-20Brochure.pdf?lang=en-GB

4. Warren I. Ljungstrom heat exchangers for waste heat recovery. J Heat Recovery Syst; (United Kingdom). 1982;2:3(3):257–71.

5. Wang L, He Y, Tang C, Wang Y, Che D. A novel design of rotary regenerative condensing heat exchanger for the dehydration from high humidity flue gas. International Journal of Heat and Mass Transfer. 2019 Mar 1;131:517–26.

6. Shah RK, Sekulić DP. Fundamentals of Heat Exchanger Design [Internet]. Fundamentals of Heat Exchanger Design. Wiley; 2003. Available from: https://onlinelibrary.wiley.com/doi/book/10.1002/9780470172605

7. Maxwell JC. Theory of Heat [Internet]. Theory of Heat. Cambridge University Press; 2011. Available from: https://www.cambridge.org/core/books/theory-of-heat/7052E2DAA4CD862126D5105ABBFFAD0F

8. Dhaiban HT, Hussein MA. The optimal design of heat sinks: A review. Journal of Applied and Computational Mechanics. 2020;6(4):1030–43.

9. Árpád IW, Kiss JT, Kocsis D. Role of the volume-specific surface area in heat transfer objects: A critical thinking-based investigation of Newton’s law of cooling. International Journal of Heat and Mass Transfer. 2024 Aug 1;227:125535.

10. Incropera FP, DeWitt DP, Bergman TL, Lavine AS. Fundamentals of Heat and Mass Transfer. 7th ed. 2011. 400–402 p.

11. Kobayashi H, Yaji K, Yamasaki S, Fujita K. Freeform winglet design of fin-and-tube heat exchangers guided by topology optimization. Applied Thermal Engineering. 2019 Oct 1;161:114020.

12. Kays WM, London AL, Eckert ERG. Compact Heat Exchangers [Internet]. Vol. 27, Journal of Applied Mechanics. American Society of Mechanical Engineers Digital Collection; 1960. 0 p. Available from: https://dx.doi.org/10.1115/1.3644004

13. Kakaç S. Heat transfer enhancement of heat exchangers. Kluwer Academic Publishers; 1999. 676 p.

14. U Tube Heat Exchanger - Design for ASME / TEMA / API [Internet]. [cited 2024 Oct 2]. Available from: http://www.ansonindustry.com/pressure-vessel/u-tube-heat-exchanger.html

15. Kakaç S, Liu H, Pramuanjaroenkij A. Heat Exchangers : Selection, Rating, and Thermal Design, Second Edition [Internet]. CRC Press; 2002 [cited 2021 Aug 27]. Available from: https://www.taylorfrancis.com/books/mono/10.1201/9781420053746/heat-exchangers-sadik-kaka%C3%A7-hongtan-liu-anchasa-pramuanjaroenkij

16. He L, Li P. Numerical investigation on double tube-pass shell-and-tube heat exchangers with different baffle configurations. Applied Thermal Engineering. 2018 Oct 1;143:561–9.

17. Milani Shirvan K, Mamourian M, Abolfazli Esfahani J. Experimental study on thermal analysis of a novel shell and tube heat exchanger with corrugated tubes: Exergetic sustainability along with sensitivity analysis. Journal of Thermal Analysis and Calorimetry [Internet]. 2019 Oct 1 [cited 2024 Oct 2];138(2):1583–606. Available from: https://link.springer.com/article/10.1007/s10973-019-08308-3

18. Sadighi Dizaji H, Jafarmadar S, Asaadi S. Experimental exergy analysis for shell and tube heat exchanger made of corrugated shell and corrugated tube. Experimental Thermal and Fluid Science. 2017 Feb 1;81:475–81.

19. Liu S, Yin Y, Tu A, Zhu D. Experimental investigation on shell-side performance of a novel shell and tube oil cooler with twisted oval tubes. International Journal of Thermal Sciences. 2020 Jun 1;152:106290.

20. Dagdevir T, Ozceyhan V. An experimental study on heat transfer enhancement and flow characteristics of a tube with plain, perforated and dimpled twisted tape inserts. International Journal of Thermal Sciences. 2021 Jan 1;159:106564.

21. Ayub ZH, Yang D, Khan TS, Al-Hajri E, Ayub AH. Performance characteristics of a novel shell and tube heat exchanger with shell side interstitial twisted tapes for viscous fluids application. Applied Thermal Engineering. 2018 Apr 1;134:248–55.

22. Wang L., Sundén Bengt, Manglik RM. Plate heat exchangers : design, applications and performance. Wang L, editor. WIT Press; 2007. 1–269 p.

23. Arsenyeva OP, Tovazhnyanskyy LL, Kapustenko PO, Khavin GL, Yuzbashyan AP, Arsenyev PY. Two types of welded plate heat exchangers for efficient heat recovery in industry. Applied Thermal Engineering. 2016 Jul 25;105:763–73.

24. Lee J, Lee KS. Friction and Colburn factor correlations and shape optimization of chevron-type plate heat exchangers. Applied Thermal Engineering. 2015 Oct 5;89:62–9.

25. Kanaris AG, Mouza AA, Paras S V. Optimal design of a plate heat exchanger with undulated surfaces. International Journal of Thermal Sciences. 2009 Jun 1;48(6):1184–95.

26. Hsieh CT, Jang JY. Parametric study and optimization of louver finned-tube heat exchangers by Taguchi method. Applied Thermal Engineering. 2012 Sep 1;42:101–10.

27. Han D, Lee KJ. Experimental study on condensation heat transfer enhancement and pressure drop penalty factors in four microfin tubes. International Journal of Heat and Mass Transfer. 2005 Aug 1;48(18):3804–16.

28. Bukasa JP, Liebenberg L, Meyer JP. Influence of Spiral Angle on Heat Transfer during Condensation inside Spiralled Micro-Fin Tubes. Heat Transfer Engineering [Internet]. 2005 Sep [cited 2024 Oct 7];26(7):11–21. Available from: https://www.tandfonline.com/doi/abs/10.1080/01457630590959278

29. Miyara A, Otsubo Y. Condensation heat transfer of herringbone micro fin tubes. International Journal of Thermal Sciences. 2002 Jun 1;41(7):639–45.

30. Kilkovský B. Review of Design and Modeling of Regenerative Heat Exchangers. Energies 2020, Vol 13, Page 759 [Internet]. 2020 Feb 9 [cited 2025 Apr 4];13(3):759. Available from: https://www.mdpi.com/1996-1073/13/3/759/htm

31. Boxu Z, Qi L, Shilong D, Bowen L. Research on Ash Clogging of Rotary Air Preheater in Coal-fired Power Plant. [cited 2025 Apr 23]; Available from: https://doi.org/10.1051/e3sconf/202126101006

32. Skiepko T. Effect of reduction in seal clearances on leakages in a rotary heat exchanger. Heat Recovery Systems and CHP. 1989 Jan 1;9(6):553–9.

33. Praveen M, Kishore PS. (PDF) Effectiveness of Rotary Air Preheater in a Thermal Power Plant. International Journal of Scientific Engineering and Technology. 2016 Dec 1;5(12):526–31.

34. Stosic N. Numerical analysis of heat transfer and fluid flow in rotary regenerative air pre-heaters. Proceeding of Thermal Sciences 2004 Proceedings of the ASME - ZSIS International Thermal Science Seminar II [Internet]. 2004 [cited 2025 Apr 16]; Available from: https://www.academia.edu/53386274/Numerical_analysis_of_heat_transfer_and_fluid_flow_in_rotary_regenerative_air_pre_heaters

35. Leong KC, Toh KC, Wong SH. Microcomputer-based design of rotary regenerators. Heat Recovery Systems and CHP. 1991 Jan 1;11(6):461–70.

36. Howden. Howden Trusted Advisor Training Course. Glasgow; 2020.

37. Cai M, Hui S, Wang X, Zhao S, He S. A study on the direct leakage of rotary air preheater with multiple seals. Applied Thermal Engineering. 2013 Sep 25;59(1–2):576–86.

38. Cai M, Hui S, Wang X, Zhao S, He S. A study on the direct leakage of rotary air preheater with multiple seals. Applied Thermal Engineering. 2013 Sep 25;59(1–2):576–86.

39. Chen Z, Li H, Gu Y, Zhu W. A novel flexible seal technology and its application in heat transfer of rotary air preheater. Applied Thermal Engineering. 2019 Dec 25;163.

40. Shayan MR, Ranjbar K, Hajidavalloo E, Heidari Kydan A. On the Failure Analysis of an Air Preheater in a Steam Power Plant. Journal of Failure Analysis and Prevention. 2015 Dec 1;15(6):941–51.

41. Zayed ME, Zhao J, Elsheikh AH, Hammad FA, Ma L, Du Y, et al. Applications of cascaded phase change materials in solar water collector storage tanks: A review. Solar Energy Materials and Solar Cells. 2019 Sep 1;199:24–49.

42. Wang L, Wang C, Guo Y, Wu Y, Bai W, Che D. Novel rotary regenerative heat exchanger using cascaded phase change material capsules. Applied Thermal Engineering [Internet]. 2021 Apr 1 [cited 2022 Apr 24];188. Available from: https://doi.org/10.1016/j.applthermaleng.2021.116619

43. Dongwon AHE. HEATING ELEMENT PROFILE – 동원AHE [Internet]. [cited 2020 Nov 8]. Available from: http://dongwonahe.com/?page_id=774&ckattempt=2

44. Modi A, Haque A, Pratap B, Kumar Bansal I, Kumar P, Saravanan S, et al. A Review on Air Preheater Elements Design and Testing. Review on Air Preheater Elements Design and Testing Mechanics, Materials Science & Engineering Journal [Internet]. 2017 [cited 2022 Apr 24]; Available from: https://hal.archives-ouvertes.fr/hal-01966399

45. Stasiek JA. Experimental studies of heat transfer and fluid flow across corrugated-undulated heat exchanger surfaces. International Journal of Heat and Mass Transfer. 1998;41(6–7):899–914.

46. Lee YM, Chung H, Kim SH, Bae HS, Cho HH. Optimization of the Heating Element in a Gas-Gas Heater Using an Integrated Analysis Model. Energies 2017, Vol 10, Page 1932 [Internet]. 2017 Nov 23 [cited 2022 May 24];10(12):1932. Available from: https://www.mdpi.com/1996-1073/10/12/1932/htm

47. Naphon P, Kornkumjayrit K. Numerical analysis on the fluid flow and heat transfer in the channel with V-shaped wavy lower plate. International Communications in Heat and Mass Transfer. 2008 Aug 1;35(7):839–43.

48. Naphon P. Laminar convective heat transfer and pressure drop in the corrugated channels. International Communications in Heat and Mass Transfer. 2007 Jan 1;34(1):62–71.

49. Metwally HM, Manglik RM. Enhanced heat transfer due to curvature-induced lateral vortices in laminar flows in sinusoidal corrugated-plate channels. International Journal of Heat and Mass Transfer. 2004 May 1;47(10–11):2283–92.

50. Wang CC, Chen CK. Forced convection in a wavy-wall channel. International Journal of Heat and Mass Transfer. 2002 Jun 1;45(12):2587–95.

51. Oviedo-Tolentino F, Romero-Méndez R, Hernández-Guerrero A, Girón-Palomares B. Use of diverging or converging arrangement of plates for the control of chaotic mixing in symmetric sinusoidal plate channels. Experimental Thermal and Fluid Science. 2009 Jan 1;33(2):208–14.

52. Focke WW, Zachariades J, Olivier I. The effect of the corrugation inclination angle on the thermohydraulic performance of plate heat exchangers. International Journal of Heat and Mass Transfer. 1985 Aug 1;28(8):1469–79.

53. Cernecky J, Koniar J, Brodnianska Z. The effect of heat transfer area roughness on heat transfer enhancement by forced convection. Journal of Heat Transfer [Internet]. 2014 Apr 1 [cited 2023 Apr 30];136(4). Available from:

https://asmedigitalcollection-asme-org.ezproxy.lib.gla.ac.uk/heattransfer/article/136/4/041901/396478/The-Effect-of-Heat-Transfer-Area-Roughness-on-Heat

54. Forooghi P, Stripf M, Frohnapfel B. A systematic study of turbulent heat transfer over rough walls. International Journal of Heat and Mass Transfer. 2018 Dec 1;127:1157–68.

55. Prasad BN, Saini JS. Optimal thermohydraulic performance of artificially roughened solar air heaters. Solar Energy. 1991 Jan 1;47(2):91–6.

56. Taslim ME, Li T, Kercher DM. Darryl E. Metzger Memorial Session Paper: Experimental Heat Transfer and Friction in Channels Roughened With Angled, V-Shaped, and Discrete Ribs on Two Opposite Walls. Journal of Turbomachinery [Internet]. 1996 Jan 1 [cited 2023 Apr 29];118(1):20–8. Available from: https://asmedigitalcollection.asme.org/turbomachinery/article/118/1/20/433465/Darryl-E-Metzger-Memorial-Session-Paper

57. Aharwal KR, Gandhi BK, Saini JS. Experimental investigation on heat-transfer enhancement due to a gap in an inclined continuous rib arrangement in a rectangular duct of solar air heater. Renewable Energy. 2008 Apr 1;33(4):585–96.

58. Tanda G. Effect of rib spacing on heat transfer and friction in a rectangular channel with 45° angled rib turbulators on one/two walls. International Journal of Heat and Mass Transfer. 2011 Feb 1;54(5–6):1081–90.

59. Chai L, Tassou SA. A Review of Airside Heat Transfer Augmentation with Vortex Generators on Heat Transfer Surface. Energies [Internet]. 2018 Oct 1 [cited 2023 Apr 27];11(10):2737. Available from: https://doaj.org/article/b9143333c6cc47d5a7964537b52b9118

60. Liu H ling, Li H, He Y ling, Chen Z tao. Heat transfer and flow characteristics in a circular tube fitted with rectangular winglet vortex generators. International Journal of Heat and Mass Transfer. 2018 Nov 1;126:989–1006.

61. Sun Z, Zhang K, Li W, Chen Q, Zheng N. Investigations of the turbulent thermal-hydraulic performance in circular heat exchanger tubes with multiple rectangular winglet vortex generators. Applied Thermal Engineering. 2020 Mar 5;168:114838.

62. Fiebig M, Kallweit P, Mitra N, Tiggelbeck S. Heat transfer enhancement and drag by longitudinal vortex generators in channel flow. Experimental Thermal and Fluid Science. 1991;4(1):103–14.

63. Tiggelbeck S, Mitra NK, Fiebig M. Comparison of Wing-Type Vortex Generators for Heat Transfer Enhancement in Channel Flows. Journal of Heat Transfer [Internet]. 1994 Nov 1 [cited 2023 Apr 29];116(4):880–5. Available from: https://asmedigitalcollection.asme.org/heattransfer/article/116/4/880/424809/Comparison-of-Wing-Type-Vortex-Generators-for-Heat

64. Lei YG, He YL, Tian LT, Chu P, Tao WQ. Hydrodynamics and heat transfer characteristics of a novel heat exchanger with delta-winglet vortex generators. Chemical Engineering Science. 2010 Mar 1;65(5):1551–62.

65. Li HY, Chen CL, Chao SM, Liang GF. Enhancing heat transfer in a plate-fin heat sink using delta winglet vortex generators. International Journal of Heat and Mass Transfer. 2013 Dec 1;67:666–77.

66. He J, Liu L, Jacobi AM. Air-side heat-transfer enhancement by a new winglet-type vortex generator array in a plain-fin round-tube heat exchanger. Journal of Heat Transfer [Internet]. 2010 Jul 1 [cited 2023 Apr 29];132(7):1–9. Available from: https://asmedigitalcollection-asme-org.ezproxy.lib.gla.ac.uk/heattransfer/article/132/7/071801/451325/Air-Side-Heat-Transfer-Enhancement-by-a-New

67. Zhou G, Ye Q. Experimental investigations of thermal and flow characteristics of curved trapezoidal winglet type vortex generators. Applied Thermal Engineering. 2012 May 1;37:241–8.

68. Sarangi SK, Mishra DP, Mishra P. Parametric Investigation of Wavy Rectangular Winglets for Heat Transfer Enhancement in a Fin-and–Tube Heat Transfer Surface. Journal of Applied Fluid Mechanics [Internet]. 2020 Jan 1 [cited 2023 Jun

7];13(2):615–28. Available from: https://doaj.org/article/81fc50a1f73a4985a2a717b6412688b2

69. Modi AJ, Rathod MK. Comparative study of heat transfer enhancement and pressure drop for fin-and-circular tube compact heat exchangers with sinusoidal wavy and elliptical curved rectangular winglet vortex generator. International Journal of Heat and Mass Transfer. 2019 Oct 1;141:310–26.

70. Gupta S, Roy A, Gupta A, Gupta M. Numerical Simulations of Performance of Plate Fin Tube Heat Exchanger Using Rectangular Winglet Type Vortex Generator with Punched Holes. SAE Technical Papers [Internet]. 2019 Apr 2 [cited 2024 Sep 26];2019-April(April). Available from: https://www.sae.org/publications/technical-papers/content/2019-01-0145/

71. Han Z, Xu Z. Experimental and numerical investigation on particulate fouling characteristics of vortex generators with a hole. International Journal of Heat and Mass Transfer. 2020 Feb 1;148:119130.

72. Modi AJ, Kalel NA, Rathod MK. Thermal performance augmentation of fin-and-tube heat exchanger using rectangular winglet vortex generators having circular punched holes. International Journal of Heat and Mass Transfer. 2020 Sep 1;158:119724.

73. Khan MZU, Akbar B, Sajjad R, Rajput UA, Mastoi S, Uddin E, et al. Investigation of heat transfer in dimple-protrusion micro-channel heat sinks using copper oxide nano-additives. Case Studies in Thermal Engineering. 2021 Dec 1;28:101374.

74. Isaev SA, Schelchkov A V., Leontiev AI, Baranov PA, Gulcova ME. Numerical simulation of the turbulent air flow in the narrow channel with a heated wall and a spherical dimple placed on it for vortex heat transfer enhancement depending on the dimple depth. International Journal of Heat and Mass Transfer. 2016 Mar 1;94:426–48.

75. Bi C, Tang GH, Tao WQ. Heat transfer enhancement in mini-channel heat sinks with dimples and cylindrical grooves. Applied Thermal Engineering. 2013 Jun 1;55(1–2):121–32.

76. Zhang F, Liao G, Sundén B. Numerical investigations on the effect of convex-dimple streamwise arrangements on the flow and heat transfer characteristics of rectangular convex-dimple-grooved channels. Numerical Heat Transfer, Part A: Applications [Internet]. 2020 Aug 7 [cited 2024 Sep 26];78(9):443–60. Available from: https://www.tandfonline.com/doi/abs/10.1080/10407782.2020.1802926

77. Choi SM, Kwon HG, Choi S, Bang M, Moon HK, Cho HH. Delta-Winglet-Pair for Enhancing Cooling Performance of a Single Dimple Imprinted Internal Channel. International Journal of Heat and Mass Transfer. 2021 Oct 1;178:121647.

78. Luo L, Wen F, Wang L, Sundén B, Wang S. On the solar receiver thermal enhancement by using the dimple combined with delta winglet vortex generator. Applied Thermal Engineering. 2017 Jan 25;111:586–98.

79. Bandler JW, Cheng QS, Dakroury SA, Mohamed AS, Bakr MH, Madsen K, et al. Space mapping: The state of the art. IEEE Transactions on Microwave Theory and Techniques. 2004 Jan;52(1 II):337–61.

80. Box GEP, Wilson KB. On the Experimental Attainment of Optimum Conditions. Journal of the Royal Statistical Society Series B (Methodological) [Internet]. 1951 [cited 2022 Apr 25];13(1):1–45. Available from: https://www-jstor-org.ezproxy.lib.gla.ac.uk/stable/2983966?pq-origsite=summon&seq=1

81. Myers RH. Response Surface Methodology—Current Status and Future Directions. Journal of Quality Technology [Internet]. 2018 [cited 2022 Apr 25];31(1):30–44. Available from: https://www.tandfonline.com/doi/abs/10.1080/00224065.1999.11979891

82. Zhong GY, Yang P, Liu YW. Heat transfer and pressure drop correlations by means of response surface methodology. International Journal of Heat and Mass Transfer. 2018 Apr 1;119:312–32.

83. Kim KY, Lee YM. Design Optimization of Internal Cooling Passage with V-shaped Ribs. Numerical Heat Transfer, Part A: Applications [Internet]. 2007 Jan [cited 2022 Apr 24];51(11):1103–18. Available from: https://www.tandfonline.com/doi/abs/10.1080/10407780601112860

84. Mohapatra T, Sahoo SS, Padhi BN. Analysis, prediction and multi-response optimization of heat transfer characteristics of a three fluid heat exchanger using response surface methodology and desirability function approach. Applied Thermal Engineering. 2019 Mar 25;151:536–55.

85. Kola PVKV, Pisipaty SK, Mendu SS, Ghosh R. Optimization of performance parameters of a double pipe heat exchanger with cut twisted tapes using CFD and RSM. Chemical Engineering and Processing - Process Intensification [Internet]. 2021;163:108362. Available from: https://www.sciencedirect.com/science/article/pii/S0255270121000660

86. Sacks J, Welch WJ, Mitchell TJ, Wynn HP. Design and Analysis of Computer Experiments. Stastical Science [Internet]. 1989 Nov 1 [cited 2022 Apr 25];4(4):409–23. Available from: https://projecteuclid.org/journals/statistical-science/volume-4/issue-4/Design-and-Analysis-of-Computer-Experiments/10.1214/ss/1177012413.full

87. Simpson TW, Mauery TM, Korte JJ, Mistree F. Comparison of response surface and kriging models for multidisciplinary design optimization. 7th AIAA/USAF/NASA/ISSMO Symposium on Multidisciplinary Analysis and Optimization [Internet]. 1998 [cited 2022 Apr 25];381–91. Available from: https://arc.aiaa.org/doi/abs/10.2514/6.1998-4755

88. Simpson TW, Booker AJ, Ghosh D, Giunta AA, Koch PN, Yang RJ. Approximation methods in multidisciplinary analysis and optimization: A panel discussion. Structural and Multidisciplinary Optimization. 2004;27(5):302–13.

89. Mohammadi-Ahmar A, Mohammadi A, Raisee M. Efficient uncertainty quantification of turbine blade leading edge film cooling using bi-fidelity combination of compressed sensing and Kriging. International Journal of Heat and Mass Transfer [Internet]. 2020 [cited 2022 Apr 25];162:120360. Available from: https://doi.org/10.1016/j.ijheatmasstransfer.2020.120360

90. Kim KY, Shin DY. Optimization of a staggered dimpled surface in a cooling channel using Kriging model. International Journal of Thermal Sciences [Internet].

2008 [cited 2022 Apr 25];47:1464–72. Available from: www.elsevier.com/locate/ijts

91. Augspurger M, Choi KK, Udaykumar HS. Optimizing fin design for a PCM-based thermal storage device using dynamic Kriging. International Journal of Heat and Mass Transfer. 2018 Jun 1;121:290–308.

92. Villarrubia G, De Paz JF, Chamoso P, la Prieta F De. Artificial neural networks used in optimization problems. Neurocomputing [Internet]. 2018 Jan 10 [cited 2022 Apr 24];272:10–6. Available from: http://dx.doi.org/10.1016/j.neucom.2017.04.075

93. Çolak AB, Kirkar SM, Gönül A, Dalkilic AS. Assessment of heat transfer characteristics of a corrugated heat exchanger based on various corrugation parameters using artificial neural network approach. International Journal of Heat and Fluid Flow. 2024 Sep 1;108:109455.

94. Alharthi MA, Almohammadi BA, Sharafeldin MA, Abdelghany MT, Bendoukha S, Refaey HA. Heat transfer and pressure drop of Al2O3/water nanofluid in conically coiled tubes: Experimental and artificial neural network prediction. Case Studies in Thermal Engineering. 2024 Feb 1;54:104043.

95. Shuqi Z, Limei Y, Goyal V, Alghanmi S, Alkhalifah T, Alkhalaf S, et al. Artificial neural network-based optimization of baffle geometries for maximized heat transfer efficiency in microchannel heat sinks. Case Studies in Thermal Engineering. 2023 Sep 1;49:103331.

96. Yang J, Cheng K, Zhang K, Huang C, Huai X. Hybrid artificial neural networks-based approaches predicting the heat transfer and flow characteristics of manifold microchannels. Applied Thermal Engineering. 2024 Dec 15;257:124446.

97. Antony Jiju. Design of experiments for engineers and scientists. 2003;152.

98. McKay MD, Beckman RJ, Conover WJ. Comparison of three methods for selecting values of input variables in the analysis of output from a computer code. Technometrics. 1979;21(2):239–45.

99. Iman RL. Latin Hypercube Sampling. Encyclopedia of Quantitative Risk Analysis and Assessment [Internet]. 2008 Sep 15 [cited 2022 Apr 25]; Available from: https://onlinelibrary.wiley.com/doi/full/10.1002/9780470061596.risk0299

100. Fang KT, Li R, Sudjianto A. Design and Modeling for Computer Experiments (Chapman & Hall/CRC Computer Science & Data Analysis). 2005 [cited 2022 Apr 25]; Available from: http://www.amazon.com/exec/obidos/redirect?tag=citeulike07-20&path=ASIN/1584885467

101. Rajabi MM, Ataie-Ashtiani B, Janssen H. Efficiency enhancement of optimized Latin hypercube sampling strategies: Application to Monte Carlo uncertainty analysis and meta-modeling. Advances in Water Resources [Internet]. 2014 [cited 2022 Apr 25];76. Available from: http://dx.doi.org/10.1016/j.advwatres.2014.12.008

102. Packham N. Combining Latin Hypercube Sampling With Other Variance Reduction Techniques.

103. Fischer BR. Mechanical Tolerance Stackup and Analysis. 2nd ed. Taylor & Francis Group; 2011.

104. Li H, Xu S, Keyser J. Optimization for statistical tolerance allocation. Computer Aided Geometric Design. 2019 Nov 1;75:101788.

105. Hasofer AM, Lind NC. An Exact and Invariant First Order Reliability Format. Journal of Engineering Mechanics. 1974;100:111–21.

106. Michael W, Siddall JN. The Optimal Tolerance Assignment With Less Than Full Acceptance. Journal of Mechanical Design [Internet]. 1982 Oct 1 [cited 2024 Jan 23];104(4):855–60. Available from: https://dx.doi.org/10.1115/1.3256448

107. Wu F, Dantan JY, Etienne A, Siadat A, Martin P. Improved algorithm for tolerance allocation based on Monte Carlo simulation and discrete optimization. Computers & Industrial Engineering. 2009 May 1;56(4):1402–13.

108. Gerth RJ, Islam Z. Towards A Designed Experiments Approach to Tolerance Design. Geometric Design Tolerancing: Theories, Standards and Applications

[Internet]. 1998 [cited 2024 Oct 9];337–45. Available from: https://link.springer.com/chapter/10.1007/978-1-4615-5797-5_26

109. Shoukr DShL, Gadallah MH, Metwalli SM. The Reduced Tolerance Allocation Problem. [Giza]: Cairo University; 2016.

110. Milani Shirvan K, Mirzakhanlari S, Kalogirou SA, Öztop HF, Mamourian M. Heat transfer and sensitivity analysis in a double pipe heat exchanger filled with porous medium. International Journal of Thermal Sciences. 2017 Nov 1;121:124–37.

111. Dezan DJ, Rocha AD, Ferreira WG. Parametric sensitivity analysis and optimisation of a solar air heater with multiple rows of longitudinal vortex generators. Applied Energy. 2020 Apr 1;263:114556.

112. The Bakerian lecture on the increase of electrical resistance in conductors with rise of temperature, and its application to the measure of ordinary and furnace temperatures ; also on a simple method of measuring electrical resistances. Proceedings of the Royal Society of London [Internet]. 1871 Dec 31 [cited 2025 Mar 17];19(123–129):443–5. Available from: https://archive.org/details/philtrans09056316

113. Feder J, Flekkøy EG, Hansen A. Physics of Flow in Porous Media [Internet]. Physics of Flow in Porous Media. Cambridge University Press; 2022 [cited 2025 Mar 28]. Available from: https://www.cambridge.org/core/books/physics-of-flow-in-porous-media/C510E8435AB620F9D80196102C210CE7

114. Bird RB, Stewart WE, Lightfoot EN. Transport Phenomena , 2nd Edition. Anderson W, Hepburn K, Kulek P, editors. Transport Phenomena. 2nd ed. 2002;422–53.

115. Linford A. Flow measurement and meters. 2nd ed. London: E. & F. N. Spon; 1961.

116. Reader-Harris M. Orifice Plates and Venturi Tubes. Cham: Springer International Publishing; 2015. (Experimental Fluid Mechanics).

117. Kijärvi J. Darcy Friction Factor Formulae in Turbulent Pipe Flow [Internet]. 2011 Jul [cited 2022 Apr 24]. Available from: http://www.kolumbus.fi/jukka.kiijarvi/clunowa/clunowa.html

118. Meek RMG. Measurement of Heat-transfer Coefficients in Randomly Packed Beds by the Cyclic Method. National Engineering Laboratory Report No 54. 1962 Sep.

119. Coleman HW, Steele WG. Experimentation, Validation, and Uncertainty Analysis for Engineers: Third Edition [Internet]. Experimentation, Validation, and Uncertainty Analysis for Engineers: Third Edition. John Wiley and Sons; 2009 [cited 2025 Mar 21]. 1–317 p. Available from: https://onlinelibrary.wiley.com/doi/book/10.1002/9780470485682

120. Bensow R, Fureby C, Liefvendahl M, Persson T. A Comparative Study of RANS, DES and LES. In: Conference: 26th ONR Symposium on Naval Hydrodynamics. 2006.

121. Som S, Senecal P, Pomraning E. Comparison of RANS and LES Turbulence Models against Constant Volume Diesel Experiments. Engineering, Environmental Science [Internet]. 2012 [cited 2022 Apr 24]; Available from: https://www.semanticscholar.org/paper/Comparison-of-RANS-and-LES-Turbulence-Models-Volume-Som-Senecal/42a68199923a49eafdfabf91b4821eb3dfe01a12

122. Spalart PR, Jou WH, Strelets M, Allmaras SR, Research USAFO of S. Comments on the Feasibility of LES for Wings, and on a Hybrid RANS/LES Approach. International conference; 1st, Advances in DNS/LES: Direct numerical simulation and large eddy simulation [Internet]. 1997;1(1):137–48. Available from: https://www.tib.eu/en/search/id/BLCP%3ACN032430290/Decaying-Turbulence-in-Two-and-Three-Dimensions/

123. Yu C, Xue X, Shi K, Shao M, Liu Y. Comparative Study on CFD Turbulence Models for the Flow Field in Air Cooled Radiator. Processes 2020, Vol 8, Page 1687 [Internet]. 2020 Dec 21 [cited 2024 Sep 30];8(12):1687. Available from: https://www.mdpi.com/2227-9717/8/12/1687/htm

124. Wei Z, Ge Y. Computational Comparison of DES and LES in Channel Flow Simulation. Computational Structural Engineering [Internet]. 2009 [cited 2024 Sep 30];417–24. Available from: https://link.springer.com/chapter/10.1007/978-90-481-2822-8_46

125. Ciofalo M, Di Piazza I, Stasiek JA. Investigation of flow and heat transfer in corrugated-undulated plate heat exchangers. Heat and Mass Transfer/Waerme- und Stoffuebertragung [Internet]. 2000 Sep [cited 2022 Dec 27];36(5):449–62. Available from: https://www.researchgate.net/publication/225898595_Investigation_of_flow_and_heat_transfer_in_corrugated-undulated_plate_heat_exchangers

126. Coleman GN, Sandberg RD. A primer on direct numerical simulation of turbulence - methods, procedures and guidelines. Southampton: University of Southampton; 2010.

127. Wang J, Zhao Y. Heat and fluid flow characteristics of a rectangular channel with a small diameter circular cylinder as vortex generator. International Journal of Thermal Sciences. 2015 Jun 1;92:1–13.

128. Jiansheng W, Yu J, Xueling L. Heat transfer and flow characteristics in a rectangular channel with small scale vortex generators. International Journal of Heat and Mass Transfer. 2019 Aug 1;138:208–25.

129. Sohankar A. Heat transfer augmentation in a rectangular channel with a vee-shaped vortex generator. International Journal of Heat and Fluid Flow. 2007 Apr 1;28(2):306–17.

130. Large Eddy Simulation for Incompressible Flows. Large Eddy Simulation for Incompressible Flows. Springer-Verlag; 2006.

131. Smagorinsky J. General Circulation Experiments with the Primitive Equations. MWRv [Internet]. 1963 [cited 2024 Sep 30];91(3):99. Available from: https://ui.adsabs.harvard.edu/abs/1963MWRv...91...99S/abstract

132. Germano M, Piomelli U, Moin P, Cabot WH. A dynamic subgrid-scale eddy viscosity model. Physics of Fluids A: Fluid Dynamics [Internet]. 1991 Jul 1 [cited 2024 Sep 30];3(7):1760–5. Available from: /aip/pof/article/3/7/1760/402287/A-dynamic-subgrid-scale-eddy-viscosity-model

133. Elcner J, Lizal F, Jedelsky J, Tuhovcak J, Jicha M. Laminar-turbulent transition in a constricted tube: Comparison of Reynolds-averaged Navier–Stokes turbulence models and large eddy simulation with experiments. Advances in Mechanical Engineering [Internet]. 2019 May 27 [cited 2024 Sep 30];11(5). Available from: https://journals.sagepub.com/doi/full/10.1177/1687814019852261

134. Nicoud F, Ducros F. Subgrid-scale stress modelling based on the square of the velocity gradient tensor. Flow, Turbulence and Combustion [Internet]. 1999 [cited 2024 Sep 30];62(3):183–200. Available from: https://link.springer.com/article/10.1023/A:1009995426001

135. Blazek J. Computational Fluid Dynamics: Principles and Applications, Second Edition. Computational Fluid Dynamics: Principles and Applications, Second Edition. Elsevier; 2006. 1–470 p.

136. Greenshields, Christopher and Weller H. Notes on Computational Fluid Dynamics General Principles [Internet]. CFD Direct Ltd. CFD Direct Ltd; 2022 [cited 2025 Apr 7]. 291 p. Available from: https://doc.cfd.direct/notes/cfd-general-principles/index/

137. Simão M, Besharat M, Carravetta A, Ramos HM. Flow Velocity Distribution Towards Flowmeter Accuracy: CFD, UDV, and Field Tests. Water 2018, Vol 10, Page 1807 [Internet]. 2018 Dec 8 [cited 2025 Apr 15];10(12):1807. Available from: https://www.mdpi.com/2073-4441/10/12/1807/htm

138. Convective heat transfer [Internet]. 2021 [cited 2025 May 2]. Available from: https://community.sw.siemens.com/s/article/Convective-heat-transfer

139. Coleman HW. Standard for Verification and Validation in Computational Fluid Dynamics and Heat Transfer: ASME V&V 20. The American Society of Mechanical Engineers (ASME). 2009.

140. Simcenter STAR-CCM+ Validation and Verification Suite [Internet]. [cited 2025 Apr 28]. Available from: https://community.sw.siemens.com/s/question/0D54O000061xkTCSAY/simcenter-starccm-validation-and-verification-suite

141. Carasik LB, Hassan YA, Wang H. Verification and Validation of CFD Simulations involving Twin Rectangular Jets using Steady RANS in Star-CCM+. Vol. 115, Transactions of the American Nuclear Society. 2016 Jul.

142. Pointer WD. STAR-CCM+ Verification and Validation Plan [Internet]. Oak Ridge, TN (United States); 2016 Sep [cited 2025 Apr 28]. Available from: http://www.osti.gov/servlets/purl/1335352/

143. Roache PJ. Verification and Validation in Computational Science and Engineering. Hermosa Publishers; 1998.

144. Celik IB, Ghia U, Roache PJ, Freitas CJ, Coleman H, Raad PE. Procedure for estimation and reporting of uncertainty due to discretization in CFD applications. Journal of Fluids Engineering, Transactions of the ASME [Internet]. 2008 Jul 1 [cited 2025 Apr 28];130(7):0780011–4. Available from: https://dx.doi.org/10.1115/1.2960953

145. Roache PJ. Quantification of uncertainty in computational fluid dynamics. Annual Review of Fluid Mechanics [Internet]. 1997 Jan 1 [cited 2025 Apr 28];29(Volume 29, 1997):123–60. Available from: https://www.annualreviews.org/content/journals/10.1146/annurev.fluid.29.1.123

146. Wilcox DC. Turbulence Modeling for CFD, Volume 1 [Internet]. DCW Industries,. DCW industries La Canada; 2006 [cited 2024 Sep 12]. 522 p. Available from: https://books.google.com/books/about/Turbulence_Modeling_for_CFD.html?id=tFNNPgAACAAJ

147. Oaks W, Paoletti S. Polyhedral Mesh Generation. International Meshing Roundtable Conference. 2000;

148. Paz C, Suárez E, Conde M, Vence J. Development of a Computational Fluid Dynamics Model for Predicting Fouling Process Using Dynamic Mesh Model. Heat Transfer Engineering [Internet]. 2020 Jan 19 [cited 2024 Oct 2];41(2):199–207. Available from: https://www.tandfonline.com/doi/abs/10.1080/01457632.2018.1522108

149. Huang S, Guo J, Yang FX. Numerical simulation of 3D unsteady flow in a rotating pump by dynamic mesh technique. IOP Conference Series: Materials Science and Engineering [Internet]. 2013 Dec 20 [cited 2024 Oct 2];52(2):022030. Available from: https://iopscience.iop.org/article/10.1088/1757-899X/52/2/022030

150. Cant RS, Ahmed U, Fang J, Chakarborty N, Nivarti G, Moulinec C, et al. An unstructured adaptive mesh refinement approach for computational fluid dynamics of reacting flows. Journal of Computational Physics. 2022 Nov 1;468:111480.

151. Zhang Z, Wang Y, Jimack PK, Wang H. Meshingnet: A new mesh generation method based on deep learning. Lecture Notes in Computer Science (including subseries Lecture Notes in Artificial Intelligence and Lecture Notes in Bioinformatics) [Internet]. 2020 [cited 2024 Oct 2];12139 LNCS:186–98. Available from: https://link.springer.com/chapter/10.1007/978-3-030-50420-5_14

152. Schlichting H, Gersten K. Boundary-Layer Theory. Boundary-Layer Theory. Springer Berlin Heidelberg; 2016. 1–799 p.

153. Gunantara N. A review of multi-objective optimization: Methods and its applications. Cogent Engineering [Internet]. 2018 Jan 1 [cited 2025 May 5];5(1):1–16. Available from: https://www.tandfonline.com/doi/pdf/10.1080/23311916.2018.1502242

154. Costs And Effectiveness Of Upgrading And Refurbishing Older Coal-Fired Power Plants In Developing Apec Economies [Internet]. 2005 Jun [cited 2025 May 6]. Available from: www.apec.org

155. Çengel Yunus A., Cimbala John M. Fluid Mechanics Fundamentals and Applications [Internet]. Fluid Mechanics: Fundamentals and Applications. McGraw

Hill; 2014 [cited 2025 May 8]. 185–242 p. Available from: 192.168.6.56/handle/123456789/23915

156. National Grid: Live [Internet]. [cited 2025 May 9]. Available from: https://grid.iamkate.com/

157. EC2 On-Demand Instance Pricing – Amazon Web Services [Internet]. [cited 2025 May 5]. Available from: https://aws.amazon.com/ec2/pricing/on-demand/

9.2 Uncertainty analysis

Value	Fractional Uncertainty								
Test Point	1	2	3	4	5	6	7	8	9
Pack Porosity	0.0018	0.0018	0.0018	0.0018	0.0018	0.0018	0.0018	0.0018	0.0018
Flow area	0.0030	0.0030	0.0030	0.0030	0.0030	0.0030	0.0030	0.0030	0.0030
Hydraulic Diameter	0.0051	0.0051	0.0051	0.0051	0.0051	0.0051	0.0051	0.0051	0.0051
Density	0.0056	0.0056	0.0056	0.0056	0.0056	0.0056	0.0056	0.0056	0.0056
Beta	0.0002	0.0002	0.0002	0.0002	0.0002	0.0002	0.0002	0.0002	0.0002
Expansability	0.0015	0.0015	0.0015	0.0015	0.0016	0.0016	0.0017	0.0019	0.0023
mass flow	0.0033	0.0033	0.0033	0.0034	0.0034	0.0034	0.0035	0.0037	0.0042
velocity	0.0071	0.0071	0.0071	0.0071	0.0071	0.0072	0.0072	0.0073	0.0076
Dynamic Viscosity	0.0014	0.0014	0.0013	0.0014	0.0014	0.0014	0.0014	0.0014	0.0014
Reynolds Number	0.0069	0.0069	0.0069	0.0069	0.0069	0.0070	0.0070	0.0071	0.0074
K2	0.0250	0.0250	0.0250	0.0250	0.0250	0.0250	0.0250	0.0250	0.0250
K1	0.0258	0.0260	0.0264	0.0261	0.0261	0.0261	0.0261	0.0261	0.0261
heat transfer	0.0266	0.0279	0.0357	0.0298	0.0335	0.0340	0.0351	0.0336	0.0357
Nusselt	0.0361	0.0340	0.0355	0.0343	0.0339	0.0303	0.0361	0.0283	0.0271
Prandtl	0.0014	0.0014	0.0013	0.0014	0.0014	0.0014	0.0014	0.0014	0.0014
Colburn	0.0281	0.0292	0.0301	0.0311	0.0336	0.0341	0.0345	0.0352	0.0367
Friction	0.0163	0.0163	0.0164	0.0165	0.0165	0.0166	0.0168	0.0173	0.0183

9.3 MATLAB code

```
clear all


cla
clc
clf('reset')

startup

load 'simulation_data.mat'


%% Winglets optimisation
```

```
Length = Variables(:,1);
Angle = Variables(:,2);
Distance = Variables(:,3);

LB = [2 0 0];
UB = [10 40 20];

ff = Sims(:,1);
cf = Sims(:,2);

lb = LB;
ub = UB;



%% Kriging friction factor

samples = [Length Angle Distance];
values = [ff];


x = (LB+UB) ./ 2;
hyperparamaters0 = x;

opts.lambda0 = 0;
opts.lambdaBounds = [-5 ; 5]; % log scale
k = oodacefit(samples, values);
y = k.predict(x);

%h = plotKrigingModel(k, LB, UB);
k = k.fit(samples, values);

disp(y)
global k
clear samples
clear values

%% Kriging process colburn factor

samples = [Length Angle Distance];
values = [cf];


%  x = [6 20 10];

k2 = oodacefit(samples, values);
y = k2.predict(x);
k2 = k2.fit(samples, values);

disp(y)
y= k2.predict(x);
disp(y)

%h = plotKrigingModel(k2, LB, UB);
k2 = k2.fit(samples, values);

global k2

%% single opbjective optimisation
lb = [2,0,0];
ub = [10,40,20];
```

```
x0 = [60,20,10];
func = @cfopti_fun;
options = optimoptions("patternsearch");
x1 = patternsearch(func,x0,[],[],[],[],lb,ub);

y = k.predict(x1);
y2 = k2.predict(x1);

table(x1,y,y2)
ans1 = [x1 y y2];

funf = @ffopti_fun;
options = optimoptions("patternsearch");
x2 = patternsearch(funf,x0,[],[],[],[],lb,ub);

y = k.predict(x2);
y2 = k2.predict(x2);

table(x2,y,y2)

ans2 = [x2 y y2];

%% multi -objective optimisation

fun = @opti_funcn
lb = [2,0,0];
ub = [10,40,20];
A = [];
b = [];
Aeq = [];
beq = [];
x0 = [2,0,0]; %starting point if required

options = optimoptions("gamultiobj","PopulationSize",2000,
"FunctionTolerance",0.0000001);
x3 = gamultiobj(fun,3,A,b,Aeq,beq,lb,ub, options);


%Presenting results in table form
y = k.predict(x3);
y2 = k2.predict(x3);

gamans= table(x3,y,y2);

ans3 = [x3 y y2];

%% Creating surrogate model space



D = 3;
n=1;

for A = 0:1:40

    for L = 2:1:10

        Z = [L, A, D];
            y = k.predict(Z);
            y2 = k2.predict(Z);
```

```
            LAGraph(n,1)=L;
            LAGraph(n,2)=A;
            LAGraph(n,3)=y;
            LAGraph(n,4)=y2;

            n=n+1;

    end

end

% Creating plots - Distance vs Length

A = 10;
n=1;

for D = 0:1:20

    for L = 2:1:10

        Z = [L, A, D];
            y = k.predict(Z);
            y2 = k2.predict(Z);

            LDGraph(n,1)=L;
            LDGraph(n,2)=D;
            LDGraph(n,3)=y;
            LDGraph(n,4)=y2;

            n=n+1;

    end

end

% Creating plots - Angle vs Distance

L = 5;
n=1;

for A = 0:1:40

    for D = 0:1:20

        Z = [L, A, D];
            y = k.predict(Z);
            y2 = k2.predict(Z);

            DAGraph(n,1)=D;
            DAGraph(n,2)=A;
            DAGraph(n,3)=y;
            DAGraph(n,4)=y2;

            n=n+1;

    end

end


%% Graphs
```

```
ZLff = [0.127 0.130]; %friction factor graphs z scale
ZLcf = [0.0103 0.011]; %colburn factor graphs z scale

figure(100)
tiledlayout(2,3);
fontsize(gcf,15,"pixels");
grid on

%Length vs angle
L = LAGraph(:,1);
A = LAGraph(:,2);
F = LAGraph(:,3);
xv = linspace(min(L), max(L), 200);
yv = linspace(min(A), max(A), 200);
[X,Y] = meshgrid(xv, yv);
Z = griddata(L,A,F,X,Y);

nexttile
%figure(2)
surf(X, Y, Z);
grid on
set(gca, 'ZLim',ZLff)
xlabel('Length (mm)')
ylabel('Angle (°)')
zlabel('friction factor')
shading interp
title('Angle/Length friction factor')

nexttile
%Angle vs distance
D = DAGraph(:,1);
A = DAGraph(:,2);
F = DAGraph(:,3);
xv = linspace(min(D), max(D), 200);
yv = linspace(min(A), max(A), 200);
[X,Y] = meshgrid(xv, yv);
Z = griddata(D,A,F,X,Y, 'v4');
surf(X, Y, Z);
grid on
xlabel('Distance from front (mm)')
ylabel('Angle(°)')
zlabel('friction factor')
set(gca, 'ZLim',ZLff)
shading interp
title('Angle/Distance friction factor')

nexttile
%length vs distance
L = LDGraph(:,1);
D = LDGraph(:,2);
F = LDGraph(:,3);
xv = linspace(min(D), max(D), 200);
yv = linspace(min(L), max(L), 200);
[X,Y] = meshgrid(xv, yv);
Z = griddata(D,L,F,X,Y, 'v4');
surf(X, Y, Z);
grid on
xlabel('Distance from front (mm)')
ylabel('Length (mm)')
zlabel('friction factor')
```

```
set(gca, 'ZLim',[ZLff])
shading interp
title('Length/Distance friction factor')

nexttile
L = LAGraph(:,1);
A = LAGraph(:,2);
C = LAGraph(:,4);
grid on
xv = linspace(min(L), max(L), 200);
yv = linspace(min(A), max(A), 200);
[X,Y] = meshgrid(xv, yv);
Z = griddata(L,A,C,X,Y, 'v4');
surf(X, Y, Z);
grid on
set(gca, 'ZLim',ZLcf)
xlabel('Length (mm)')
ylabel('Angle (°)')
zlabel('Colburn factor')
shading interp
title('Angle/Length Colburn factor')

nexttile
D = DAGraph(:,1);
A = DAGraph(:,2);
C = DAGraph(:,4);
xv = linspace(min(D), max(D), 200);
yv = linspace(min(A), max(A), 200);
[X,Y] = meshgrid(xv, yv);
Z = griddata(D,A,C,X,Y, 'v4');
surf(X, Y, Z);
grid on
xlabel('Distance from front (mm)')
ylabel('Angle (°)')
zlabel('Colburn factor')
set(gca, 'ZLim',ZLcf)
shading interp
title('Angle/Distance Colburn factor')

nexttile
L = LDGraph(:,1);
D = LDGraph(:,2);
C = LDGraph(:,4);
xv = linspace(min(D), max(D), 200);
yv = linspace(min(L), max(L), 200);
[X,Y] = meshgrid(xv, yv);
Z = griddata(D,L,C,X,Y, 'v4');
surf(X, Y, Z);
grid on
xlabel('Distance from front (mm)')
ylabel('Length (mm)')
zlabel('Colburn Factor')
set(gca, 'ZLim',ZLcf)
shading interp
title('Length/Distance Colburn factor')



%% functions

function outputs = opti_funcn(x, k, k2)
```

```
                global k k2
                out1 = k.predict(x);

                out2 = k2.predict(x)*(-1);
                outputs = [out1, out2];

end

function cfout = cfopti_fun(x,k2)

            global k2

            cfout = k2.predict(x)*(-1);

end


function ffout = ffopti_fun(x,k)

            global k

            ffout = k.predict(x);

end
```

9.4 Winglet Optimisation plots

Distance = 0mm, Length = 2mm, Angle = 0°

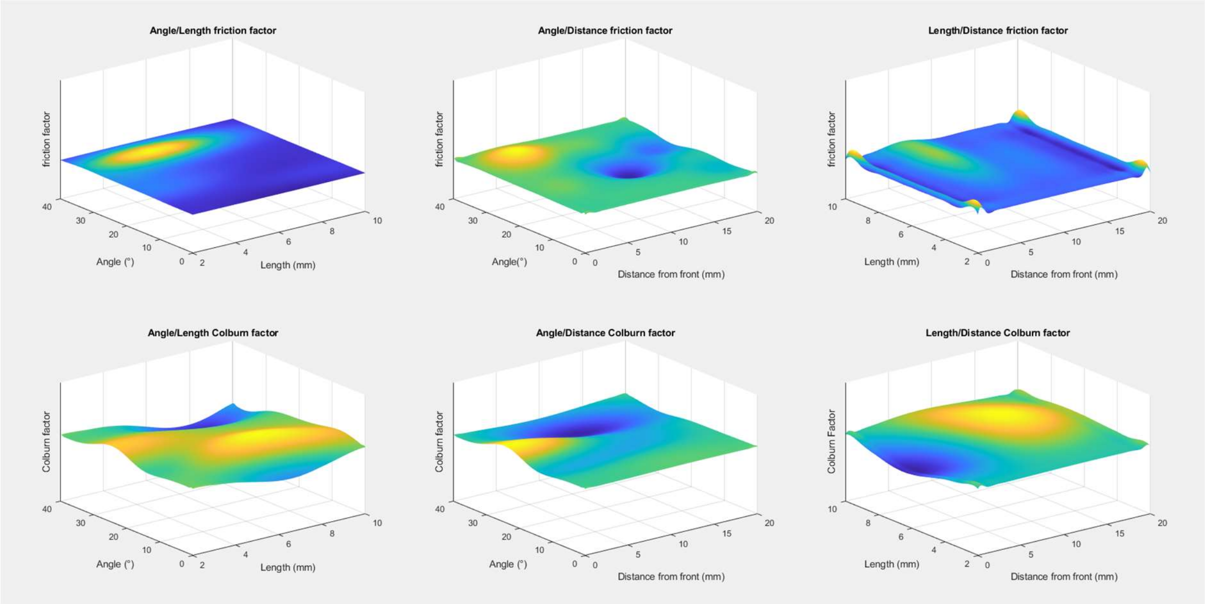

Distance = 10mm, Length = 6mm, Angle = 20°

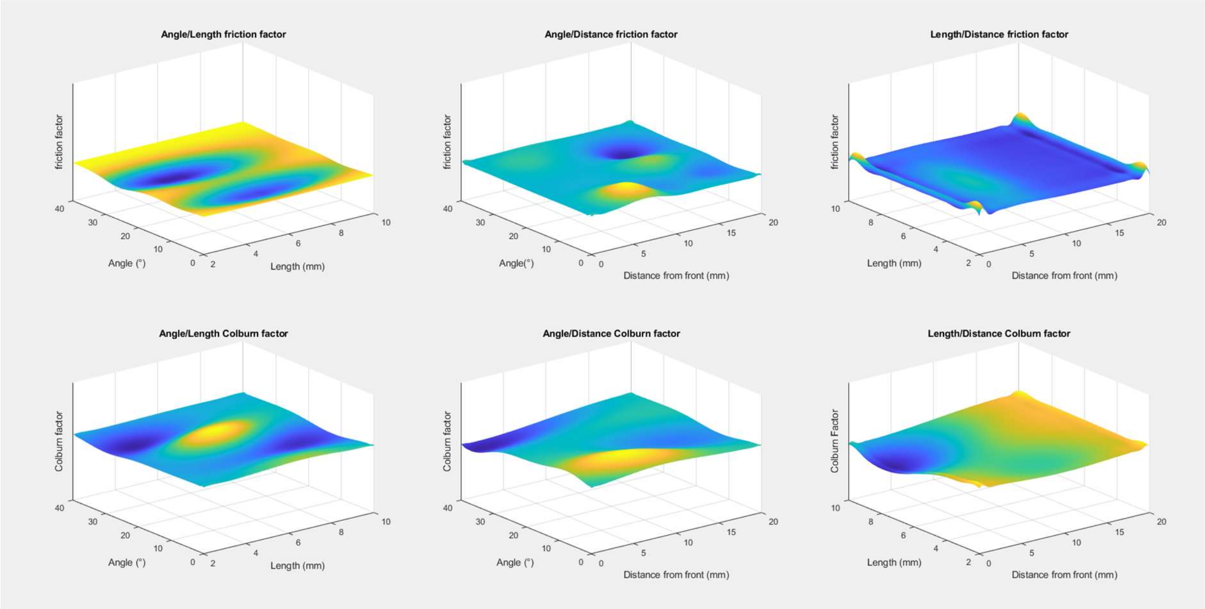

Distance = 20mm, Length = 10mm, Angle = 40°